Optical excitations of spin, lattice and charge degrees of freedom in multiferroics

Dissertation

zur Erlangung des Grades eines

Doktors der Naturwissenschaften

(Dr. rer. nat.)

eingereicht an der

Mathematisch-Naturwissenschaftlich-Technischen Fakultät

der

Universität Augsburg

von

Stephan Reschke

aus Buchloe

Augsburg, im August 2020

Erstgutachter:	Prof. Dr. István Kézsmárki
Zweitgutachterin:	Prof. Dr. Christine Kuntscher
Drittgutachter:	Prof. Dr. Markus Grüninger

Tag der mündlichen Prüfung: 7. Dezember 2020

Contents

1. Motivation

Within the course of this work excitations of spin, lattice and charge degrees of freedom in multiferroic compounds are investigated by means of broadband optical spectroscopy ranging from terahertz frequencies up to the visible spectral range. Multiferroics are materials, which exhibit different ferroic orders that exist simultaneously in the same phase [1–6]. The term multiferroics refers mostly to materials with concomitant ferroelectric and magnetic order. Due to the coupling between microscopic electric and magnetic dipoles, these compounds exhibit magnetoelectric effects. Magnetoelectric materials are subject of intense research activity, as they are promising candidates for technical applications. They may open a path towards energy-efficient data storage technologies [5], low-power electronic devices [7] or magneto-optical diodes [8]. The simultaneous breaking of spatial and time-reversal symmetry is an essential ingredient for the unconventional properties of magnetoelectric materials [5].

For instance, in the investigated polar transition metal molybdenum oxides $M_2Mo_3O_8$ the symmetry conditions under a magnetic field applied perpendicular to the polar axis give rise to unidirectional transmission for light propagating perpendicular to both the polar axis and the magnetic field. This phenomenon is also referred to as the directional dichroism, that is the difference in the absorption of counter-propagating light beams. This violation of the reciprocity principle can occur due to the dynamical magnetoelectric effect under certain symmetry conditions.

Excitations of lattice degrees of freedom, i. e. phonons, are closely linked to the crystal symmetry and, thus, offer the possibility to investigate changes of the symmetry at phase transitions accompanied by structural changes. While the present studies eventually exclude a lattice symmetry lowering upon the magnetic transition of $Fe_2Mo_3O_8$, the phonon study of the lacunar spinels AM_4X_8 provides evidence for the symmetry lowering at the structural transition that typically occurs in these compounds between 30 and 50 K. The lacunar spinels, whith some of them hosting unconventional magnetic structures like cycloidal or Skyrmion lattice phases, have attracted much interest in recent years. So far the electronic structure of these narrow-gap semiconductors has not been fully understood yet and therefore is another objective of the optical measurements performed within the course of this work.

This thesis is structured as follows: At the beginning, the basic ingredients of this work are introduced: The multiferroic materials, the magnetoelectric effect

and the Kubo formula. The last is derived in frame of the linear response theory, and is used to discuss the optical property tensors and the relation between their form and the material symmetry. On this basis, the unidirectional transmission arising from the dynamic magnetoelectric effect is derived. Subsequently, a brief introduction to the experimental techniques, namely the terahertz time-domain spectroscopy and the Fourier-transform infrared spectroscopy, is given and the calculation of the material parameters from the experimental data is explained.

The excitations representing the different degrees of freedom in the studied compounds are usually located in distinct frequency regions. This is reflected in the structure of the results part of this thesis, following the hierarchy of the excitations from low to high energy. At first, the magnons and low-energy excitations of transition-metal molybdenum oxides in the THz range are discussed, which show remarkable directional dichroism. Afterwards, the temperature dependence of the phonon excitations of $Fe_2Mo_3O_8$ in the infrared range and their relation to orbital degrees of freedom are discussed.

The study of the phonons for a broad series of lacunar spinels allows not only to trace the symmetry lowering at the structural phase transition, but also to assign the different modes to distinct structural units. Finally, the systematics of electronic excitations in lacunar spinels are revealed by broadband optical measurements up to the visible range. From experimental side, these compounds are clearly identified as narrow-gap semiconductors already in their high-temperature cubic state. This study, involving compounds with $3d$, $4d$ and $5d$ transition metals, may serve as a solid basis for future theoretical investigations.

2. Introduction

At first, the fundamentals of multiferroics and the magnetoeletric effect will be described. After that, the Kubo formula, which is a basic outcome of linear response theory, will be introduced and its relation to the optical property tensors will be discussed. Based on this, the directional dichroism, which originates from the dynamical magnetoelectric effect, will be explained in detail. Finally, an introduction to the studied compounds, namely the transition metal oxides $M_2\mathrm{Mo}_3\mathrm{O}_8$ and the lacunar spinels AM_4X_8, will be given.

2.1. Multiferroics and the magnetoelectric effect

Multiferroics are compounds exhibiting two or more primary ferroic orders, which coexist in the same phase [1–6]. Ferroic order refers to a spontaneous uniform ordering of a macroscopic property, which is switchable by its conjugate field: This includes ferromagnetic, ferroelectric, ferroelastic and also ferrotoroidic order, where the magnetization $\boldsymbol{M}$ is switchable by magnetic field $\boldsymbol{H}$, the polarization $\boldsymbol{P}$ is switchable by electric field $\boldsymbol{E}$, the strain $\boldsymbol{\epsilon}$ is coupled to stress $\boldsymbol{\sigma}$ and the toroidal moment $\boldsymbol{T}$ is conjugated to crossed electric and magnetic fields $\boldsymbol{E} \times \boldsymbol{H}$ [4, 5, 9]. Nowadays, the term multiferroics is usually also extended to antiferromagnetic and ferrimagnetic order, but mostly refers to magnetoelectric materials combining ferroelectricity and magnetic ordering [5, 6]. Multiferroics can be classified in two groups referred to as type I and type II [5, 10]. In type I multiferroics, ferroelectricity and magnetism are of different origin and occur independently. In type II multiferroics, ferroelectricity and magnetism are strongly coupled to each other and, therefore, appear concomitantly. As it will be elucidated in sections 2.4 and 2.5, all compounds studied in the course of this work are type I multiferroics.

Probably the most interesting aspect of multiferrioc compounds is the cross-coupling between the different order parameters. As a consequence, one order parameter may not only be controlled by its own conjugate field, but also by the conjugate field of another order parameter [6], leading to, e. g., the piezoelectric, magnetoelastic or, most prominent, the magnetoelectric effect, as illustrated in Fig. 2.1.

The magnetoelectric effect, already predicted in 1894 by Pierre Curie [11], allows the control of polarization by magnetic field and the control of magnetization by electric field. Therefore, materials with magnetoelectric coupling have drawn huge

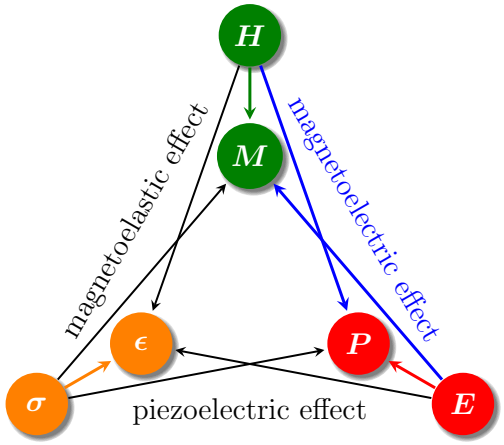

Figure 2.1.: Order parameters $\boldsymbol{P}$, $\boldsymbol{M}$ and $\boldsymbol{\epsilon}$ and their conjugate fields $\boldsymbol{E}$, $\boldsymbol{H}$ and $\boldsymbol{\sigma}$. In multiferroics, via cross couplings an order parameter may not only be controlled by its own conjugate field, resulting in piezoelectricity, magnetoelasticity or magnetoelectricity. Adapted from Ref. [2,3].

research interest, as they have high potential for applications [12]. In the field of information technology, e. g., they open new paths towards miniaturization, enabling electric-field controlled magnetic data storage, multiple-state memories or spintronic devices [2, 12]. The magnetoelectric effect is not strictly restricted to multiferroic materials [5, 13]. On one hand, the presence of magnetic and ferroelectric order is not a sufficient condition for the magnetoelectric effect. On the other hand, the magnetoelectric effect can also occur in compounds that are not multiferroics.

Formally, the magnetoelectric effect can be introduced by the expansion of the free energy $F(\boldsymbol{E}, \boldsymbol{H})$, which in the dc limit under Einstein summation convention is given by [8, 14]:

$$F(\boldsymbol{E},\boldsymbol{H}) = F_0 - P_i^{\mathrm{S}} E_i - M_i^{\mathrm{S}} \mu_0 H_i - \frac{1}{2}\epsilon_0 \chi_{ij}^{\mathrm{ee}} E_i E_j - \frac{1}{2}\mu_0 \chi_{ij}^{\mathrm{mm}} H_i H_j - \sqrt{\epsilon_0 \mu_0}\chi_{ij}^{\mathrm{me}} E_i H_j - \frac{1}{2}\beta_{ijk} E_i H_j H_k - \frac{1}{2}\gamma_{ijk} H_i E_j E_k - \cdots \quad (2.1)$$

Here F_0 is the free energy in the absence of external fields and $\boldsymbol{P}^{\mathrm{S}}$ and $\boldsymbol{M}^{\mathrm{S}}$ are the spontaneous polarization and magnetization, respectively. ϵ_0 and μ_0 are the vacuum permittivity and permeability, respectively. $\hat{\chi}^{\mathrm{ee}}$ and $\hat{\chi}^{\mathrm{mm}}$ denote the electric and magnetic susceptibility tensors. The linear magnetoelectric effect is introduced by the linear magnetoelectric tensor $\hat{\chi}^{\mathrm{me}}$. The third-order tensors $\hat{\beta}$ and $\hat{\gamma}$ account for the contribution from quadratic magnetoelectric effects. From the free energy the

polarization and magnetization are obtained by $\boldsymbol{P} = -\frac{\partial F}{\partial \boldsymbol{E}}$ and $\boldsymbol{M} = -\frac{1}{\mu_0}\frac{\partial F}{\partial \boldsymbol{H}}$ [15]. This results in [8, 13]:

$$\begin{aligned} P_i(\boldsymbol{E},\boldsymbol{H}) &= P_i^{\mathrm{S}} + \epsilon_0\chi_{ij}^{\mathrm{ee}}E_j + \sqrt{\epsilon_0\mu_0}\chi_{ij}^{\mathrm{em}}H_j + \frac{1}{2}\beta_{ijk}H_jH_k + \gamma_{ijk}H_iE_j + \cdots, \\ M_i(\boldsymbol{E},\boldsymbol{H}) &= M_i^{\mathrm{S}} + \chi_{ij}^{\mathrm{mm}}H_j + \sqrt{\frac{\epsilon_0}{\mu_0}}\chi_{ji}^{\mathrm{me}}E_j + \beta_{ijk}E_iH_j + \frac{1}{2}\gamma_{ijk}E_jE_k + \cdots \end{aligned} \tag{2.2}$$

The tensor $\hat{\chi}^{\mathrm{em}}$ accounts for the electric polarization induced by magnetic field, while $\hat{\chi}^{\mathrm{me}}$ describes the magnetization induced by electric field. In some cases, e. g. in magnetic materials with reduced dimensionality [13], the contributions from the higher-order terms $\hat{\beta}$, $\hat{\gamma}$ to the magnetoelectric effect may be crucial. However, often the higher-order terms are neglected [8] and it is enough to concentrate on the linear magnetoelectric effect. It can be shown that the linear magnetoelectric effect is limited by $\chi_{ij}^{\mathrm{me}} < \sqrt{\chi_{ii}^{\mathrm{ee}}\chi_{jj}^{\mathrm{mm}}}$ [8, 13, 16, 17]. This implies that the magnetoelectric effect can especially be strong in ferroelectric and ferromagnetic multiferroics, where both χ^{ee} and χ^{mm} is large [3].

In the following, only the linear magnetoelectric effect will be discussed in detail. Equations 2.2 can be extended to the dynamical case. The dynamical response of polarization and magnetization to oscillating electric and magnetic fields reads as follows:

$$\begin{aligned} \boldsymbol{P}^{\omega} &= \epsilon_0\hat{\chi}^{\mathrm{ee}}\boldsymbol{E}^{\omega} + \sqrt{\epsilon_0\mu_0}\hat{\chi}^{\mathrm{em}}\boldsymbol{H}^{\omega}, \\ \boldsymbol{M}^{\omega} &= \hat{\chi}^{\mathrm{mm}}\boldsymbol{H}^{\omega} + \sqrt{\frac{\epsilon_0}{\mu_0}}\hat{\chi}^{\mathrm{me}}\boldsymbol{E}^{\omega}. \end{aligned} \tag{2.3}$$

The electric and magnetic permeability tensors $\hat{\epsilon}$ and $\hat{\mu}$ are directly related to $\hat{\chi}^{\mathrm{ee}}$ and $\hat{\chi}^{\mathrm{mm}}$ and are introduced according to

$$\begin{aligned} \epsilon_{ij} &= \delta_{ij} + \chi_{ij}^{\mathrm{ee}}, \\ \mu_{ij} &= \delta_{ij} + \chi_{ij}^{\mathrm{mm}}, \end{aligned} \tag{2.4}$$

with δ_{ij} being the Kronecker delta. Using Eqs. 2.3 and 2.4, the electric induction $\boldsymbol{D} = \epsilon_0\boldsymbol{E} + \boldsymbol{P}$ and the magnetic induction $\boldsymbol{B} = \mu_0(\boldsymbol{M} + \boldsymbol{H})$ adopt the symmetrical form

$$\begin{aligned} \boldsymbol{D}^{\omega} &= \epsilon_0\hat{\epsilon}\boldsymbol{E}^{\omega} + \sqrt{\epsilon_0\mu_0}\hat{\chi}^{\mathrm{em}}\boldsymbol{H}^{\omega}, \\ \boldsymbol{B}^{\omega} &= \mu_0\hat{\mu}\boldsymbol{H}^{\omega} + \sqrt{\epsilon_0\mu_0}\hat{\chi}^{\mathrm{me}}\boldsymbol{E}^{\omega}, \end{aligned} \tag{2.5}$$

which is convenient for solving the Maxwell equations. This will be done in section 2.3 in order to demonstrate how the magnetoelectric effect can induce directional dichroism.

2.2. Light-matter interaction in the linear response regime

As already mentioned in the previous chapter, the response of a material to electromagnetic radiation is described by the optical property tensors. In the experiments performed in this work, the electromagnetic radiation can be regarded as a small perturbation and, thus, the optical property tensors can be treated within the scope of the linear response theory, which allows to express the elements of the optical property tensors by the Kubo formula.

In general, linear response theory considers a perturbation coupled to an operator $\hat{B}$ according to a perturbation Hamiltonian $\delta\hat{H}(t) = -\hat{B}f(t)$ [18]. Provided that the perturbation is small compared to the equilibrium Hamiltonian, the response observed as a change $\delta\hat{A}$ of the expectation value of the operator $\hat{A}$ can be treated in linear approximation. It can be shown that the non-equilibrium expectation value of $\hat{A}$ at a given time t can then be written as [18]:

$$\langle\hat{A}\rangle(t) = \langle\hat{A}\rangle_0 + \delta\hat{A}(t) = \langle\hat{A}\rangle_0 + \int_{-\infty}^{t} \chi^{AB}(t,t')f(t')\,\mathrm{d}t'. \tag{2.6}$$

Here $\langle\hat{A}\rangle_0$ denotes the expectation value of $\hat{A}$ of the unperturbed state. The linear response function χ^{AB} is given by

$$\chi^{AB}(t,t') = \frac{i}{\hbar}\langle[\hat{A}(t),\hat{B}(t')]\rangle_0\,\Theta(t-t'), \tag{2.7}$$

where $\Theta(t-t')$ is the Heaviside step function. $\Theta(t-t')$ ensures that the causality principle is fulfilled , i. e. if the perturbation is switched on at $t = t'$, then $\delta\hat{A}$ can only be different from zero for $t \geq t'$.

Evaluation and subsequent Fourier transformation of Eq. 2.7 results in the Kubo formula, which provides an expression for the frequency dependent response function $\chi_{AB}(\omega)$. In the zero temperature limit $\chi_{AB}(\omega)$ is given by:

$$\begin{aligned}\chi_{AB}(\omega) &= \frac{2}{\hbar}\sum_n \left[\frac{\omega_{n0}\Re\{\langle 0|\,\hat{A}\,|n\rangle\,\langle n|\,\hat{B}\,|0\rangle\}}{\omega_{n0}^2-\omega^2-2i\omega\delta_n} + \frac{i\omega\Im\{\langle 0|\,\hat{A}\,|n\rangle\,\langle n|\,\hat{B}\,|0\rangle\}}{\omega_{n0}^2-\omega^2-2i\omega\delta_n}\right] \\ &= \chi'_{AB} + \chi''_{AB}.\end{aligned} \tag{2.8}$$

The Kubo formula contains matrix elements describing transitions from the ground state $|0\rangle$ to an excited state $|n\rangle$ separated by the energy $E_n = \hbar\omega_{n0}$. δ_n is the inverse lifetime of $|n\rangle$. The symbols $\Re$ and $\Im$ denote real and imaginary parts. It is convenient to separate χ_{AB} into the terms containing the real (χ'_{AB}) and imaginary

parts (χ''_{AB}) of the matrix element products. χ'_{AB} and χ''_{AB} are not to be confused with the actual real and imaginary parts of χ_{AB}.

When exchanging the operators $\hat{A}$ and $\hat{B}$, the following relations directly result from the Kubo formula:

$$\begin{aligned} \chi'_{AB} &= \chi'_{BA}, \\ \chi''_{AB} &= -\chi''_{BA}. \end{aligned} \tag{2.9}$$

Furthermore, it can be shown that under the time-reversal symmetry operation $\hat{\mathbb{T}}$ the response function behaves as follows [19]:

$$\hat{\mathbb{T}}\left\{\chi_{AB}\right\} = \varepsilon_A \varepsilon_B \chi_{BA}. \tag{2.10}$$

The coefficients ε_A and ε_B account for the behavior of $\hat{A}$ and $\hat{B}$ under time reversal. They are either $+1$ or -1 depending on whether the respective operator represents a time-reversal even or odd quantity.

Now the general operators $\hat{A}$ and $\hat{B}$ can be related to the magnetic and electric dipole operators $\hat{m}_i$ and $\hat{p}_i$ and the response function χ_{AB} can be identified with the optical property tensors. Consequently, the optical property tensors can be expressed in their microscopic form by the Kubo formula [20]:

$$\begin{aligned} \epsilon_{ij}(\omega) &= \delta_{ij} + \frac{2}{V\hbar\epsilon_0} \sum_n \left[\frac{\omega_{n0} \Re\{\langle 0|\, \hat{p}_i \,|n\rangle \langle n|\, \hat{p}_j \,|0\rangle\}}{\omega_{n0}^2 - \omega^2 - 2i\omega\delta_n} + \frac{i\omega \Im\{\langle 0|\, \hat{p}_i \,|n\rangle \langle n|\, \hat{p}_j \,|0\rangle\}}{\omega_{n0}^2 - \omega^2 - 2i\omega\delta_n} \right] \\ &= \epsilon'_{ij} + \epsilon''_{ij}, \end{aligned} \tag{2.11}$$

$$\begin{aligned} \mu_{ij}(\omega) &= \delta_{ij} + \frac{2\mu_0}{V\hbar} \sum_n \left[\frac{\omega_{n0} \Re\{\langle 0|\, \hat{m}_i \,|n\rangle \langle n|\, \hat{m}_j \,|0\rangle\}}{\omega_{n0}^2 - \omega^2 - 2i\omega\delta_n} + \frac{i\omega \Im\{\langle 0|\, \hat{m}_i \,|n\rangle \langle n|\, \hat{m}_j \,|0\rangle\}}{\omega_{n0}^2 - \omega^2 - 2i\omega\delta_n} \right] \\ &= \mu'_{ij} + \mu''_{ij}, \end{aligned} \tag{2.12}$$

$$\begin{aligned} \chi^{\mathrm{me}}_{ij}(\omega) &= \frac{2}{V\hbar}\sqrt{\frac{\mu_0}{\epsilon_0}} \sum_n \left[\frac{\omega_{n0} \Re\{\langle 0|\, \hat{m}_i \,|n\rangle \langle n|\, \hat{p}_j \,|0\rangle\}}{\omega_{n0}^2 - \omega^2 - 2i\omega\delta_n} + \frac{i\omega \Im\{\langle 0|\, \hat{m}_i \,|n\rangle \langle n|\, \hat{p}_j \,|0\rangle\}}{\omega_{n0}^2 - \omega^2 - 2i\omega\delta_n} \right] \\ &= \chi^{\mathrm{me}\,\prime}_{ij} + \chi^{\mathrm{me}\,\prime\prime}_{ij}. \end{aligned} \tag{2.13}$$

Here V denotes the volume of the system. $\hat{\chi}^{\mathrm{em}}$ can be written analogously to $\hat{\chi}^{\mathrm{me}}$. Furthermore, it follows directly from Eqs. 2.9 that these two tensors are related to each other according to

$$\chi^{\mathrm{me}}_{ij} = \chi^{\mathrm{me}\,\prime}_{ij} + \chi^{\mathrm{me}\,\prime\prime}_{ij} = \chi^{\mathrm{em}\,\prime}_{ji} - \chi^{\mathrm{em}\,\prime\prime}_{ji}. \tag{2.14}$$

The electric dipole operator $\hat{p}_i$ is time-reversal even, whereas the magnetic dipole operator $\hat{m}_i$ is time-reversal odd. Therefore, the coefficients introduced in Eqs. 2.10

are $\varepsilon_{p_i} = +1$ and $\varepsilon_{m_i} = -1$. With that it follows from Eqs. 2.9 and 2.10 that the ϵ'_{ij} and μ'_{ij} are time-reversal even and the ϵ''_{ij} and μ''_{ij} are time-reversal odd quantities. On the contrary, the $\chi^{\mathrm{me}\,\prime}_{ij}$ and $\chi^{\mathrm{em}\,\prime}_{ij}$ are time-reversal odd and the $\chi^{\mathrm{me}\,\prime\prime}_{ij}$ and $\chi^{\mathrm{em}\,\prime\prime}_{ij}$ are time-reversal even quantities. As it is clear from Eq. 2.8, in the zero-frequency limit ϵ''_{ij}, μ''_{ij} and $\chi^{\mathrm{me}\,\prime\prime}_{ij}$ vanish and, hence, the static response is described solely by ϵ'_{ij}, μ'_{ij} and $\chi^{\mathrm{me}\,\prime}_{ij}$.

It was shown in section 2.1 that the dynamical magnetoelectric effect is governed by the dynamical magnetoelectric susceptibility tensors $\hat{\chi}^{\mathrm{me}}$ and $\hat{\chi}^{\mathrm{em}}$. As it can be seen from Eq. 2.13, $\hat{\chi}^{\mathrm{me}}$ is finite only, if both matrix elements $\langle 0|\,\hat{m}_i\,|n\rangle$ and $\langle n|\,\hat{p}_j\,|0\rangle$ are finite, i. e. if the transition from the ground state $|0\rangle$ to the excited state $|n\rangle$ can be excited both via the magnetic and electric dipole operator. This implies that the dynamical magnetoelectrical effect only appears for both electric and magnetic dipole active excitations [21], so-called magnetoelectric resonances. Concerning low-energy spin excitations, these are to be distinguished from the purely magnetic dipole active conventional magnons and the purely electric dipole active electromagnons.

2.3. Unidirectional transmission

When spatial and time-reversal symmetry are simultaneously broken, in a material the refractive index for light beams travelling along certain direction can have four different values, corresponding to the two orthogonal polarizations and the two directions of propagation, $\pm\boldsymbol{k}$ [20,22]. This is called quadrochroism. Consequently, counter-propagating light beams with propagation directions $+\boldsymbol{k}$ and $-\boldsymbol{k}$ can have different absorption strengths. In the long-wavelength limit, when the light-matter interaction is well described by $\hat{\chi}^{\mathrm{ee}}$, $\hat{\chi}^{\mathrm{mm}}$, $\hat{\chi}^{\mathrm{em}}$ and $\hat{\chi}^{\mathrm{me}}$, the origin of such directional dichroism is the dynamical magnetoelectric effect. Therefore, it is not surprising that strong directional dichroism has particularly been reported in studies on multiferroics, where it was found for frequencies ranging from the GHz up to the visible range [20,21,23–32].

In compounds with coexisting crossed polarization and magnetization, directional dichroism can emerge for light propagating parallel or antiparallel to $\boldsymbol{P}\times\boldsymbol{M}$ [29,33–35]. Thus, the product $\boldsymbol{k}\cdot(\boldsymbol{P}\times\boldsymbol{M})$ is a measure of the magnetoelectric directional anisotropy [27,36]. It will be shown, that in this case directional dichroism occurs for both electric and magnetic dipole active excitations due to off-diagonal time-reversal odd components of the magnetoelectric susceptibility tensor [30,37,38]. The cross product $\boldsymbol{P}\times\boldsymbol{M}$ is closely related to the toroidal moment [8,35], which can be defined as $\boldsymbol{T} = \frac{1}{2}\sum_i \boldsymbol{r}_i \times \boldsymbol{S}_i$ [39,40], where $\boldsymbol{r}_i$ is the position of spin $\boldsymbol{S}_i$. $\boldsymbol{T}$ and $\boldsymbol{P}\times\boldsymbol{M}$ have the same symmetry [17] and, although not strictly following the definition, the toroidal moment is often referred to $\boldsymbol{T} = \boldsymbol{P}\times\boldsymbol{M}$ [21,35,39], as it will also be done in the following.

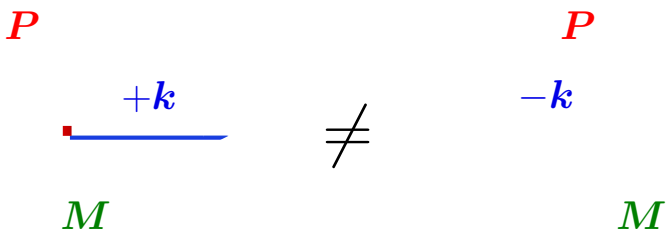

Figure 2.2.: Schematic illustration of the $\boldsymbol{k} \cdot (\boldsymbol{P} \times \boldsymbol{M})$ directional anisotropy. In presence of a toroidal moment $\boldsymbol{T} = \boldsymbol{P} \times \boldsymbol{M}$ parallel to the propagation direction the $+\boldsymbol{k}$ and $-\boldsymbol{k}$ configurations are not equivalent, as they are not connected by symmetry operations.

The situation of crossed polarization and magnetization and a light beam propagating either parallel or antiparallel to $\boldsymbol{P} \times \boldsymbol{M}$ is schematically illustrated in Fig. 2.2. The $+\boldsymbol{k}$ and $-\boldsymbol{k}$ configurations are not equivalent, as they are not connected by any symmetry of the material: There is no symmetry operation, which reverses $\boldsymbol{k}$, but at the same time leaves $\boldsymbol{T}$ intact. Both time and spatial inversion reverse the sign of $\boldsymbol{k}$. While time reversal changes the sign of $\boldsymbol{M}$, but leaves $\boldsymbol{P}$ intact, spatial inversion reverses $\boldsymbol{P}$, but leaves $\boldsymbol{M}$ intact. Consequently, both time and spatial inversion operation change the sign of both $\boldsymbol{T} = \boldsymbol{P} \times \boldsymbol{M}$ and $\boldsymbol{k}$. From this it directly follows that a necessary condition of directional dichroism is the simultaneous breaking of the time reversal and the spatial inversion.

For the occurrence of such nonreciprocal light propagation the symmetry, in particular the magnetic point group, plays a crucial role [41]. The case of perpendicular polarization and magnetization is described by the magnetic point group symmetry $2'm'm$. More precisely, when assuming the magnetization pointing along the x-axis and the polarization pointing along the z-axis, the magnetic point group is $2'_z m'_{xz} m_{yz}$. Here we assume that the crystal structure does not further reduce the symmetry, i. e. in the absence of $\boldsymbol{P}$ and $\boldsymbol{M}$ the crystal symmetry is $2_z m_{xz} m_{yz} 1'$ or higher. It will be shown in section 2.4 that this symmetry can be realized in the antiferromagnetically ordered phases of the transition metal molybdenum oxides $M_2\mathrm{Mo_3O_8}$ by applying a magnetic field perpendicular to their polar six-fold rotational axis.

For a given symmetry the form of the optical property tensors can be derived from Neumann's principle, which states that any physical property must be

invariant under the symmetry operations of the crystal [42]. For the magnetic point group $2'_z m'_{xz} m_{yz}$ the optical property tensors have the following form:

$$\hat{\epsilon} = \begin{pmatrix} \epsilon'_{xx} & 0 & 0 \\ 0 & \epsilon'_{yy} & \epsilon''_{yz} \\ 0 & -\epsilon''_{yz} & \epsilon'_{zz} \end{pmatrix} \qquad \hat{\mu} = \begin{pmatrix} \mu'_{xx} & 0 & 0 \\ 0 & \mu'_{yy} & \mu''_{yz} \\ 0 & -\mu''_{yz} & \mu'_{zz} \end{pmatrix}$$
$$\hat{\chi}^{\mathrm{me}} = \begin{pmatrix} 0 & \chi''_{xy} & \chi'_{xz} \\ \chi''_{yx} & 0 & 0 \\ \chi'_{zx} & 0 & 0 \end{pmatrix} \qquad \hat{\chi}^{\mathrm{em}} = \begin{pmatrix} 0 & -\chi''_{yx} & \chi'_{zx} \\ -\chi''_{xy} & 0 & 0 \\ \chi'_{xz} & 0 & 0 \end{pmatrix} \tag{2.15}$$

Now the directional dichroism can be quantitatively described by solving the Maxwell equations for a light beam propagating along the y-direction. The Fourier transformed Maxwell equations can be written as

$$\begin{aligned} -\omega \boldsymbol{D}^{\omega} &= \boldsymbol{k} \times \boldsymbol{H}^{\omega}, \\ \omega \boldsymbol{B}^{\omega} &= \boldsymbol{k} \times \boldsymbol{E}^{\omega}, \end{aligned} \tag{2.16}$$

where $\boldsymbol{D}^{\omega}$ and $\boldsymbol{B}^{\omega}$ are given by Eqs. 2.5. Furthermore the refractive index n is introduced as

$$n = \frac{kc}{\omega} = \frac{k}{\omega\sqrt{\epsilon_0 \mu_0}}, \tag{2.17}$$

where c is the speed of light in vacuum. Solving the Maxwell equations 2.16 for $\boldsymbol{k} \parallel y$ yields four different solutions for the refractive index. For both orthogonal linear polarizations there are two solutions corresponding to $+\boldsymbol{k}$ and $-\boldsymbol{k}$ propagation direction:

$$n_{zx}^{\pm \boldsymbol{k}} = \sqrt{\frac{\epsilon'_{yy}\epsilon'_{zz} + \epsilon''^2_{yz}}{\epsilon'_{yy}} \left(\frac{\chi''^2_{xy}}{\epsilon'_{yy}} + \mu'_{xx} \right)} \pm \left(\chi'_{xz} - \chi''_{xy} \frac{\epsilon''_{yz}}{\epsilon'_{yy}} \right) \tag{2.18}$$

$$\approx \sqrt{\epsilon'_{zz}\mu'_{xx}} \pm \chi'_{xz}, \tag{2.19}$$

$$n_{xz}^{\pm \boldsymbol{k}} = \sqrt{\frac{\mu'_{yy}\mu'_{zz} + \mu''^2_{yz}}{\mu'_{yy}} \left(\frac{\chi''^2_{yx}}{\mu'_{yy}} + \epsilon'_{xx} \right)} \mp \left(\chi'_{zx} + \chi''_{yx} \frac{\mu''_{yz}}{\mu'_{yy}} \right) \tag{2.20}$$

$$\approx \sqrt{\epsilon'_{xx}\mu'_{zz}} \mp \chi'_{zx}. \tag{2.21}$$

Here $n_{zx}^{\pm \boldsymbol{k}}$ are the solutions for polarization $\boldsymbol{E}^{\omega} \parallel z$ / $\boldsymbol{H}^{\omega} \parallel x$ and $n_{xz}^{\pm \boldsymbol{k}}$ are the solutions for polarization $\boldsymbol{E}^{\omega} \parallel x$ / $\boldsymbol{H}^{\omega} \parallel z$. From the approximate solutions 2.19 and 2.21 it becomes apparent that the directional dichroism is caused by the time-reversal odd off-diagonal components of the magnetoelectric susceptibility

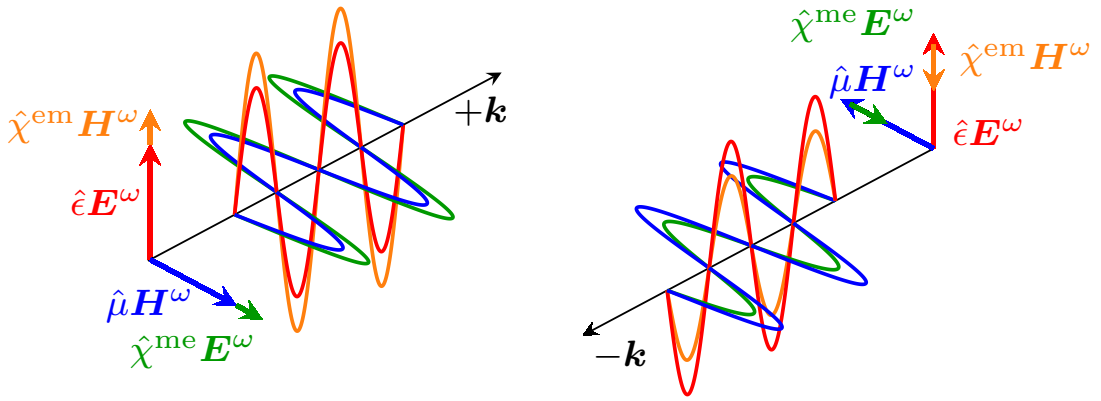

Figure 2.3.: Schematical illustration of the directional dichroism. Left: For propagation direction $+\boldsymbol{k}$ the contributions induced by $\hat{\chi}^{\mathrm{em}}$ and $\hat{\chi}^{\mathrm{me}}$ are parallel to those from $\hat{\epsilon}$ and $\hat{\mu}$, resulting in an enhancement of the amplitude of the electromagnetic wave. Right: For propagation direction $-\boldsymbol{k}$ the contributions induced by $\hat{\chi}^{\mathrm{em}}$ and $\hat{\chi}^{\mathrm{me}}$ are antiparallel to those from $\hat{\epsilon}$ and $\hat{\mu}$, resulting in a reduction of the amplitude of the electromagnetic wave.

tensors. It is convenient to consider the difference of the absorption coefficients $\Delta\alpha$ of two counter-propagating beams [21]

$$\Delta\alpha_{ij} = \alpha_{ij}^{+\boldsymbol{k}} - \alpha_{ij}^{-\boldsymbol{k}} = \frac{2\omega}{c}\Im\{n_{ij}^{+\boldsymbol{k}} - n_{ij}^{-\boldsymbol{k}}\} \approx \frac{4\omega}{c}\Im\{\chi'_{ji}\}. \tag{2.22}$$

A schematical illustration of the directional dichroism is shown in Fig. 2.3. Both in the $+\boldsymbol{k}$ and the $-\boldsymbol{k}$ configuration, contributions to the polarization and magnetization arise from $\boldsymbol{E}^{\omega}$ and $\boldsymbol{H}^{\omega}$ via the diagonal elements of $\hat{\epsilon}$ and $\hat{\mu}$. Furthermore, an additional contribution to the polarization emerges from $\boldsymbol{H}^{\omega}$ via the off-diagonal elements of χ^{em}, and an additional contribution to the magnetization emerges from $\boldsymbol{E}^{\omega}$ via the off-diagonal elements of χ^{me}. Without loss of generality it can be assumed that these additional contributions interfere constructively with the contributions from $\hat{\epsilon}$ and $\hat{\mu}$ in the $+\boldsymbol{k}$ configuration. Reversal of the propagation direction changes the relative sign of $\boldsymbol{E}^{\omega}$ and $\boldsymbol{H}^{\omega}$ and consequently the contributions induced by $\hat{\chi}^{\mathrm{em}}$ and $\hat{\chi}^{\mathrm{me}}$ are now antiparallel to those induced by $\hat{\epsilon}$ and $\hat{\mu}$. This results in a reduction of the amplitude of the electromagnetic wave in the $-\boldsymbol{k}$ configuration and, thus, in different absorption strengths for the counter-propagating beams.

When following the discussion of Fig. 2.2, it becomes apparent that the reversal of $\boldsymbol{k}$ is equivalent to reversing the toroidal moment $\boldsymbol{T} = \boldsymbol{P} \times \boldsymbol{M}$ by either changing the sign of $\boldsymbol{P}$ or $\boldsymbol{M}$. In the course of this work all three possibilities of switching the sign of $\boldsymbol{k} \cdot (\boldsymbol{P} \times \boldsymbol{M})$, thus, realizing directional dichroism have been investigated experimentally.

2.4. Transition metal Mo oxides $M_2Mo_3O_8$

The transition metal Mo oxides $M_2Mo_3O_8$ ($M =$ Mn, Fe, Co, Zn) are type I multiferroics, which exhibit a variety of magnetoelectric effects. In the course of this work optical spectroscopy studies have been performed on $Co_2Mo_3O_8$ and $Fe_2Mo_3O_8$ as well as on 7 % Zn substituted $Fe_2Mo_3O_8$, namely $Fe_{1.86}Zn_{0.14}Mo_3O_8$. In the following part an introduction to the structural, magnetic and polar properties of these compounds and an overview of the occurring magnetoelectric effects will be given.

The transition metal Mo oxides crystallize in a hexagonal structure with the noncentrosymmetric polar space group $P6_3mc$ [43–49]. The unit cell of the crystallographic structure of $M_2Mo_3O_8$ is shown in Fig. 2.4 (a). It consists of alternating layers of M^{2+} and Mo^{4+} ions, which are stacked along the c-axis. The magnetic M^{2+} ions are located both in octahedral and tetrahedral oxygen coordination. The corner-sharing MO_6 octahedra and MO_4 tetrahedra form honeycomb-like layers in the ab-plane [7], as shown in Fig. 2.4 (b). The polar nature of the $M_2Mo_3O_8$ compounds is reflected in the polar arrangement of the MO_4 tetrahedra, which are all pointing in the same direction along the c-axis. This results in a ferroelectric polarization parallel to the c-axis [7, 50, 51]. The Mo^{4+} ions are found in octahedral oxygen coordination and form Kagome-like layers in the ab-plane [7] as illustrated in Fig. 2.4 (e).

In the $M_2Mo_3O_8$ compounds the M^{2+} ions are responsible for the magnetism. The Mo^{4+} ions are arranged in triangular groups as Mo_3O_{13} clusters, which form spin-singlet trimers [44, 52], as highlighted in Fig. 2.4 (e). Consequently, the Mo_3O_{13} clusters are diamagnetic, but otherwise they do not contribute to the magnetism. Upon cooling the polar $M_2Mo_3O_8$ compounds undergo magnetic ordering in the temperature range between 40 and 60 K and, thus, become multiferroic. For the studied compounds either antiferromagnetic or ferrimagnetic ordering is realized.

The antiferromagnetic spin arrangement is illustrated by the arrows in Fig. 2.4 (c). Both the spins on the tetrahedral and the octahedral M^{2+} sites are aligned along the c-axis, forming a four-sublattice easy-axis antiferromagnetic structure. Within one layer the spins at tetrahedral and octahedral sites order antiferromagnetically. In neighboring layers both the tetrahedral and the octahedral spins are arranged in an antiferromagnetic manner. As it is recognizable from Fig. 2.4 (c), the magnetic moments at the tetrahedral and the octahedral sites are not equivalent, which results in a net ferrimagnetic magnetization of each single layer. The antiferromagnetic arrangement of neighboring layers leads to an overall cancellation of the magnetization in the antiferromagnetic state.

In $Fe_2Mo_3O_8$ the magnetic moment of the octahedral sites is larger than that of the tetrahedral sites and their values clearly exceed the spin-only value of 4 μ_B due sizeable orbital contribution. For the moments at octahedral and tetrahedral sites values of 4.85 μ_B and 4.21 μ_B have been found, respectively [44]. In contrast,

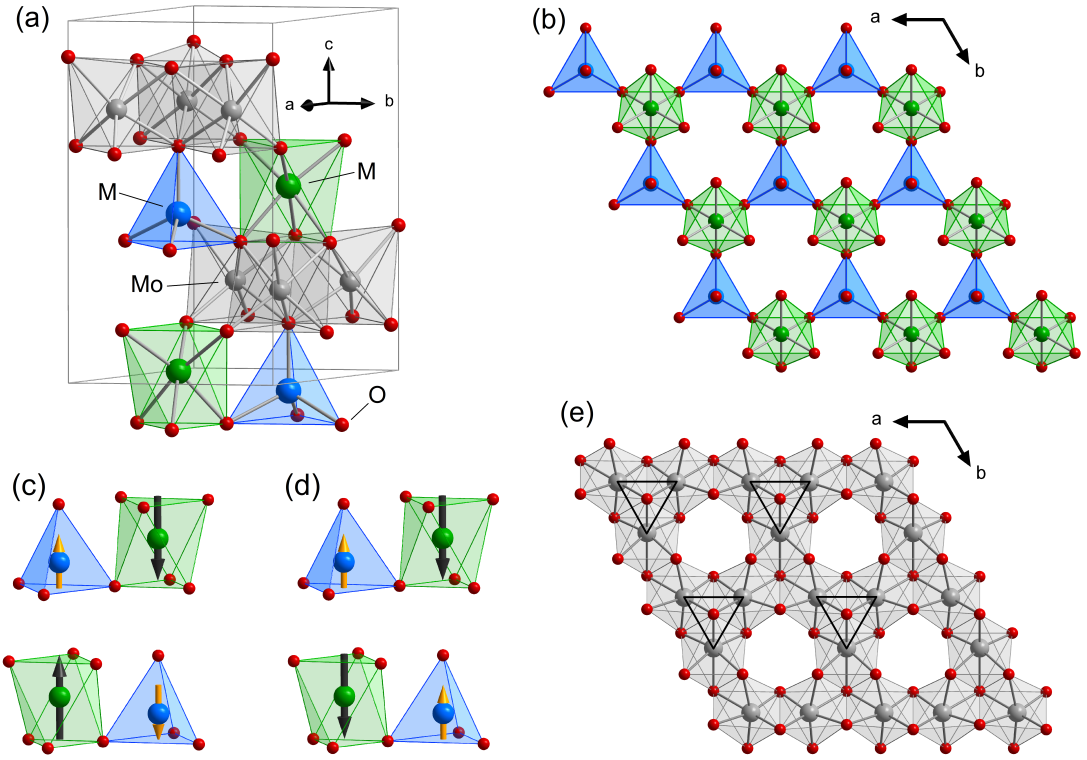

Figure 2.4.: (a) Unit cell of $M_2Mo_3O_8$. The M^{2+} ions are located in octahedral (green) and tetrahedral (blue) oxigen coordination. (b) View of a M^{2+} layer along the c-axis. (c) Schematical illustration of the antiferromagnetic and (d) ferrimagnetic spin arrangement. (e) View of a Mo layer along the c-axis with highlighted Mo trimers.

in $Co_2Mo_3O_8$ the refined moment of the tetrahedral site is larger and the values for the tetrahedral and octahedral site of $3.44\,\mu_B$ and $3.35\,\mu_B$, respectively, are closer to each other [51].

The spin arrangement of the ferrimagnetic order is illustrated in Fig. 2.4 (d). In the ferrimagnetic structure the spins are also aligned along the polar axis. Within the *ab*-plane the spins at the tetrahedral and octahedral sited are again ordered antiferromagnetically. The ferrimagnetic structure can be obtained from the antiferromagnetic structure by flipping the spins in every second M^{2+} layer. The single layers are arranged in a ferromagnetic manner, which results in a ferrimagnetic net magnetization.

The ferrimagnetic state is realized in $Mn_2Mo_3O_8$, which undergoes magnetic ordering below $T_c = 41\,\mathrm{K}$ [45, 48, 53]. Due to the weak spin anisotropy of Mn^{2+} a spin-flop state can be realized in $Mn_2Mo_3O_8$ in relatively low magnetic fields $H \parallel c$ [53].

In contrast, antiferromagnetic ordering is realized in $Co_2Mo_3O_8$ and $Fe_2Mo_3O_8$. For $Co_2Mo_3O_8$ the ordering takes place at $T_N = 40\,\mathrm{K}$ [45, 48, 49, 51], a ordering

temperature of $T_N = 60\,K$ [7, 45, 48, 50] has been found in $Fe_2Mo_3O_8$. In $Fe_2Mo_3O_8$ besides the antiferromagnetic order also a ferrimagnetic state can be realized. The ferrimagnetic state can be established in $Fe_2Mo_3O_8$ by applying a magnetic field along the *c*-axis [7] and can be stabilized by isovalent substitution of Fe^{2+} by non-magnetic Zn^{2+} [45,50]. It has been shown by Mössbauer spectroscopy that the Zn^{2+} ions preferably occupy the tetrahedral sites [44]. According to GGA+*U* calculations this selectivity is ascribed to the different ionic radii of Fe^{2+} and Zn^{2+} [54].

The effect of the Zn doping is illustrated by the magnetic field - temperature phase diagrams of $Fe_2Mo_3O_8$ and $Fe_{1.86}Zn_{0.14}Mo_3O_8$, which are shown in Fig. 2.5. For pure $Fe_2Mo_3O_8$ the antiferromagnetic state is realized below $T_N = 60\,K$ when cooling down in low magnetic fields. Dependent on the temperature the ferrimagnetic order is established above a critical magnetic field $H_c \parallel c$. At T_N the critical field is approximately 4 T and continuously increases with decreasing temperature. In pure $Fe_2Mo_3O_8$ the transition from the antiferromagnetic to the ferrimagnetic state is reversible without hysteresis when going back to low magnetic fields.

In $Fe_{1.86}Zn_{0.14}Mo_3O_8$, shown in Fig. 2.5 (b), T_N is slightly reduced to 54 K and the ferrimagnetic phase is clearly stabilized. The antiferromagnetic state is only realized when cooling down in very low magnetic fields $< 0.1\,T$. The critical field again increases continuously with decreasing temperature, however, the field values are considerably lower than in pure $Fe_2Mo_3O_8$. In contrast to $Fe_2Mo_3O_8$, in $Fe_{1.86}Zn_{0.14}Mo_3O_8$ the switching to the metastable ferrimagnetic state is irreversible. The ferrimagnetic state is preserved when removing the magnetic field, which is resulting in a hysteretic region as illustrated by the hatched area in the phase diagram. Studies on $Fe_2Mo_3O_8$ with different Zn doping concentrations confirm that the phase diagram is very sensitive to the Zn content and that the ferrimagnetic state is easily stabilized by slight Zn doping [50]. These findings suggest that in $Fe_2Mo_3O_8$ the antiferromagnetic and the ferrimagnetic order are close in energy. This is also in line with the exchange couplings derived for $Fe_2Mo_3O_8$ and $Fe_{1.86}Zn_{0.14}Mo_3O_8$. The magnetic exchange coupling within the *ab*-plane is the strongest, whereas the inter-layer exchange couplings are weaker [54,55] as the Fe^{2+} layers are separated by the Mo layers. Therefore, the ferrimagnetic moments of the single layers can be aligned by relatively low magnetic fields.

Interestingly, the metamagnetic transition from the antiferromagnetic to the ferrimagnetic state in $Fe_{1.86}Zn_{0.14}Mo_3O_8$ happens via a two-step magnetization process, as illustrated by the two critical fields H_{c1} and H_{c2} in Fig. 2.5 (b). Similar findings have already been reported on 12.5 % and 25 % Zn doped samples and have been ascribed to several competing magnetic phases [56]. Based on our magnon spectroscopy studies on $Fe_{1.86}Zn_{0.14}Mo_3O_8$ we conclude a coexistence of the antiferromagnetic and the ferrimagnetic phases for $H_{c1} < H < H_{c2}$ [57] (see section 4.2.2).

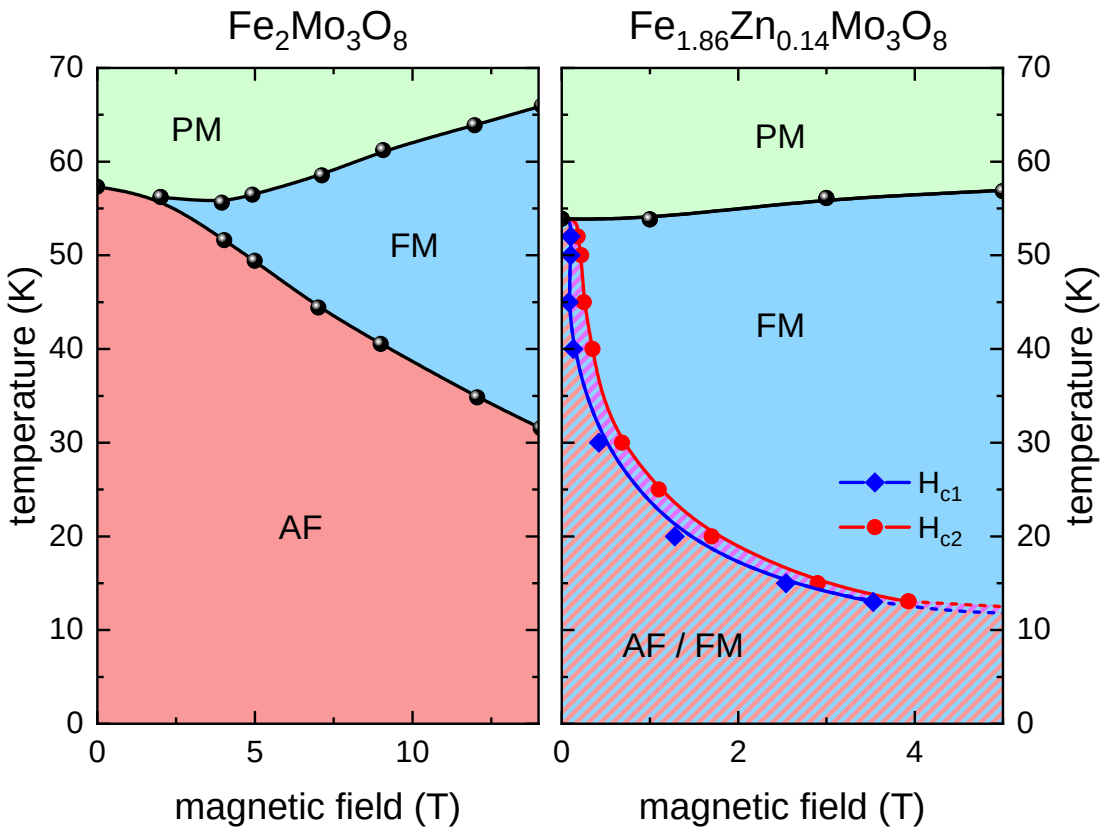

Figure 2.5.: *H-T* phase diagrams of (a) $Fe_2Mo_3O_8$ and (b) $Fe_{1.86}Zn_{0.14}Mo_3O_8$, with the magnetic field $H \parallel c$. The hatched area corresponds to a hysteretic region. PM, AF and FM denote the paramagnetic, antiferromagnetic and ferrimagnetic phases, respectively. Data of $Fe_2Mo_3O_8$ are taken from Ref. [50], data of $Fe_{1.86}Zn_{0.14}Mo_3O_8$ were obtained from magnetization and specific heat measurements on our own samples.

For $Co_2Mo_3O_8$ the situation is slightly different. In contrast to $Fe_2Mo_3O_8$ the antiferromagnetically ordered phase is more stable in $Co_2Mo_3O_8$ [51]. So far no additional magnetic phase was reported in literature. However, preliminary high-field magnetization measurements with magnetic field applied along the *c*-axis revealed a metamagnetic phase transition around 30 T [58].

As already mentioned, the polarity of the $M_2Mo_3O_8$ compounds originates from the crystal structure and a small ferroelectric polarization along the *c*-direction can already be observed for temperatures above T_N. Besides, a considerable increase of the polarization is observed when entering the magnetically ordered phases, which indicates a sizeable magnetically induced ferroelectric contribution to the polarization [7, 50, 51, 53]. Studies on pure and Zn doped $Fe_2Mo_3O_8$ revealed a different ferroelectric polarization for the antiferromagnetic and ferrimagnetic phase [7, 50].

Among different mechanisms for spin-induced ferroelectricity, exchange striction has been identified as the main mechanism behind the magnetically induced polarization [7,51]. Via this mechanism ions are shifted to gain exchange energy by optimization of the symmetric spin interaction $\boldsymbol{S}_i \cdot \boldsymbol{S}_j$ [5]. This ionic shifts result in the ferroelectric polarization $\boldsymbol{P}_{ij} \propto \boldsymbol{R}_{ij}(\boldsymbol{S}_i \cdot \boldsymbol{S}_j)$, with $\boldsymbol{R}_{ij}$ being the direction of the magnetostriction. Despite the displacement of the ions at T_N, the space group symmetry $P6_3mc$ is preserved both in $Co_2Mo_3O_8$ [51] and $Fe_2Mo_3O_8$ [59], although for the latter compound symmetry lowering had been suggested previously [60], as will be discussed in section 5.1.

In addition to exchange striction also the *d-p* hybridization mechanism is relevant for the ferroelectric polarization in the $M_2Mo_3O_8$ compounds. It describes the spin-direction dependent hybridization of a magnetic ion *d* orbital with a ligand *p* orbital resulting in a polarization $\boldsymbol{P}_{ij} \propto (\boldsymbol{S}_i \cdot \boldsymbol{e}_{ij})^2 \boldsymbol{e}_{ij}$ along the direction of the unit vector $\boldsymbol{e}_{ij}$ connecting the ion and ligand site [61]. Due to the squared term, the polarization does not depend on the sign of $\boldsymbol{S}_i$ and, thus, not on the direction of the spins relative to the *c*-axis. Therefore, the *d-p* hybridization mechanism should equally contribute to the polarization in the antiferromagnetic and the ferrimagnetic state [50], as in either case the spins are expected to point either along the positive or negative *c*-direction.

Besides, also a contribution from inverse Dzyaloshinskii-Moriya interaction to the polarization in $Fe_2Mo_3O_8$ was discussed [62]. This antisymmetric exchange interaction can lead to a displacement of the ligand atom as a consequence of an acentric spin structure [5]. If $\boldsymbol{e}_{ij}$ is the unit vector connecting the spins, the polarization induced by inverse Dzyaloshinskii-Moriya interaction is given by $\boldsymbol{P}_{ij} \propto \boldsymbol{e}_{ij} \times (\boldsymbol{S}_i \times \boldsymbol{S}_j)$ [61]. However, to be applicable for the $M_2Mo_3O_8$ compounds this would require mutually canted spins and therefore would imply a deviation from the proposed collinear magnetic structure.

In the $M_2Mo_3O_8$ compounds a variety of magnetoelectric effects can be observed. The presence or absence of certain effects in the different phases can be understood by means of the respective magnetic point group symmetry and the resulting magnetoelectric tensors. With the *z*-axis being the polar axis ($a, b, c = x, y, z$), in the paramagnetic state the magnetic point group is $6_z m_{xz} m_{yz}$. When entering the antiferromagnetic phase, due to the ordering of the spins the time reversal ($'$) has to be considered in the symmetry and the magnetic point group reads $6'_z m'_{xz} m_{yz}$ [50]. From this the optical property tensors are obtained by Neumann's principle. Both for the paramagnetic and the antiferromagnetic phase this results in the following form of $\hat{\chi}^\mathrm{me}$ and $\hat{\chi}^\mathrm{em}$:

$$\hat{\chi}^\mathrm{me} = \hat{\chi}^\mathrm{em} = \begin{pmatrix} 0 & \chi''_{xy} & 0 \\ -\chi''_{xy} & 0 & 0 \\ 0 & 0 & 0 \end{pmatrix} \tag{2.23}$$

As shown in section 2.2, the time reversal even components χ''_{xy} vanish in the zero frequency limit. Therefore, the antiferromagnetic phase does not allow the static linear magnetoelectric effect in magnetic fields $H \parallel c$. However, this symmetry still enables the second order magnetoelectric effect. Indeed, considerable second order magnetoelectric effect has been reported in the antiferromagnetic phase of $Co_2Mo_3O_8$ [51].

In the ferrimagnetic phase the magnetic point group is $6_z m'_{xz} m'_{yz}$ [50, 53, 63]. This yields the following magnetoelectric tensors:

$$\hat{\chi}^{\mathrm{me}} = \hat{\chi}^{\mathrm{em}} = \begin{pmatrix} \chi'_{xx} & \chi''_{xy} & 0 \\ -\chi''_{xy} & \chi'_{xx} & 0 \\ 0 & 0 & \chi'_{zz} \end{pmatrix} \tag{2.24}$$

Thus, this symmetry allows the linear magnetoelectric effect. Large linear magnetoelectric effects have been observed in the ferrimagnetic phases of $Mn_2Mo_3O_8$ [53], $Fe_2Mo_3O_8$ and Zn doped $Fe_2Mo_3O_8$ [50]. Furthermore, in $Fe_2Mo_3O_8$, which hosts several magneto-optical spin excitations [64], non-reciprocal gyrotropic birefringence was reported in the ferrimagnetic phase [63]. This phenomenon occurs via the dynamical magnetoelectric effect due to the diagonal components of $\hat{\chi}$ and causes a rotation of the polarization of the electromagnetic wave around its propagation direction.

In the course of this work nonreciprocal directional dichroism in $Co_2Mo_3O_8$ and $Fe_2Mo_3O_8$ has been studied intensively. This effect could be realized in the antiferromagnetically ordered phase by applying a magnetic field perpendicular to the c-axis. A magnetic field $H \perp c$ causes a canting of the spins away from the c-axis and, thus, induces a magnetization parallel to the applied field. As a consequence, crossed polarization and magnetization are present in the sample and the magnetic point group symmetry is reduced to $2'm'm$. This is equivalent to the case described in section 2.3 with the optical property tensors given by Eq. 2.15. In literature so far directional dichroism on the $M_2Mo_3O_8$ compounds has only been reported in $FeZnMo_3O_8$ [31]. In this case, a giant effect was already found in the paramagnetic phase, which is in contrast to previous observations of directional dichroism in magnetoelectrics.

Besides the magnon spectra and the directional dichroism, the phonon modes and the d-d transitions of $Fe_2Mo_3O_8$ and their coupling to orbital degrees of freedom were studied in detail within the scope of this work.

2.5. Lacunar spinels AM_4X_8

The lacunar spinels are the second class of type I multiferroic compounds studied in the course of this work. By infrared spectroscopy over a large series of compounds the systematics of phonons and electronic excitations have been investigated. In

the following, an introduction to the lacunar spinels, their structure and phase transitions as well as an overview on theoretical studies will be given.

The compounds of the lacunar spinel family have the chemical formula AM_4X_8, with A = Ga, Ge, Al; M = V, Mo, Nb, Ta; and X = S, Se [65–68]. Interestingly, these compounds can accommodate many different elements, especially transition metal ions from $3d$ to $5d$, while always adopting the same structure. The term "lacunar spinel" refers to the lack of every second A site atom compared to the normal spinels. Their structure can be derived from the normal spinel structure AM_2X_4 by removing every second A atom in a regular manner. In the normal spinel structure the M sublattice consists of corner-sharing tetrahedra forming the so-called pyrochlore lattice. Due to the vacancy of every second A site the M atoms are shifted along their $\langle 111 \rangle$ axes resulting in a network of alternating smaller and larger M_4 tetrahedra [69, 70], which is also known as the breathing pyrochlore lattice. This is illustrated in Fig. 2.6 (c), where the red arrows indicate the shifts of the M sites with respect to their positions in an ideal pyrochlore lattice. This breathing pyrochlore lattice may be interpreted as cubic lattice of electric monopoles and antimonopoles, associated with the larger and smaller tetrahedra, respectively. The ordering of the vacancies results in the cubic noncentrosymmetric lacunar spinel crystal structure with space group $F\bar{4}3m$, which is shown in Fig. 2.6 (a) and (b). It consists of only weakly linked AX_4 tetrahedral and M_4X_4 cubane molecular clusters [65, 67, 71], which are arranged in a NaCl manner.

The separated cubane M_4X_4 units are characteristic to the lacunar spinels. As illustrated in Fig. 2.6 (d), they contain tetrahedral M_4 clusters, which are the magnetic building blocks of the lacunar spinels. Due to the larger intercluster distances (e. g. V-V distance of 3.936 Å in GaV_4S_8 [68]) the electronic overlap between the clusters can be neglected in first approximation [72]. The smaller intracluster distances (e. g. V-V distance of 2.896 Å in GaV_4S_8 [68]) lead to the fact that the M_4 clusters constitute a unique molecular electron distribution with well defined local spin and can be described by a molecular orbital scheme [68, 73]. This cluster orbital scheme consists of six bonding orbitals, which are split into one a_1, two e and three t_2 levels in cubic T_d crystal symmetry, as illustrated in Fig. 2.7. Depending on the compound, these cluster orbitals are filled with either seven (GaV_4S_8, AlV_4S_8, GaV_4Se_8, $GaNb_4S_8$, $GaTa_4Se_8$), eight (GeV_4S_8) or eleven ($GaMo_4S_8$, $AlMo_4S_8$, $GaMo_4Se_8$) valence electrons. In each case the highest occupied t_2 cluster orbital is only partially filled and, thus, remains triply degenerate. Therefore, within the crystal-field scheme, the studied lacunar spinels are Jahn-Teller active. Depending on the compound, the orbital degeneracy is lifted by a symmetry-lowering structural Jahn-Teller distortion in the temperature range between 30 and 55 K.

In the systems where the cluster orbitals are occupied with seven electrons the M_4 tetrahedra get elongated along one of the threefold axes below the structural

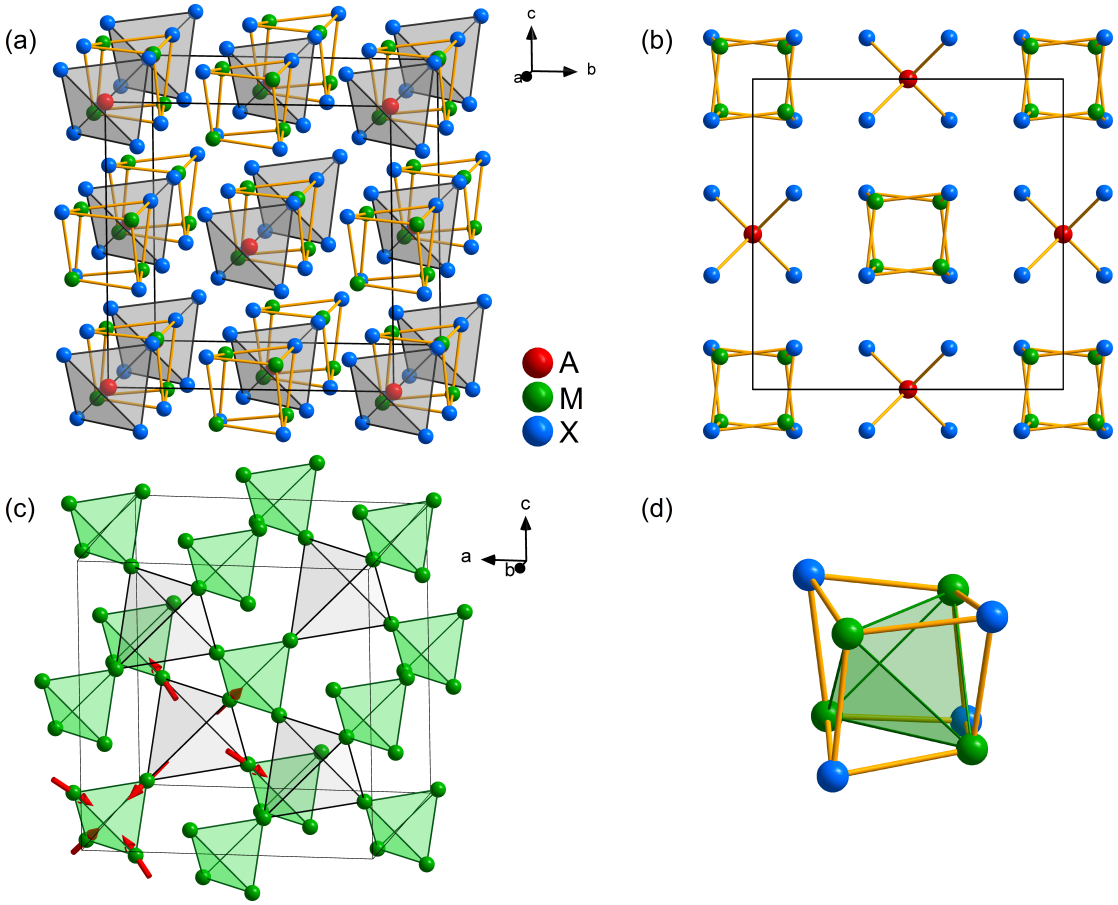

Figure 2.6.: (a) Crystal structure of the lacunar spinels AM_4X_8 in the high-temperature cubic phase (space group $F\bar{4}3m$). Tetrahedral AX_4 and cubane M_4X_4 clusters are arranged in a NaCl manner. (b) View of the crystallographic structure along the [100] direction, (c) Breathing pyrochlore lattice formed by the M sublattice [169]. The M sites are shifted with respect to the positions in an ideal pyrochlore lattice, as indicated by the red arrows. (d) Cubane M_4X_4 cluster. The tetrahedral M_4 cluster, being the magnetic building block of the lacunar spinels, is highlighted.

transition temperature T_{JT}, as shown in Fig. 2.6. In GaV_4S_8, AlV_4S_8 and GaV_4Se_8 this distortion is rhombohedral and reduces the symmetry of the tetrahedron to C_{3v}. As a consequence, the t_2 orbital is split into a lower a_1 level and two upper e levels, the orbital degeneracy is lifted and the single unpaired electron is stabilized in the a_1 level [68, 74]. In GaV_4S_8, AlV_4S_8 and GaV_4Se_8 for all tetrahedra in the unit cell this distortion takes place along the same cubic body diagonal, resulting in the rhombohedral space group symmetry $R3m$ [68, 75–77]. Typically, a multidomain structure is formed below T_{JT} [69].

Similarly, in $GaNb_4S_8$, $GaNb_4Se_8$ and $GaTa_4Se_8$ the elongation of the individual tetrahedra is nearly rhombohedral. However, in this case the unit cell becomes

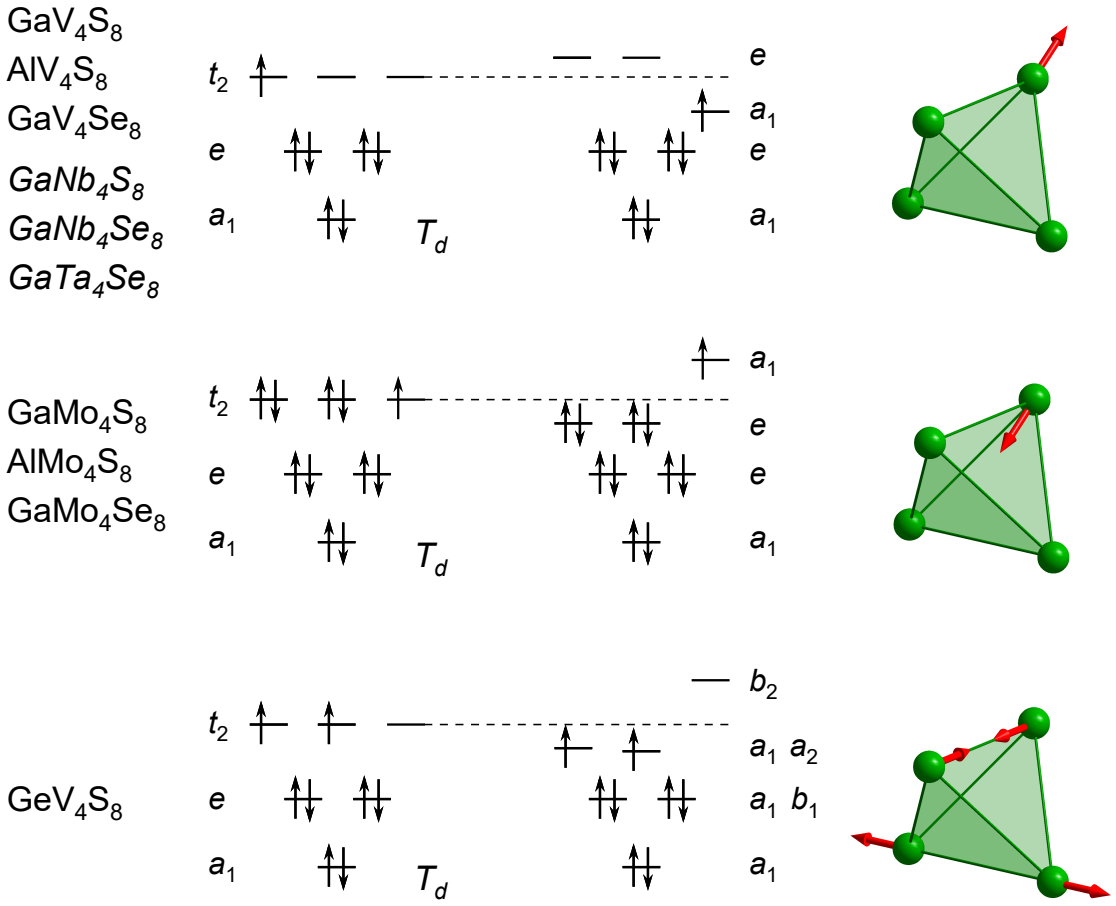

Figure 2.7.: Left: Cluster molecular orbital schemes of the studied lacunar spinels in the cubic T_d symmetry. Right: The Jahn-Teller distortion lifts the degeneracy of the t_2 orbital. The red arrows indicate the the main motif of the distortion of the M_4 tetrahedron. As described in the text, in the case of $GaNb_4S_8$, $GaTa_4Se_8$ and $GaNb_4Se_8$ despite of the tetragonal lattice symmetry, the distortion of the individual tetrahedra in the low-temperature phase is nearly rhombohedral, but the unit cell becomes four times larger, including four tetrahedra with four different directions of distortion.

four times larger, including four tetrahedral clusters distorting along four different cubic body diagonals [78–80]. For $GaNb_4S_8$ a tetragonal low-temperature structure with space group $P\bar{4}2_1m$ has been reported in literature so far [78], however, a recent study suggests that the actual symmetry might be even lower [81]. For $GaTa_4Se_8$, where previously also a tetragonal $P\bar{4}2_1m$ structure was claimed [79], a recent study reports that the low-temperature structure is well described by tetragonal space group $P\bar{4}m2$ [80]. In the case of $GaNb_4Se_8$ recently the structure has been reported to first change to cubic $P2_13$ and then to be further reduced to $P2_12_12_1$ below the magnetic transition [80].

For the compounds where the cluster molecular orbitals are filled with eleven electrons the situation is very similar to the filling with seven electrons. Instead of one unpaired electron, the t_2 orbital is now occupied by seven electrons or, in other words, by one hole. The occupation is quasi opposite and therefore also the rhombohedral distortion below T_{JT} [68]. The M_4 tetrahedra get compressed along one of the cubic body diagonals and the symmetry of the M_4 tetrahedra is again lowered to C_{3v}. The orbital degeneracy is lifted by splitting the t_2 orbital into two lower e levels and one upper a_1 level. For $GaMo_4S_8$, $AlMo_4S_8$ and $GaMo_4Se_8$ all tetrahedra within the unit cell distort long the same direction, which results in the rhombohedral space group symmetry $R3m$ [68, 82, 83].

In the case of GeV_4S_8, the cluster orbitals are occupied by eight electrons, with two unpaired electrons being on the t_2 levels, as shown in the lower part of Fig. 2.7. The degeneracy of the t_2 levels is lifted by a distortion of the M_4 tetrahedra with one V-V distance being reduced and the opposing V-V distance being elongated [75, 84, 85]. This reduces the symmetry of the cluster to C_{2v}. By the distortion the t_2 levels get split into two lower levels a_1 and a_2 filled with one unpaired electron each and one empty upper b_2 level, and also the e levels are split in a a_1 and b_1 level [75]. The resulting space group of GeV_4S_8 below T_{JT} is orthorhombic $Imm2$.

From dielectric spectroscopy measurements the cubic-to-rhombohedral structural phase transition in GaV_4S_8, GaV_4Se_8 and $GaMo_4S_8$ has been characterized as disorder-to-order type transition [86–88], which implies that a dynamic Jahn-Teller distortion is already present for temperatures well above T_{JT}. The scenario of a dynamical Jahn-Teller distortion has also been discussed in connection with GeV_4S_8 [89].

All of the studied lacunar spinels also undergo magnetic ordering, which usually happens at temperatures T_{C} lower than T_{JT}. Only for $GaNb_4S_8$ and $GaTa_4Se_8$, which adopt a tetragonal low-temperature phase, the structural and magnetic transitions occur concomitantly. For these two compounds a spin singlet state has been proposed [90–92]. The structural phase transition temperatures T_{JT}, the low-temperature structure, the magnetic phase transition temperature T_{C} and the types of magnetic ordering of the studied compounds are summarized in Tab. 2.1. Complex low-temperature magnetic phase diagrams have been found in GaV_4S_8, GaV_4Se_8 and $GaMo_4S_8$, which are hosting cycloidal order and a Néel-type skyrmion lattice [69, 93–96].

The highly correlated lacunar spinels have drawn high experimental and theoretical research interest due to the large variety of physical phenomena they are hosting. Pressure-induced superconductivity [74, 103, 104], bandwidth-controlled metal-to-insulator transitions [105, 106], resistive switching [107–109], large negative magnetoresistance [110], a two-dimensional topological insulating state [111], orbital order induced ferroelectricity and strong magnetoelectric effects [85] have

Table 2.1.: Summary of the structural transition temperature T_{JT}, low-temperature structure, magnetic phase transition temperature T_C and the types of magnetic order realized in the respective lacunar spinel compound. fm, afm, cyc and SkL denote ferromagnetic, antiferromagnetic, cycloidal and skyrmion lattice phases, respectively.

	T_{JT} (K)	low T struct.	T_C (K)	magnetic order	Literature
GaV_4S_8	44	$R3m$	13	cyc, SkL, fm	[69, 97]
GeV_4S_8	30	$Imm2$	15	afm	[67, 75, 84, 98]
$GaMo_4S_8$	45	$R3m$	20	cyc, SkL, fm	[82, 94, 99, 100]
$GaNb_4S_8$	32	$P\bar{4}2_1m$	32	spin singlet	[78, 90, 91]
AlV_4S_8	40	$R3m$	10	fm	[77]
$AlMo_4S_8$	45	$R3m$	12	fm	[83, 101]
GaV_4Se_8	41	$R3m$	18	cyc, SkL, fm	[76, 93]
$GaMo_4Se_8$	54	$R3m$	25	fm	[83, 99, 100, 102]
$GaTa_4Se_8$	53	$P\bar{4}m2$	53	spin singlet	[79, 80, 92]

been found. For example in GaV_4S_8 and GaV_4Se_8 besides the ferroelectric polarization emerging at the Jahn-Teller transition, excess polarization in the cycloidal and Skyrmion lattice phases has been observed experimentally [87, 112].

From the theory side, however, reproducing the electronic structure is still a challenge, especially for the high-temperature cubic state. From a simple electron counting for the lacunar spinels a metallic behavior would be expected due to the fractional occupation of the M_4X_4 cluster orbitals [113, 114]. However, most lacunar spinel compounds have been found to be semiconductors. This illustrates the importance of electron-electron correlations [113]. As a consequence of their semiconducting nature and due to the M_4 cluster formation the lacunar spinels have been classified as Mott insulators [68,75,114], with the on-site Coulomb repulsion U preventing the hopping of the electrons between the clusters [67]. Indeed, the electrical conductivity of GaV_4S_8 can be described by the Mott variable-range hopping mechanism [115] at low temperatures, while above T_{JT} thermal activated behavior was found [97].

In lacunar spinels typically band gaps in the range of 0.2 - 0.4 eV are found [107]. However, it has been shown by various theoretical studies that standard density functional theory (DFT) is not capable of opening the experimentally observed band gap in the cubic $F\bar{4}3m$ phase [67, 74, 89, 113, 114, 116–118]. Only by imposing a symmetry lower than cubic these standard DFT+U calculations are able to open a band gap at E_F [74, 75, 78, 89, 117]. Calculations for the rhombohedral $R3m$ low-temperature structure with usual values of $U \approx 2$ - 3 eV are able to reproduce the

band gap in lacunar spinels, e. g. in GaV_4S_8 [75,117]. From LDA+U calculations a rather large $U = 6\,\text{eV}$ has been reported for $GaNb_4S_8$ [74]. Although not applicable for the cubic state, these studies demonstrate the impact of lattice distortions on the electronic structure of the lacunar spinels. This is further confirmed by DFT studies of the rhombohedral $R3m$ phases of GaV_4S_8, $GaMo_4S_8$ and $GaMo_4Se_8$, where a band gap could be opened alone by structural distortions even in the absence of Coulomb interactions U [117, 119].

While standard DFT methods fail to predict the semiconducting state in the cubic phase and instead result in a metallic state, a recent theoretical study on GaV_4S_8 utilizing molecular orbital cluster dynamical mean field theory (cluster DMFT) could reproduce the observed band gap [114]. This investigation suggests that the molecular orbital approach is substantial for the description of the electronic structure of lacunar spinels in the cubic phase. Similarly, by DMFT with $U = 1.2\,\text{eV}$ the band gap as well as the insulator to metal transition could be reproduced in $GaTa_4Se_8$ [106]. Moreover, in a study comparing the performance of different exchange-correlation potentials a gap could be opened in GaV_4S_8, $GaMo_4S_8$, $GaNb_4Se_8$ and $GaTa_4Se_8$ when using the Perdew-Burke-Ernzerhof (PBE) functional and taking into account both spin-orbit coupling and on-site Coulomb interaction of $U = 2$ - $3\,\text{eV}$ [117].

As already mentioned, the structural distortions of the clusters, which occur due to the Jahn-Teller effect, play an important role for the modeling of the electronic structure of the lacunar spinels. Besides, the cluster orbitals are influenced by spin-orbit coupling and therefore also the electronic structure, as the hopping of the electrons from cluster to cluster strongly depends on the form of the cluster orbitals. In addition, the electronic structure is also affected by the magnetic ground state. This is best illustrated in the case of $GaNb_4S_8$, where the formation of a spin singlet state occurs concomitantly with the structural phase transition from the cubic to the tetragonal phase [78, 91]. The large number of different magnetic ground states found in lacunar spinels, such as ferromagnetic, antiferromagnetic, cycloidal, Néel-type skyrmion lattice and spin singlet states [69,90–94,120,121] also indicates a delicate balance of competing magnetic interactions and their strong dependence on the electronic structure, which makes the theoretical modeling of the band structure a great challenge.

Broadband infrared spectroscopy measurements on a wide series of lacunar spinels have been performed in the course of this work. The compounds GaV_4S_8, GeV_4S_8, $GaMo_4S_8$, $GaNb_4S_8$, AlV_4S_8, $AlMo_4S_8$, GaV_4Se_8, $GaMo_4Se_8$ and $GaTa_4Se_8$ have been studied. The broadband optical conductivity provides an insight into the electronic structure of these compounds and may give an experimental basis for future theoretical studies. Besides tracing substitutional effects on the size of the band gap, the systematic replacement of the ions at the A, M and the ligand

sites allows an assignment of the infrared-active phonon modes to the individual structural units of the lacunar spinels.

3. Experimental techniques

In the following chapter the experimental techniques and methods of optical spectroscopy used in this work will be explained. By means of Terahertz time domain and Fourier-transform spectroscopy a broad frequency range from 0.1 to 600 THz could be covered. The working principle of these two spectroscopic techniques will be introduced and the determination of material parameters from the experimental data will be elaborated. Furthermore, an overview of the sample preparation is given.

3.1. Terahertz time-domain spectroscopy

In optical spectroscopy THz radiation typically refers to the frequency range from approximately $0.1 - 10$ THz, which is located in the gap between the range of classical dielectric and FIR spectroscopy [122, 123]. For a long time this frequency region, also known as the "THz gap" [124], was merely difficult to access, for example by backward-wave oscillators (BWOs) [125–127]. However, progress on the field of ultrafast pulsed lasers opened a new possibility for the generation and detection of THz radiation [128] based on photoconductive switching [129–132], which led to the development of terahertz time-domain spectroscopy (THz-TDS). Today, besides fundamental research, THz spectroscopy has a wide field of applications, e.g. in biological and pharmaceutical industry, imaging or security checks [133, 134]. In solid state physics THz-TDS can be used for the investigation of low-energy excitations, like soft modes of ferroelectrics, energy gap and quasiparticle excitations in superconductors, relaxational modes or, as done in the course of this work, phonon and magnon modes in highly correlated materials [135].

The experimental setup of a terahertz time-domain spectrometer is schematically illustrated in Fig. 3.1. The *Toptica TeraFlash* spectrometer used for the experiment contains an Er-Laser with a wave length of 1560 nm, which generates ultrashort laser pulses with a pulse length of 80 fs at a repetition rate of 100 MHz. By a beamsplitter the laser beam is split in two parts. The first part of the beam is directed to the THz emitter and is used for the generation of the THz radiation. It is focussed on the gap between the metallic contacts of the dipole antenna, which is evaporated on a semiconducting InGaAs substrate. With its photon energy being larger than the bandgap of the semiconducting substrate, the laser pulse creates electron-hole pairs in the material. Due to a bias voltage applied to the antenna

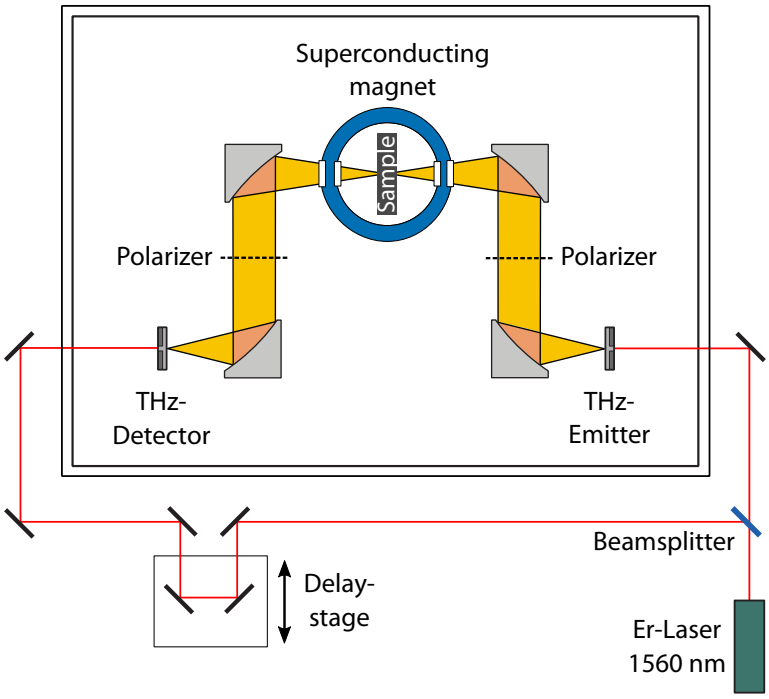

Figure 3.1.: Schematic illustration of the *TeraFlash* THz time-domain spectrometer, which is coupled to a 7 T superconducting magnet. The THz optics is placed inside a box purged with nitrogen to avoid unwanted absorption from water vapor.

the charge carriers are separated, resulting in a short current flow. According to the principle of the Hertzian dipole antenna, this pulsed photocurrent I_{PC} results in the emission of THz radiation. The electric field of the THz pulse is proportional to the time derivative of I_{PC} [128, 136, 137].

$$E(t) \propto \frac{\mathrm{d}I_{\mathrm{PC}}(t)}{\mathrm{d}t} \tag{3.1}$$

By off-axis parabolic mirrors the pulsed THz radiation generated by the emitter is focussed on the sample and the transmitted THz pulse is then focussed on the detector.

The working principle of the THz detection is very similar to that of the THz generation. The second part of the split laser beam is focussed on the detector. The laser pulse creates charge carriers in the semiconducting substrate and activates the detector. In contrast to the emitter, there is no voltage applied to the detector. Instead, the electric field of the incoming THz pulse separates the charge carriers and the resulting electrical current is measured. This current is proportional to the electric field. Since the detector is only active during the short fs laser pulse, the time dependence $E(t)$ of the electric field of the THz pulse can be measured by moving the delay stage, which allows to change the optical path length of the

second laser beam and, thus, the time delay between generation and detection of the THz radiation.

From the time dependent $E(t)$ the frequency dependent electric field $E(\omega)$ can be calculated by Fourier transformation [137]:

$$E(\omega) = |E(\omega)|e^{i\phi(\omega)} = \frac{1}{\sqrt{2\pi}} \int_{-\infty}^{+\infty} e^{-i\omega t} E(t)\, \mathrm{d}t, \tag{3.2}$$

where $\omega = 2\pi\nu$ denotes the angular frequency. For discrete measurement data instead a discrete Fourier transformation is used. As it is clear from Eq. 3.2, $E(\omega)$ is complex and also contains the phase $\phi(\omega)$. The phase sensitivity results from the measurement of $E(t)$ and is a great advantage over other techniques, such as Fourier-transform infrared spectroscopy (see section 3.2), which only measure intensity $|E|^2$ and, thus, are not capable of obtaining the phase information. As a consequence, the complex refractive index $\tilde{n}(\omega)$ can be directly calculated from THz-TDS measurements without the need of Kramers-Kronig transformation [135, 137, 138].

In the THz transmission experiments the time-domain signals of the sample $E_{\mathrm{sam}}(t)$ and a empty reference aperture $E_{\mathrm{ref}}(t)$ are measured and the frequency dependent complex spectra $E_{\mathrm{sam}}(\omega)$ and $E_{\mathrm{ref}}(\omega)$ are obtained by Fourier transformation. From this the complex transmission coefficient $t(\omega)$ is calculated according to [139, 140]

$$t(\omega) = \frac{E_{\mathrm{sam}}(\omega)}{E_{\mathrm{ref}}(\omega)} = |t(\omega)|e^{i\Delta\phi(\omega)}, \tag{3.3}$$

where $\Delta\phi(\omega) = \phi_{\mathrm{sam}}(\omega) - \phi_{\mathrm{ref}}(\omega)$ denotes the phase shift between sample and reference. The power transmission $T(\omega)$ is directly related to $t(\omega)$ and given by $T(\omega) = |t(\omega)|^2 = |E_{\mathrm{sam}}(\omega)|^2/|E_{\mathrm{ref}}(\omega)|^2$.

The complex refractive index $\tilde{n}(\omega) = n(\omega) + ik(\omega)$ can be directly calculated from the complex transmission coefficient. To relate $t(\omega)$ with $\tilde{n}(\omega)$ for a plane parallel sample of thickness d at normal incidence, the following contributions have to be taken into account: (i) The propagation of the THz beam within the sample, (ii) transmission through the sample interfaces and (iii) contributions from the Fabry-Pérot effect. Dependent on the sample thickness and transparency the latter can occur due to the interference of multiple reflected beams within the sample, leading to a periodic pattern in the measured spectrum. Considering these contributions and assuming that the sample is placed within a medium with $\tilde{n} = 1$, the complex transmission can be written as [122, 139, 141]

$$t(\omega) = \frac{4\tilde{n}(\omega)}{(\tilde{n}(\omega)+1)^2} \frac{\exp\left(-i(\tilde{n}(\omega)-1)\frac{\omega}{c}d\right)}{1 - \frac{(\tilde{n}(\omega)-1)^2}{(\tilde{n}(\omega)+1)^2}\exp\left(-2i\tilde{n}(\omega)\frac{\omega}{c}d\right)}. \tag{3.4}$$

A detailed derivation of Eq. 3.4 can be found in [139]. As this complex equation cannot be solved analytically, a numerical approach is followed. At first, starting values for $n(\omega)$ and $k(\omega)$ are estimated from the experimental $t(\omega)$. To obtain the actual $\tilde{n}(\omega)$, these starting values are iteratively modified until the calculated transmission matches the measured transmission data.

The complex refractive index is generally defined as $\hat{n}(\omega) = \sqrt{\epsilon(\omega)\mu(\omega)}$ [142]. For known $\tilde{n}(\omega)$, for nonmagnetic materials with magnetic permeability $\mu(\omega) = 1$ the complex dielectric permittivity $\epsilon(\omega) = \epsilon_1(\omega) + i\epsilon_2(\omega) = \tilde{n}^2(\omega)$ and the complex conductivity $\sigma(\omega) = \sigma_1(\omega) + i\sigma_2(\omega) = i\omega\epsilon_0(1-\epsilon)$ can be directly calculated. The real and imaginary parts are given by [141, 143]:

$$\begin{aligned} \epsilon_1(\omega) &= n^2(\omega) - k^2(\omega) & \sigma_1(\omega) &= \omega\epsilon_0\epsilon_2(\omega) \\ \epsilon_2(\omega) &= 2n(\omega)k(\omega) & \sigma_2(\omega) &= \omega\epsilon_0(1-\epsilon_1(\omega)) \end{aligned} \tag{3.5}$$

The absorption coefficient $\alpha(\omega)$ can be calculated from the imaginary part of the refractive index $k(\omega)$ [144]

$$\alpha(\omega) = \frac{2\omega k(\omega)}{c} \tag{3.6}$$

In the used experimental setup, the THz optics is placed inside a box purged with nitrogen in order to avoid unwanted absorption lines from water vapor. The laser is coupled to the emitter and detector by optical fibers. By the spectrometer the frequency range from 5 to 140 cm^{-1} can be covered. Two wire grid polarizers are placed in the THz beam, as shown in Fig. 3.1, to control the light polarization at the sample. The sample is placed inside a *Oxford Spectromag* superconducting magnet cryostat, which allows to measure in magnetic fields up to ± 7 T and at temperatures between 2 and 300 K. By rotating the magnet, measurements are possible with the magnetic field parallel (Faraday configuration) and perpendicular (Voigt configuration) to the beam direction.

3.2. Fourier-transform infrared spectroscopy

The second spectroscopic technique used in the course of this work is the Fourier-transform infrared (FTIR) spectroscopy. By this technique the spectral region from the far infrared (FIR) over the mid infrared (MIR) and near infrared (NIR) up to the visible range is covered. In FTIR spectroscopy broadband light sources are used. The frequency information is obtained by an interferometric principle and subsequent Fourier transformation, as will be elucidated in the following.

The interferometric principle of FTIR spectroscopy can be explained on the basis of the Michelson interferometer. Its applicability to spectroscopic measurements was already described by Michelson [145, 146], however, only later progress in computing made the development of FTIR spectrometers possible [147, 148]. A

Michelson interferometer is realized in the Bruker IFS66v/S spectrometer, which is schematically illustrated in Fig. 3.2. The beam coming from the source is split in two beams by the beamsplitter. One of the beams is directed to a fixed mirror, the other beam is directed to a movable mirror. The two reflected beams are recombined after the beamsplitter and interfere with each other. Due to the interference the intensity of the recombined beam depends on the relative path difference δ, also called retardation, of the two beams reflected at the fixed and the movable mirror. The retardation $\delta = 2x$ can be varied by changing the position x of the movable mirror. The intensity measured at the detector as a function of δ is called interferogram $I(\delta)$.

At first the ideal simple case of a monochromatic source with wave length λ_0 is considered. If I_0 is the intensity of the two equally split beams, the variation of δ results in a cosine-shaped interferogram $I(\delta)$ [147–149]:

$$I(\delta) = I_0 \left(1 + \cos(2\pi\tilde{\nu}_0\delta)\right) \tag{3.7}$$

Here $\tilde{\nu}_0$ denotes the wave number, which is defined as the inverse wave length $\tilde{\nu}_0 = 1/\lambda_0$. The wave number is a commonly used frequency unit in optical spectroscopy and usually given in the units of cm^{-1}. The interferogram $I(\delta)$ consists of a dc and an ac component. For spectroscopy only the ac component of Eq. 3.7 is important, therefore, the dc component is omitted in the following.

For broadband sources with spectrum $S(\tilde{\nu})$ the interferogram is given by the integration over all frequencies [149]:

$$I(\delta) = \int_{-\infty}^{+\infty} S(\tilde{\nu}) \cos(2\pi\tilde{\nu}\delta)\, \mathrm{d}\tilde{\nu} \tag{3.8}$$

From the mathematical point of view, the interferogram $I(\delta)$ is the cosine Fourier transform of the spectrum $S(\tilde{\nu})$. Therefore, $S(\tilde{\nu})$ can be obtained from $I(\delta)$ by the inverse transform:

$$S(\tilde{\nu}) = \int_{-\infty}^{+\infty} I(\delta) \cos(2\pi\tilde{\nu}\delta)\, \mathrm{d}\delta \tag{3.9}$$

In reality the interferogram $I(\delta)$ cannot be measured with infinite retardation δ, as required in Eq. 3.9. The experimental limitation of δ results in a finite frequency resolution of the spectrum. The maximum resolution is given by $\Delta\tilde{\nu} = 1/\delta$ [151]. Hence, a higher resolution can be achieved by a larger displacement of the moving mirror.

For the FTIR measurements performed in the course of this work, mainly the two Bruker spectrometers IFS66v/S and IFS113v were used, which are schematically

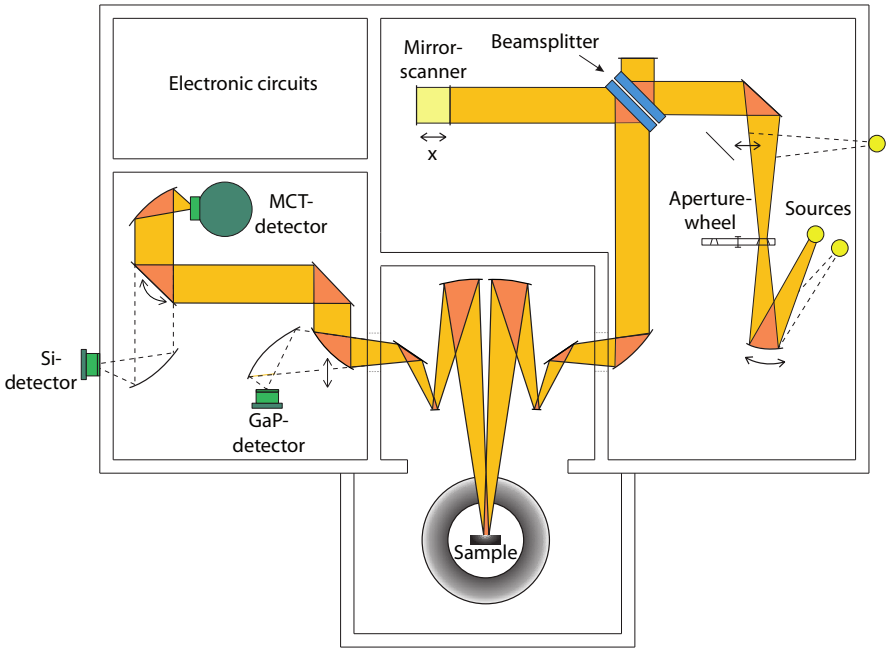

Figure 3.2.: Schematical illustration of the Bruker IFS66v/S spectrometer in reflectivity configuration. The beam is modulated in the Michelson interferometer and directed to the sample. The reflected beam is directed to the detector chamber. Adapted from Ref. [150].

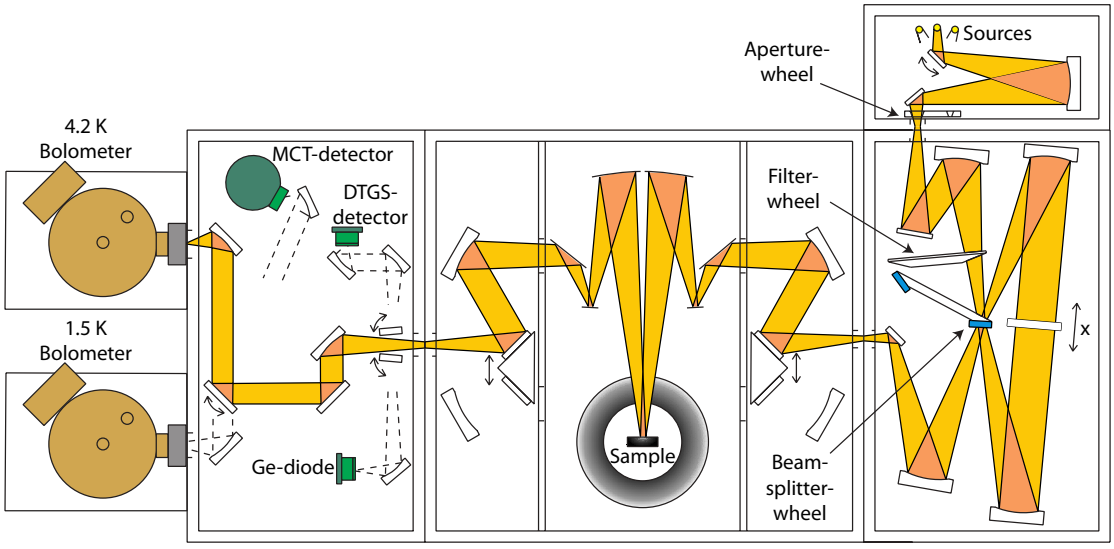

Figure 3.3.: Schematical illustration of the Bruker IFS113v spectrometer in reflectivity configuration. In this spectrometer a Genzel interferometer is realized. Adapted from Ref. [150].

illustrated in Figs. 3.2 and 3.3, respectively. The main difference between these two spectrometers is that the IFS113v uses a Genzel interferometer, where the two interfering beams are reflected on the two sides of the same mirror. Compared to the Michelson interferometer, twice the retardation and, thus, resolution can be achieved by the same mirror displacement. Measurements on small samples with sizes below 1 mm were performed on a similar Bruker Vertex80v spectrometer, which was coupled to a Hyperion IR microscope (not shown). By a set of different sources (Hg lamp, globar, tungsten halogen lamp), beamsplitters and detectors (Bolometer, MCT-detector, Si-diode) the spectral range from 100 to 20000 cm^{-1} is covered. The samples are placed inside CryoVac He-flow cryostats, which allow to measure at temperatures between 10 and 300 K.

As for the studied single crystalline samples the transmission is low in the infrared range, the FTIR measurements were mainly performed in reflectivity configuration. To determine the reflectivity $R(\omega)$, the reflected intensities of the sample and of a reference are measured. As a reference gold or silver mirrors are used. $R(\omega)$ is given by

$$R(\omega) = \frac{I_{\mathrm{sam}}(\omega)}{I_{\mathrm{ref}}(\omega)} = |r(\omega)|^2, \tag{3.10}$$

where $r(\omega)$ is the complex reflectivity coefficient, which is introduced as:

$$r(\omega) = \sqrt{R(\omega)} e^{i\phi(\omega)}. \tag{3.11}$$

$\phi(\omega)$ denotes the phase shift between the reflected and the incident wave. The reflectivity of a sample depends on the complex refractive index. For a beam coming from a medium with $\tilde{n}'(\omega) = 1$ the reflectivity coefficient $r(\omega)$ at normal incidence is given by the following relation [144]:

$$r(\omega) = \frac{\tilde{n}(\omega) - 1}{\tilde{n}(\omega) + 1} \tag{3.12}$$

Therefore, $\tilde{n}(\omega)$ can be directly calculated from $r(\omega)$. However, as by FTIR spectroscopy only intensities can be measured, only $R(\omega)$ is experimentally accessible, while $\phi(\omega)$ can not be determined in the experiment.

This problem can be overcome by a Kramers-Kronig transformation. Based on the principle of causality [152] the Kramers-Kronig relations [153, 154] allow to calculate the real part of complex linear response functions from the imaginary part, and vice versa. Applied to $\ln r(\omega) = \ln\sqrt{R(\omega)} + i\phi(\omega)$ this yields [155–158]

$$\ln\sqrt{R(\omega)} = -\frac{2}{\pi}\mathcal{P}\int_0^\infty \frac{\omega'\phi(\omega')}{\omega^2 - \omega'^2}\,\mathrm{d}\omega' \tag{3.13}$$

and

$$\phi(\omega) = \frac{2\omega}{\pi}\mathcal{P}\int_0^\infty \frac{\ln\sqrt{R(\omega')}}{\omega^2 - \omega'^2}\,\mathrm{d}\omega'. \tag{3.14}$$

$\mathcal{P}$ denotes the principal value of the Cauchy integral. To avoid the singularity at $\omega' = \omega$ the Cauchy integral in Eq. 3.14 can be rewritten, as shown in Ref. [155]:

$$\phi(\omega) = \frac{\omega}{\pi}\int_0^\infty \frac{\ln R(\omega') - \ln R(\omega)}{\omega^2 - \omega'^2}\,\mathrm{d}\omega'. \tag{3.15}$$

According to Eq. 3.15, the phase $\phi(\omega)$ can be calculated, if the reflectivity $R(\omega)$ is known over the complete frequency range from 0 to ∞. As this cannot be realized experimentally, an extrapolation of the measurement data towards low and high frequencies is required. For the studied non-metallic samples a constant extrapolation of $R(\omega)$ can be used at the low-frequency side of the experimental spectrum. Towards high frequencies the experimental reflectivity is commonly continued steadily by a power-law extrapolation $R(\omega) \propto \omega^{-s}$ [159]. For even higher energies (above $\approx 100\,\mathrm{eV} \mathrel{\hat{=}} 8 \cdot 10^5\,\mathrm{cm}^{-1}$) the reflectivity can be described by an extrapolation $R(\omega) \propto \omega^{-4}$ [160].

3.3. Sample preparation

The samples studied in this work were synthesized by Dr. Vladimir Tsurkan and Dr. Lilian Prodan. After a description of the sample synthesis and crystal growth, it will be elucidated how the single- and ploy-crystalline samples were prepared for the optical measurements.

3.3.1. Mo oxides $M_2Mo_3O_8$

Polycrystalline $Fe_2Mo_3O_8$ was synthesized from the binary oxides FeO (99.999 %) and MoO_2 (99 %) by repeated annealing in evacuated quartz ampoules at a temperature of 1000 °C. For the preparation of polycrystalline $Fe_{1.86}Zn_{0.14}Mo_3O_8$, FeO was partly substituted with the respective amount of ZnO. For preparing polycrystalline $Co_2Mo_3O_8$, FeO was substituted by CoO. The single crystalline $M_2Mo_3O_8$ samples were grown at temperatures between 950 and 900 °C by the chemical transport reaction method. Anhydrous $TeCl_4$ was used as the transport agent. Crushed single crystals were analyzed by x-ray diffraction. This confirmed the single-phase composition with hexagonal space group $P6_3mc$. By squid magnetometry the antiferromagnetic ordering reported in the literature could be confirmed.

Optical spectroscopy measurements were performed on *ab*- and *ac*-cut samples. As the single crystals mainly grow in a hexagonal shape, the *ab*-plane can be

identified with the hexagonal surface of the crystal, with the *a*-direction being parallel to the edges of the hexagon. Thus, *ac*-cut samples were obtained by cutting crystals perpendicular to the *ab*-plane.

Reflectivity measurements were performed in the IR range on $Fe_2Mo_3O_8$ and $Fe_{1.86}Zn_{0.14}Mo_3O_8$. The reflectivity of *ab*-cut single crystals was measured on as-grown sample surfaces. For the polarization dependent *ac*-cut measurements the cut surface was polished to optical flatness. In the THz range the transmission was measured for $Co_2Mo_3O_8$, $Fe_2Mo_3O_8$ and $Fe_{1.86}Zn_{0.14}Mo_3O_8$. For this purpose the samples were polished to plane parallel slabs of appropriate thicknesses in the range between 0.5 and 1.5 mm.

For the reflectivity as well as the transmission measurements the samples were glued on circular apertures with diameters between 1.5 and 3 mm, dependent on the sample size. In the case of the *ac*-cut sample of $Fe_2Mo_3O_8$ a sufficient sample diameter of ≥ 1.5 mm could only be achieved by preparing a mosaic composed of two parts.

3.3.2. Lacunar spinels AM_4X_8

Polycrystalline samples of the lacunar spinels AM_4X_8 (with $A =$ Ga, Ge, Al, $M =$ V, Mo, Nb, Ta, $X =$ S, Se) were prepared from high-purity elements by solid state reactions by three repeated syntheses at temperatures from 800 to 1050 °C. The sample quality was checked by x-ray powder diffraction after each step of the synthesis. Single crystals were obtained by chemical transport reaction with iodine as transport agent.

The IR measurements on the lacunar spinels were mainly performed in reflectivity. The reflectivity spectra were measured on as-grown (111) surfaces of single crystalline samples of GaV_4S_8, GeV_4S_8, $GaMo_4S_8$, $GaNb_4S_8$, AlV_4S_8 and GaV_4Se_8. In the case of $GaMo_4S_8$, $GaNb_4S_8$, AlV_4S_8 and GaV_4Se_8 the obtained single crystals only had a limited size of less than 1 mm. Therefore, the measurements on these samples were carried out with the help of an IR microscope. In this case, half of the sample surface was evaporated with a 150 nm thick silver layer, which then was used for the reference measurement. For the single-crystalline $GaNb_4S_8$ sample with an effectively measurable area of only 0.15 mm in diameter, the absolute value of the reflectivity obtained from the microspectroscopy was not fully reliable. Therefore, a high-density polycrystalline pellet with a diameter of 4 mm was used to precisely determine the absolute value of the reflectivity in the FIR. The reflectivity of the single crystal was scaled accordingly.

In the case of $AlMo_4S_8$, $GaMo_4Se_8$ and $GaTa_4Se_8$ neither single crystals nor dense pellets were available for reflectivity measurements. For this reason, FIR transmission measurements were performed on polycrystalline samples embedded in polyethylene (PE) pellets. The pellets were prepared from PE powder, which was mixed with a suitable amount of the grounded polycrystalline sample. With

a heatable pressing tool this mixture was pressed with 25 kN at 130 °C for five minutes. Afterwards the pellet was annealed with released pressure at 150 °C for 25 minutes.

4. Magnon spectroscopy in multiferroics

In the following chapter the low-energy excitations in the magnetically ordered phases of the transition metal molybdenum oxides $M_2Mo_3O_8$ (M = Co, Fe, Zn) will be discussed, which have been investigated by magnetic field dependent THz-TDS experiments in the frequency range between 10 and 135 cm^{-1} (0.3–4 THz). In section 4.1, the results obtained on $Co_2Mo_3O_8$ will be presented in detail. The low-energy spectrum of $Co_2Mo_3O_8$ is found to be far more complex than expected for the reported magnetic structure. For some of the modes strong directional dichroism is observed. In section 4.2 a brief summary of the main results on $Fe_2Mo_3O_8$ and $Fe_{1.86}Zn_{0.14}Mo_3O_8$ will be given, which have been obtained in collaboration with Ana Strinić and Benjamin Csizi in the course of their Master- and Bachelor-theses, respectively. The results on $Fe_{1.86}Zn_{0.14}Mo_3O_8$ have been published in Ref. [57].

4.1. Forests of magnons, electromagnons and magnetoelectric excitations in $Co_2Mo_3O_8$

4.1.1. Magnon spectroscopy in magnetic fields

The low-energy spin excitations of the antiferromagnetically ordered phase of $Co_2Mo_3O_8$ have been investigated by THz transmission measurements. In Fig. 4.1 the frequency-dependent absorption coefficient, α, measured at 2 K in zero magnetic field is shown for the three different polarizations (a) $E^\omega \parallel a$ / $H^\omega \parallel b$; (b) $E^\omega \parallel a$ / $H^\omega \parallel c$ and (c) $E^\omega \parallel c$ / $H^\omega \parallel a$. The spectra obtained for $E^\omega \perp c$ exhibit an overall increase of the absorption towards high frequencies, limiting the experimentally accessible frequency range. This increase is already present at room temperature and gets more pronounced below T_N. Qualitatively similar spectra have also been observed in isostructural $Fe_2Mo_3O_8$ and $Fe_{1.86}Zn_{0.14}Mo_3O_8$ (see section 4.2). In the latter compounds the increase of the absorption towards high frequencies could clearly be ascribed to a low lying E_1 phonon, showing considerable narrowing below T_N (see section 5.1). Therefore, these findings suggest that also in $Co_2Mo_3O_8$ a phonon is located in this frequency range.

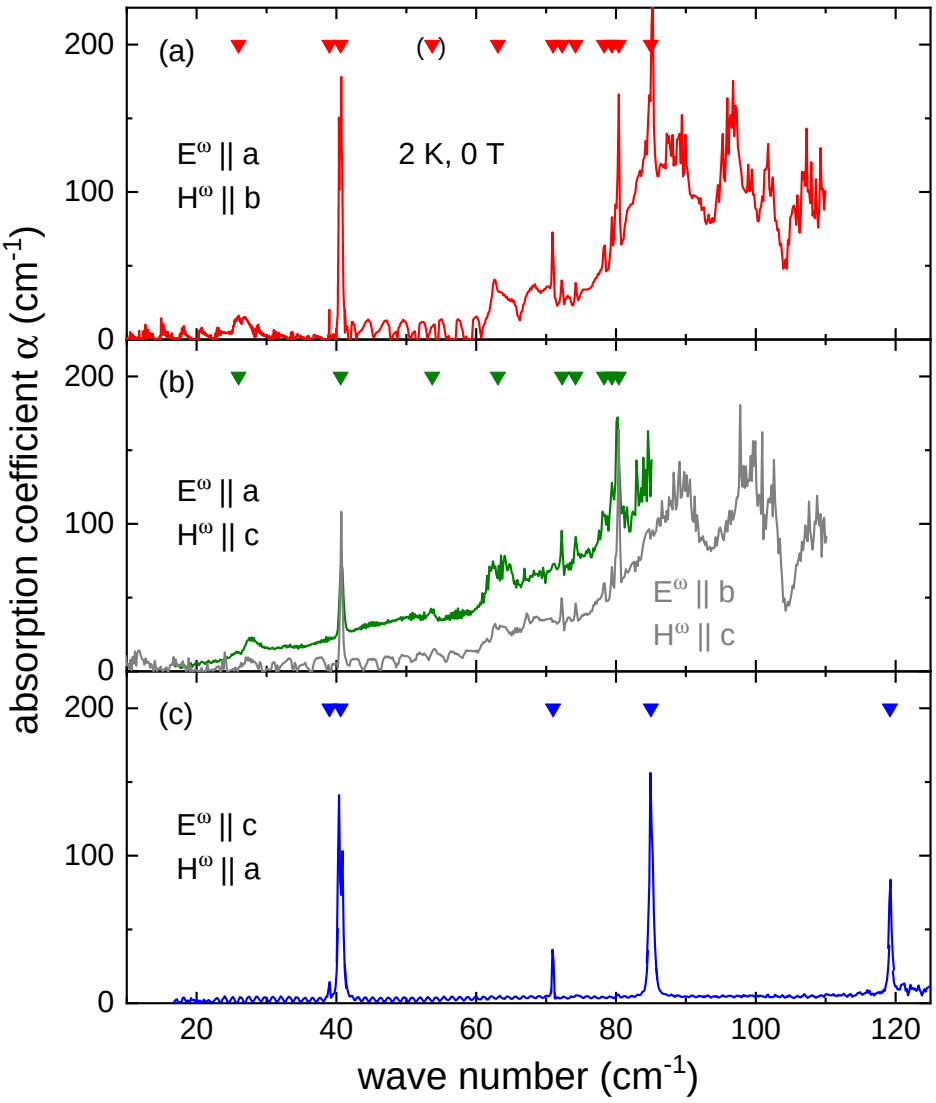

Figure 4.1.: Frequency dependence of the absorption coefficient α of $Co_2Mo_3O_8$ at $T = 2\,\mathrm{K}$ in zero magnetic field with polarization direction (a) $E^\omega \parallel a$ / $H^\omega \parallel b$, (b) $E^\omega \parallel a$ / $H^\omega \parallel c$ and $E^\omega \parallel b$ / $H^\omega \parallel c$, and (c) $E^\omega \parallel c$ / $H^\omega \parallel a$. The mode frequencies are indicated by the triangular symbols.

For the THz-TDS measurements the sample thickness was optimized in a way that the accessible frequency range is as wide as possible, while still preserving all excitations visible in the spectrum. Periodic fringes at the low-frequency side of some spectra result from multiple reflections of the THz-beam within the sample due to high transparency (Fabry-Pérot effect).

Several low-energy excitations emerge when entering the antiferromagnetically ordered phase. As will be shown later, these modes exhibit a magnetic field dependence and, thus, may be ascribed to magnon modes. For polarization $E^\omega \parallel a$ / $H^\omega \parallel b$ in the accessible frequency range twelve modes can be identified below T_N.

The two strongest modes are observed at 41 and 85 cm^{-1}. Modes of intermediate strength are found at 26, 63, 71 and 80 cm^{-1}. The spectral weight of the remaining modes is comparatively weak. Therefore, for better visibility all mode frequencies are indicated by triangles in Fig. 4.1. The spectrum obtained on an *ac*-cut for polarization $E^\omega \parallel a$ / $H^\omega \parallel c$ is qualitatively similar. In this case, nine modes are observed. Finally, in Fig. 4.1 (b) in addition the spectrum obtained on a *bc*-cut sample with polarization $E^\omega \parallel b$ / $H^\omega \parallel c$ is shown. Besides a slightly different baseline, it is in line with the spectrum obtained on the *ac*-cut, as expected from the hexagonal crystal symmetry. Indeed, polarization dependent measurements on an *ab*-cut sample have confirmed the isotropy within the *ab*-plane in zero magnetic field and for fields along the *c*-axis. Thus, the reproducible difference in the baseline may originate from the fact that the *ac*- and *bc*-cut samples stem from different batches. For polarization $E^\omega \parallel c$ / $H^\omega \parallel a$, the absorption spectrum does not exhibit a phononic background. In this case, five excitations are observed, with the two modes at 41 and 85 cm^{-1} dominating the spectrum.

In total, 14 modes could be observed in the antiferromagnetically ordered phase of $Co_2Mo_3O_8$ in $H = 0$. Table 4.1 summarizes the mode frequencies and denotes, for which polarization direction the respective modes are active. This allows to derive the selection rules, i. e. whether a mode is electric and/or magnetic dipole active along a certain direction. The selection rules are also included in Tab. 4.1. It turns out that all the modes for which the selection rule could be derived are active for E^ω and/or H^ω fields oscillating within the *ab*-plane. The modes at 39, 71 and the dominating mode 85 cm^{-1} are solely magnetic dipole active, i. e. they are classified as conventional magnons. The second dominating mode located at 41 cm^{-1} is found to be both magnetic and electric dipole active and, thus, classified as a magnetoelectric resonance. The further weak excitations are purely electric dipole active and therefore may be considered as electromagnons. Due to the limited accessible frequency range in the $E^\omega \perp c$ configurations the selection rules for the modes at 98 and 119 cm^{-1} could not unambiguously be determined. The selection rules obtained in zero field remain also valid in magnetic fields $\boldsymbol{H} \parallel c$, which causes a linear splitting of the modes, as will be discussed later.

In the linear spin-wave theory for $S = 1/2$, the number of magnon modes is equal to the number of magnetic sublattices [161]. This rule of thumb is widely accepted also for $S > 1/2$, though in that case it only captures $\Delta S = \pm 1$ transitions. Along this line, for the reported four-sublattice easy-axis collinear antiferromagnetic structure, four magnon modes would be expected. In this case, in zero magnetic field two doubly degenerate modes should be observed, which split linearly under magnetic field applied along the easy axis. In zero field, indeed two magnon modes are observed by inelastic neutron scattering (INS), as shown in Fig. 4.3, which will be discussed later in detail. It is obvious from the spectra shown in Fig. 4.1 that far more modes are observed in $Co_2Mo_3O_8$ in the THz-TDS measurements. On

Table 4.1.: Summary of the mode frequencies of $Co_2Mo_3O_8$ in zero magnetic field, mode activity for the three different polarizations and corresponding selection rules. The presence or absence of a mode in a certain polarization direction is indicated by ✓ and ×, respectively. (✓) denotes a mode that could not be identified unambiguously. When the experimental observation of a mode was not possible due to the low transmission, this is indicated by n.r. (not resolved). Under magnetic field $\boldsymbol{H} \parallel c$ the modes are split. g_l and g_u denote the g-factors determined for the lower and upper branch, respectively.

$H = 0\,\mathrm{T}$					$\boldsymbol{H} \parallel c$	
ω_0 (cm^{-1})	$E^\omega \perp c$, $H^\omega \perp c$	$E^\omega \perp c$, $H^\omega \parallel c$	$E^\omega \parallel c$, $H^\omega \perp c$	selection rule	g_l	g_u
26	✓	✓	×	$E^\omega \perp c$	0.58	0.44
39	✓	×	✓	$H^\omega \perp c$	1.68	1.48
41	✓	✓	✓	H^ω, E^ω	1.71	1.43
54	(✓)	✓	×	$E^\omega \perp c$ (?)	1.89	
63	✓	✓	×	$E^\omega \perp c$	3.57	4.25
71	✓	×	✓	$H^\omega \perp c$	0	0
72	✓	✓	×	$E^\omega \perp c$	3.29	2.94
74	✓	✓	×	$E^\omega \perp c$	3.52	3.50
78	✓	✓	×	$E^\omega \perp c$	3.51	3.06
79	✓	✓	×	$E^\omega \perp c$	3.60	
80	✓	✓	×	$E^\omega \perp c$	3.53	3.02
85	✓	×	✓	$H^\omega \perp c$	5.83	5.58
98	n.r.	✓	×	?	2.56	
119	n.r.	n.r.	✓	?	4.17	3.87

one hand, there is no experimental evidence that the magnetic ground state of $Co_2Mo_3O_8$ is more complicated. On the other hand, the optical measurements with V-shape splitting for $\boldsymbol{H} \parallel c$ and no discernible splitting for $\boldsymbol{H} \perp c$ also support the collinear easy-axis antiferromagnetic order. Moreover, the zero-field spectra are dominated by the two modes at 41 and $85\,\mathrm{cm}^{-1}$, which are also observed in the INS experiment.

In a next step the magnetic field dependence of the low-energy excitations in $Co_2Mo_3O_8$ is analyzed. For an easy-axis antiferromagnet the following behavior of the magnon modes is expected in magnetic field [161]: As already mentioned, under magnetic field applied parallel to the easy axis the modes exhibit a V-shape splitting: The degeneracy of the modes is lifted by the magnetic field as the different sublattices experience different enhanced or reduced effective fields. For

magnetic fields applied perpendicular to the easy axis only a weaker second-order splitting of the magnon modes is expected, which even may not be discerned in low fields.

The magnetic field dependence of the absorption spectra of $Co_2Mo_3O_8$ for fields $\boldsymbol{H} \parallel c$ up to 7 T is shown in Fig. 4.2 for the three different polarizations. Except for the excitation found at 71 cm^{-1} for $E^{\omega} \parallel c$ / $H^{\omega} \parallel a$, whose mode frequency is constant within the experimental accuracy, all other observed modes show a V-shape splitting in magnetic field, as indicated by the dashed lines in Fig. 4.2. The strength of the split modes is nearly equal for each polarization. Moreover, their strength does not depend on the field, leaving the selection rules derived for $H = 0$ intact. For magnetic fields $\boldsymbol{H} \perp c$ no splitting of the modes was found (see Figs. 4.4 and 4.5). Therefore, these findings from the field dependent measurements support the easy-axis character of the magnetic ground state of $Co_2Mo_3O_8$ with the c-axis being the easy axis.

The magnetic field dependence of the mode frequencies in $\boldsymbol{H} \parallel c$ is summarized for the three polarizations in Fig. 4.2 (d)-(f). For clarity reasons as well as in order to reflect the character of the absorption spectra in this mode map, the excitations have been classified in weak, medium strength and strong modes. The weak and narrow modes with absorption amplitude maxima up to approximately 10 cm^{-1} are only shown as dashed grey lines. Modes of intermediate strength are represented as small squares and colored dashed lines. The two strongest modes, clearly exceeding an absorption strength of 100 cm^{-1}, are located at 41 and 85 cm^{-1} in zero field and are represented as large circles and solid lines. From the linear splitting of the modes the g-factor can be determined for $\boldsymbol{H} \parallel c$. The g-factors of the lower (g_{l}) and upper (g_{u}) branches have been calculated separately from the slopes of the lines in Fig. 4.2 (d)-(f). The splitting of the modes is found to be mostly symmetric with the g-factors varying over a rather unusual wide range from 0.4 to 6. The g-factors of the single modes are summarized in Tab. 4.1.

To get further insight into the magnetic structure and the magnon excitations of $Co_2Mo_3O_8$, inelastic neutron scattering (INS) measurements were performed. These measurements were carried out by Dr. Somnath Ghara, Guratinder Kaur and Dr. Oksana Zaharko at the Paul Scherrer Institut (PSI) in Villigen, Switzerland, using the thermal neutron triple-axis spectrometer EIGER at the SINQ neutron source.

Figure 4.3 (a)-(c) shows the magnon dispersions along the $(h, 0, 0)$, $(h,0,-h)$ and (-1,0,l) directions obtained from INS energy scans in zero magnetic field. These measurements reveal two magnon modes at 5 and 10.5 meV, which clearly can be identified with the two strong modes located at 41 and 85 cm^{-1} dominating the THz spectra, as evident from Fig. 4.3, where INS and THz data share a common energy/frequency scale. The INS data exhibit slight dispersion along the h direc-

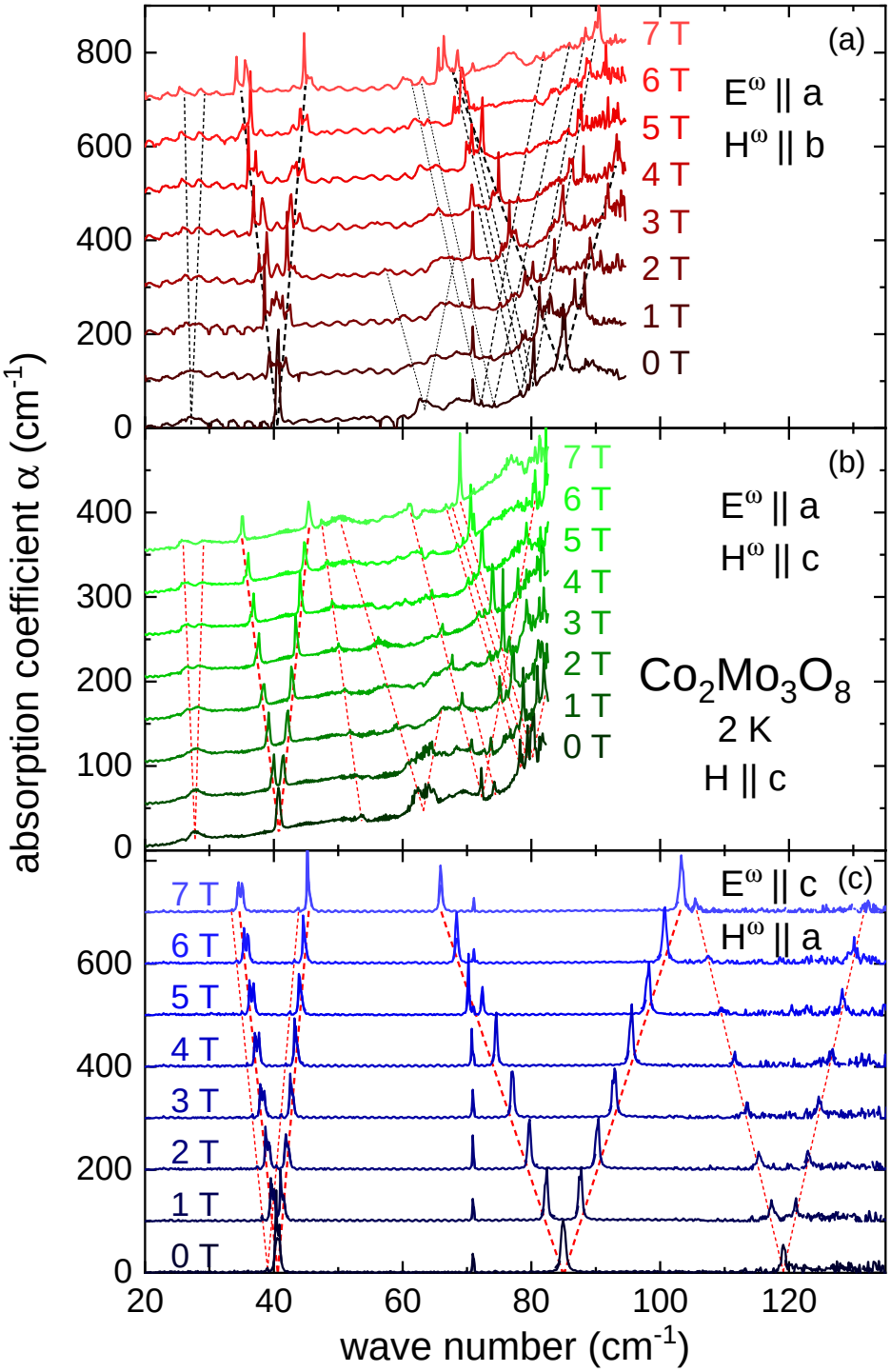

Figure 4.2.: Magnetic field dependence of the absorption spectra of $Co_2Mo_3O_8$ at $T = 2\,\mathrm{K}$ for polarization direction (a) $E^\omega \parallel a$ / $H^\omega \parallel b$, (b) $E^\omega \parallel a$ / $H^\omega \parallel c$ and (c) $E^\omega \parallel c$ / $H^\omega \parallel a$. For clarity, the curves are shifted by an offset in proportion to the magnetic field $\boldsymbol{H} \parallel c$. Dashed lines indicate the splitting of the modes in magnetic field.

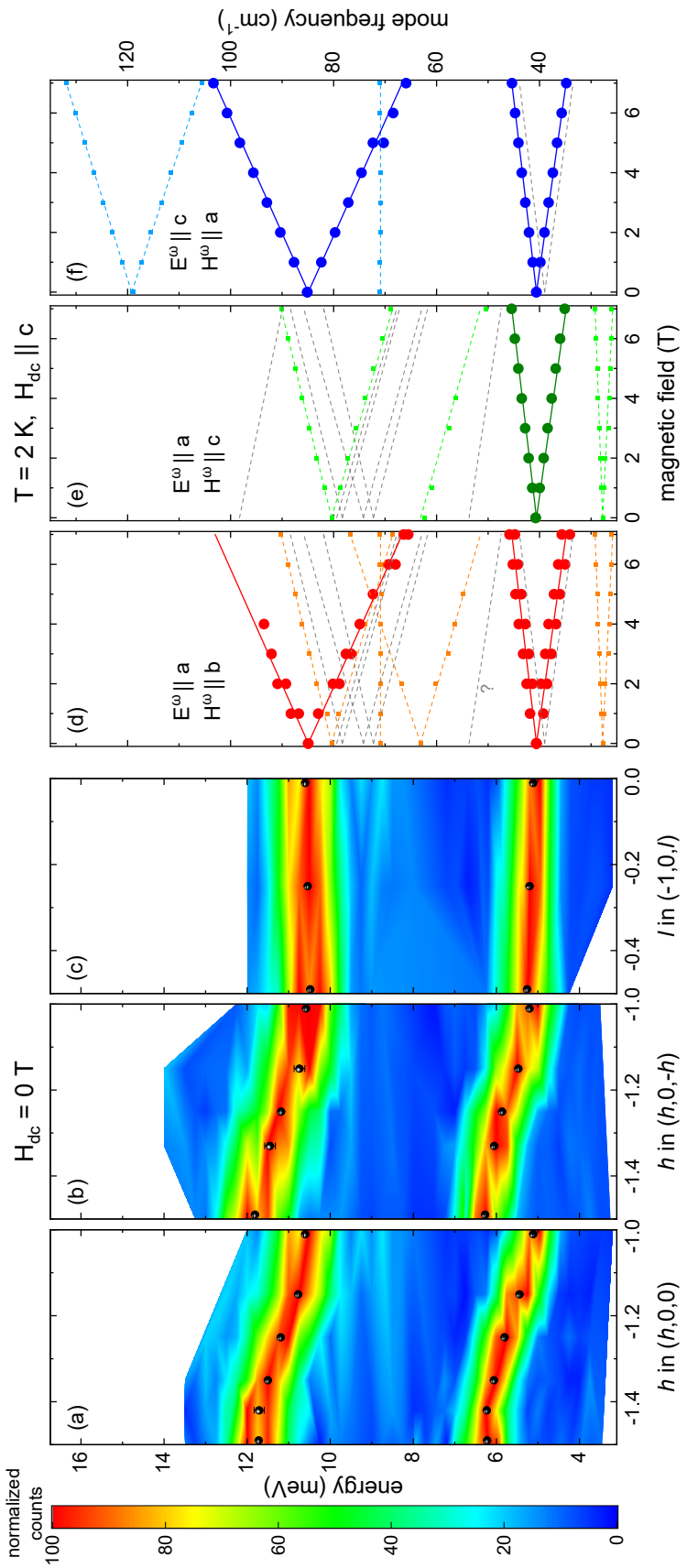

Figure 4.3: (a)-(c) Color plot of the dispersion of $Co_2Mo_3O_8$ obtained from inelastic neutron scattering (INS) along the (h,0,0), (h,0,−h) and (-1,0,l) direction. The black symbols indicate the peak positions of the respective energy scan. (d)-(f) Mode frequencies obtained from THz transmission measurements at 2 K as a function of magnetic field $\boldsymbol{H} \parallel c$. Large circles and solid lines indicate the strongest modes. Small squares and colored dashed lines denote modes of medium strength. The weakest modes are represented by grey dashed lines. For direct comparison, the data from INS and THz measurements share a common energy/frequency scale.

tion and along the diagonal (h,0,$-h$) direction, whereas along the l direction no dispersion can be observed.

The results from INS, with two magnon modes being observed in the magnetically ordered phase of $Co_2Mo_3O_8$, are in agreement with a four-sublattice easy-axis antiferromagnetic structure and give no evidence that the magnetic ground state is more complicated than reported previously. The observation of only two magnons by INS is not in contradiction with the large number of modes in the THz experiments, as the additional modes are considerably weaker. Moreover, the energy resolution of the INS measurements is lower than in the optical experiments. Therefore, the additional modes may just not be detectable by INS. Furthermore, as a fundamental difference, the matrix elements are different for the light absorption and for the INS process.

Concerning the unexpected large number of modes observed by THz spectroscopy, an easy way would be to ascribe them to a more complicated magnetic ground state with more than four sublattices. However, the field dependent optical measurements with $\boldsymbol{H} \parallel c$ and $\boldsymbol{H} \perp c$ support the easy-axis nature of the magnetic structure of $Co_2Mo_3O_8$. Furthermore, our colleagues revisited the magnetic structure of $Co_2Mo_3O_8$ by polarized and unpolarized neutron scattering and found no deviation from the four sublattice easy-axis antiferromagnetic structure. Therefore, if present at all, deviations from the four-sublattice easy-axis magnetic structure can be considered small.

The reason behind the large number of modes could be that not only the $\Delta S = \pm 1$ transitions are excited, as expected from the linear spin-wave theory, resulting in one mode per magnetic sublattice, but also transitions with $\Delta S = \pm 2$ or $\Delta S = \pm 3$ can be active and couple to light in $Co_2Mo_3O_8$. These transitions are usually silent in conventional magnets, as the magnetic dipole matrix element governing the dynamic magnetic susceptibility $\hat{\chi}^{\mathrm{mm}}(\omega)$ vanishes in such cases [162]. In the present case, the following conditions may release this selection rule: Co^{2+} realizes the $S = 3/2$ state and inversion symmetry is broken. $\Delta S = \pm 2, \pm 3$ transitions would also naturally explain the large g-factors up to $g = 6$.

A similar situation has been experimentally found and theoretically described in multiferroic $Ba_2CoGe_2O_7$ [162]: This compound also hosts Co^{2+} ions as magnetic ions with $S = 3/2$, which are located in tetrahedral oxygen coordination. Below $T_N = 6.7\,\mathrm{K}$, $Ba_2CoGe_2O_7$ adopts a two-sublattice antiferromagnetic structure [163–165]. In this compound, more than two magnon modes have been observed, in contrast to the prediction of the linear spin-wave theory. However, the conventional spin-wave theory is only valid, if the expectation values, i. e. the lengths, of the spins are preserved and the excitation only changes the orientation of the spins relative to the ground state [162]. To describe the additional excitations in $Ba_2CoGe_2O_7$, the authors of Ref. [162] developed a multiboson spin-wave theory including spin-stretching modes with an oscillating spin length. It was found that

the occurrence of additional magnetic excitations in $Ba_2CoGe_2O_7$ is closely linked to the presence of large single-ion anisotropy and that the noncentrosymmetric crystal structure can make these excitations electric dipole active [162]. It was stated that spin-stretching modes generally can emerge in compounds with $S > 1/2$ exhibiting large single-ion anisotropy or a noncentrosymmetric structure [162]. Therefore, it seems possible that also in the noncentrosymmetric $Co_2Mo_3O_8$ additional unconventional excitations may be identified as spin-stretching modes. However, to verify this hypothesis, along this line a detailed theoretical analysis of the low-energy excitations of $Co_2Mo_3O_8$ is required.

Finally, we propose a different scenario to explain the forest of magnon modes in $Co_2Mo_3O_8$. As will be outlined in section 4.2, also in the antiferromagnetically ordered phase of isostructural $Fe_2Mo_3O_8$ more excitations than the four expected magnon modes were observed by THz spectroscopy. All these low-energy excitations of $Fe_2Mo_3O_8$ are at least electric dipole active. Theoretical calculations [166] of the splitting of the ^5D ground term of the tetrahedral Fe^{2+} in $Fe_2Mo_3O_8$ revealed energies matching some of these modes, which therefore might rather be considered as electronic transitions than as magnon excitations. Thus, a similar scenario of low-lying electronic transitions might also be possible for some of the additional modes in $Co_2Mo_3O_8$, out of which most are purely electric dipole active. However, such calculations of the electronic levels supporting this statement are currently not available for $Co_2Mo_3O_8$.

4.1.2. Unidirectional transmission

The dynamical magnetoelectric effect in $Co_2Mo_3O_8$ was studied via the investigation of directional dichroism of magnon modes. As explained in detail in section 2.3, different absorption strengths can occur at magnetoelectric resonances for light beams propagating parallel or antiparallel to $\boldsymbol{T} = \boldsymbol{P} \times \boldsymbol{M}$. In $Co_2Mo_3O_8$ with ferroelectric polarization $\boldsymbol{P}$ along the c-axis this configuration can be achieved by the application of a magnetic field $\boldsymbol{H} \perp c$, which induces the necessary magnetization $\boldsymbol{M}$. Therefore, measurements of the directional dichroism were performed on an ac-cut sample in Voigt configuration with magnetic field applied along the a-direction. This results in magnetic point group symmetry $2'_z m'_{xz} m_{yz}$, which is the case discussed in section 2.3. Following Eqs. 2.18 - 2.21, the approximate four solutions of the Maxwell equations for the refractive indices n for the two different polarization directions are given by:

$$\begin{aligned} n_{ac}^{\pm \boldsymbol{k}} &\approx \sqrt{\epsilon'_{xx}\mu'_{zz}} \mp \chi'_{zx} \qquad \text{for } E^\omega \parallel a \;/\; H^\omega \parallel c, \\ n_{ca}^{\pm \boldsymbol{k}} &\approx \sqrt{\epsilon'_{zz}\mu'_{xx}} \pm \chi'_{xz} \qquad \text{for } E^\omega \parallel c \;/\; H^\omega \parallel a. \end{aligned} \tag{4.1}$$

As the reversal of the magnetic field, or the magnetization, corresponds to a time-reversal operation, it is equivalent to the reversal of the propagation

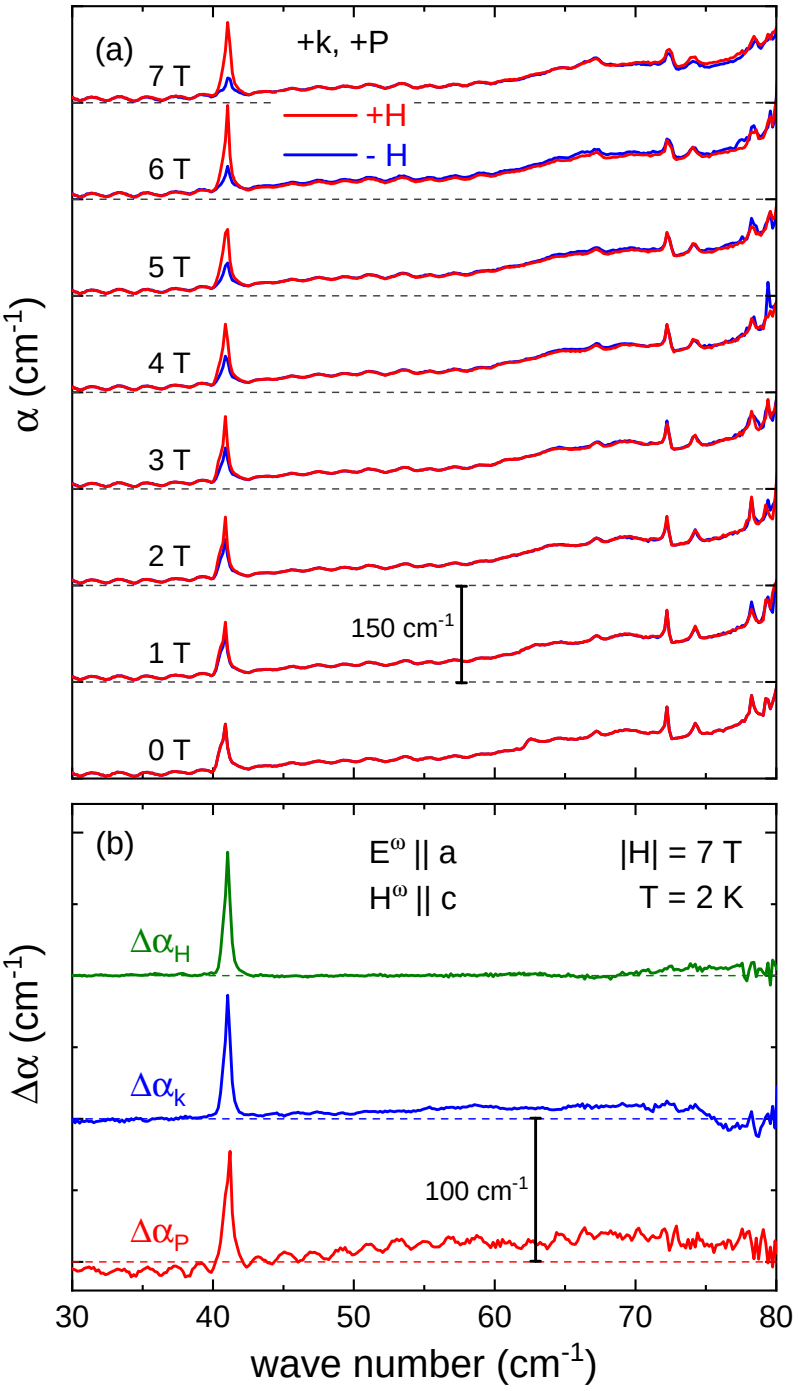

Figure 4.4.: (a) Magnetic field dependence ($\boldsymbol{H} \parallel a$) of the absorption spectra of $Co_2Mo_3O_8$ for polarization $E^\omega \parallel a$ / $H^\omega \parallel c$ measured at 2 K in $+\boldsymbol{k}$, $+\boldsymbol{P}$ configuration. Red and blue curves represent positive and negative magnetic fields, respectively. (b) Difference spectra $\Delta\alpha_H$, $\Delta\alpha_k$ and $\Delta\alpha_P$ at 2 K in $|H| = 7$ T. The spectra are shifted by a constant offset, as indicated by the dashed lines.

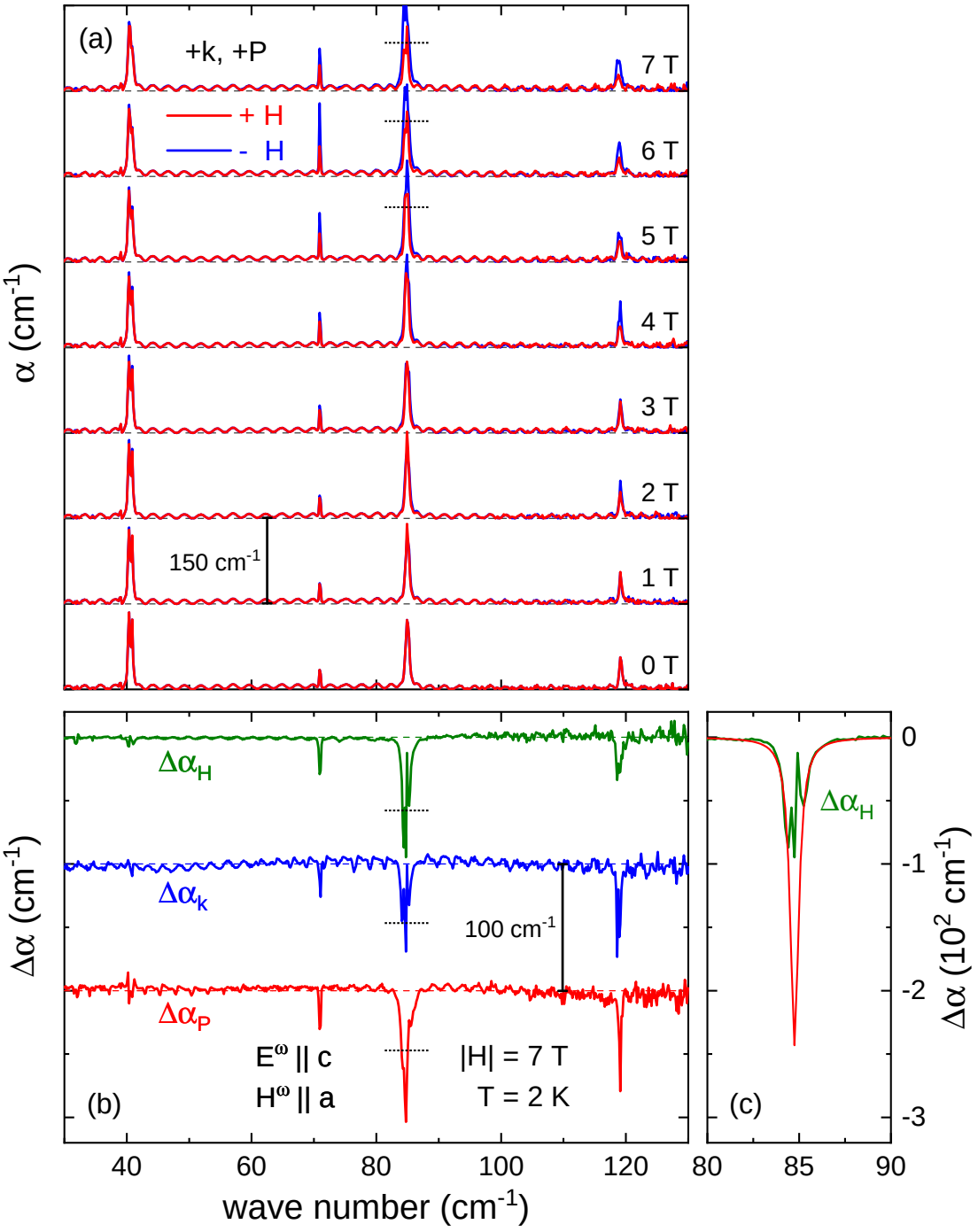

Figure 4.5.: (a) Magnetic field dependence ($\boldsymbol{H} \parallel a$) of the absorption spectra of $Co_2Mo_3O_8$ for polarization $E^{\omega} \parallel c$ / $H^{\omega} \parallel a$ measured at 2 K in $+\boldsymbol{k}$, $+\boldsymbol{P}$ configuration. Red and blue curves represent positive and negative magnetic fields, respectively. (b) Difference spectra $\Delta\alpha_H$, $\Delta\alpha_k$ and $\Delta\alpha_P$ at 2 K in $|H| = 7$ T. The spectra are shifted by a constant offset, as indicated by the dashed lines. Due to strong absorption the peak maximum of the 85 cm^{-1} could not be resolved, as indicated by the dotted lines across the peak. (c) Enlarged view of $\Delta\alpha_H$ of the 85 cm^{-1} mode. The red line represents a Lorentz fit, as described in the text.

direction $\boldsymbol{k}$. Therefore, the easiest way to experimentally detect directional anisotropy $\boldsymbol{k} \cdot (\boldsymbol{P} \times \boldsymbol{M})$ in $Co_2Mo_3O_8$ is to measure the absorption spectrum in positive and negative magnetic fields. Figure 4.4 (a) shows the field dependence of the absorption spectra for polarization $E^\omega \parallel a$ / $H^\omega \parallel c$ in positive (red) and negative (blue) magnetic fields $\boldsymbol{H} \parallel a$ up to $|H| = 7\,\mathrm{T}$. The propagation direction of the THz beam and the orientation of the ferroelectric polarization of this measurement are defined as the $+\boldsymbol{k}$ and $+\boldsymbol{P}$ direction, respectively. For this polarization, strong directional dichroism is observed for the mode located at $41\,\mathrm{cm}^{-1}$. For this mode the directional anisotropy caused by χ'_{zx} increases with magnetic field. While in positive magnetic fields the absorption strength of this mode is increased in field, the mode gets gradually suppressed in negative magnetic fields. In the remaining part of the spectrum no difference between the $\pm\boldsymbol{H}$ spectra is observed. Furthermore, all mode eigenfrequencies are independent of the magnetic field $\boldsymbol{H} \parallel a$, as expected for an easy-axis antiferromagnet with spins along the c-axis.

As it follows from the symmetry considerations, only the relative orientation of $\boldsymbol{k}$ and $\boldsymbol{T} = \boldsymbol{P} \times \boldsymbol{M}$ is relevant for the occurrence of directional dichroism. Thus, it is equivalent if either the propagation direction $\boldsymbol{k}$, the magnetization $\boldsymbol{M}$ or the orientation of the ferroelectric polarization $\boldsymbol{P}$ is reversed. Besides the measurements shown for $\pm\boldsymbol{H}$, also the $\pm\boldsymbol{k}$ and $\pm\boldsymbol{P}$ configurations have been investigated. For the reversal of the propagation direction $\boldsymbol{k}$ the THz source and detector were exchanged. The orientation of $\boldsymbol{P}$ can be reversed by a 180° rotation of the sample around the a- or b-direction. For a direct comparison of these three possible configurations, it is instructive to consider the difference spectra $\Delta\alpha$, which are defined as follows:

$$\begin{aligned} \Delta\alpha_H &= \alpha(+\boldsymbol{k}, +\boldsymbol{P}, +\boldsymbol{H}) - \alpha(+\boldsymbol{k}, +\boldsymbol{P}, -\boldsymbol{H}) \\ \Delta\alpha_k &= \alpha(+\boldsymbol{k}, +\boldsymbol{P}, +\boldsymbol{H}) - \alpha(-\boldsymbol{k}, +\boldsymbol{P}, +\boldsymbol{H}) \\ \Delta\alpha_P &= \alpha(+\boldsymbol{k}, +\boldsymbol{P}, +\boldsymbol{H}) - \alpha(+\boldsymbol{k}, -\boldsymbol{P}, +\boldsymbol{H}) \end{aligned} \tag{4.2}$$

The difference spectra $\Delta\alpha_H$, $\Delta\alpha_k$ and $\Delta\alpha_P$ for polarization $E^\omega \parallel a$, $H^\omega \parallel c$ in $|H| = 7\,\mathrm{T}$ are shown in Fig. 4.4 (b). As expected, all three curves nicely coincide, with $\Delta\alpha$ reaching a value of $85\,\mathrm{cm}^{-1}$. Slight deviations of the baseline from zero in $\Delta\alpha_k$ and $\Delta\alpha_P$ are ascribed to the necessary realignment of the optics when switching between $\pm\boldsymbol{k}$, or the dismounting of the sample when switching between $\pm\boldsymbol{P}$, respectively.

For the perpendicular polarization $E^\omega \parallel c$ / $H^\omega \parallel a$, the magnetic field dependent absorption spectra with $\boldsymbol{H} \parallel a$ are shown in Fig. 4.5 (a). Directional dichroism is observed for the modes located at 71, 85 and $119\,\mathrm{cm}^{-1}$. In this case, the directional anisotropy originates from the dynamical magnetoelectric effect via χ'_{xz}. For these modes, the absorption strength is enhanced in increasing negative fields and reduced in increasing positive fields. Although the sample thickness has already

been considerably reduced for the directional dichroism measurements, the peak maximum of the 85 cm^{-1} mode is not fully resolved due to its high absorption strength, as indicated by the dotted lines in Fig. 4.5.

In contrast to the previously shown polarization, for $E^\omega \parallel c$ / $H^\omega \parallel a$ the mode at 41 cm^{-1} does not show directional dichroism. The selective occurrence of directional anisotropy for a certain mode in only one polarization is possible, because the directional dichroism for the different polarization directions is governed by χ'_{zx} and χ'_{xz}, respectively (see Eqs. 4.1), which are independent components of the dynamical magnetoelectric susceptibility tensor due to the orthorhombic magnetic point group.

For polarization $E^\omega \parallel c$ / $H^\omega \parallel a$, the difference spectra $\Delta\alpha_H$, $\Delta\alpha_k$ and $\Delta\alpha_P$ in $|H| = 7$ T are shown in Fig. 4.5 (b). Again all three curves are in satisfactorily agreement. For the mode at 71 cm^{-1} $\Delta\alpha$ reaches 25 cm^{-1}. For the mode located at 119 cm^{-1} $\Delta\alpha$ is in the range of 30 to 60 cm^{-1}, however, the exact determination of $\Delta\alpha$ is limited by experimental noise. The strongest directional dichroism is detected for the mode at 85 cm^{-1}, where $\Delta\alpha$ at 7 T clearly exceeds 100 cm^{-1}. As the peak maximum for this mode is not fully resolved, $\Delta\alpha$ can only be estimated. For this purpose the flanks of $\Delta\alpha_H$ were fitted, assuming a Lorentzian lineshape. As shown in Fig. 4.5 (c), this yields a large $\Delta\alpha$ of approximately 200 cm^{-1}.

4.2. THz spectroscopy on $Fe_{2-x}Zn_xMo_3O_8$

4.2.1. Magnons and electromagnetic resonances in $Fe_2Mo_3O_8$

Like in $Co_2Mo_3O_8$, spin excitations of the sister compound $Fe_2Mo_3O_8$ were studied by THz-transmission measurements. Magnetic field dependent absorption spectra, measured at 2 K in $\boldsymbol{H} \parallel c$ are shown in Fig. 4.6 for the three different polarizations (a) $E^\omega \parallel a$ / $H^\omega \parallel b$, (b) $E^\omega \parallel a$ / $H^\omega \parallel c$ and (c) $E^\omega \parallel c$ / $H^\omega \parallel a$. The overall increase of the absorption on the high-frequency side of the spectra obtained for the $E^\omega \parallel a$ configurations originates from a phonon mode located at 129 cm^{-1}, as will be discussed in detail in section 5.1.

In zero magnetic field, below $T_N = 60$ K several low-energy excitations emerge in the antiferromagnetically ordered phase. For $E^\omega \parallel a$ / $H^\omega \parallel b$, three modes are observed at 41, 89 and 113 cm^{-1}. In the *ac*-cut sample the same set of modes is found for polarization $E^\omega \parallel a$ / $H^\omega \parallel c$. For the same polarization direction a further weak excitation at 116 cm^{-1} may appear, though not resolved clearly. In the case of $E^\omega \parallel c$ / $H^\omega \parallel a$, only two modes at 89 and 113 cm^{-1} are observed in zero field.

Table 4.2 summarizes the excitation frequencies in zero magnetic field and the mode activity for the different polarization directions. From this, it can

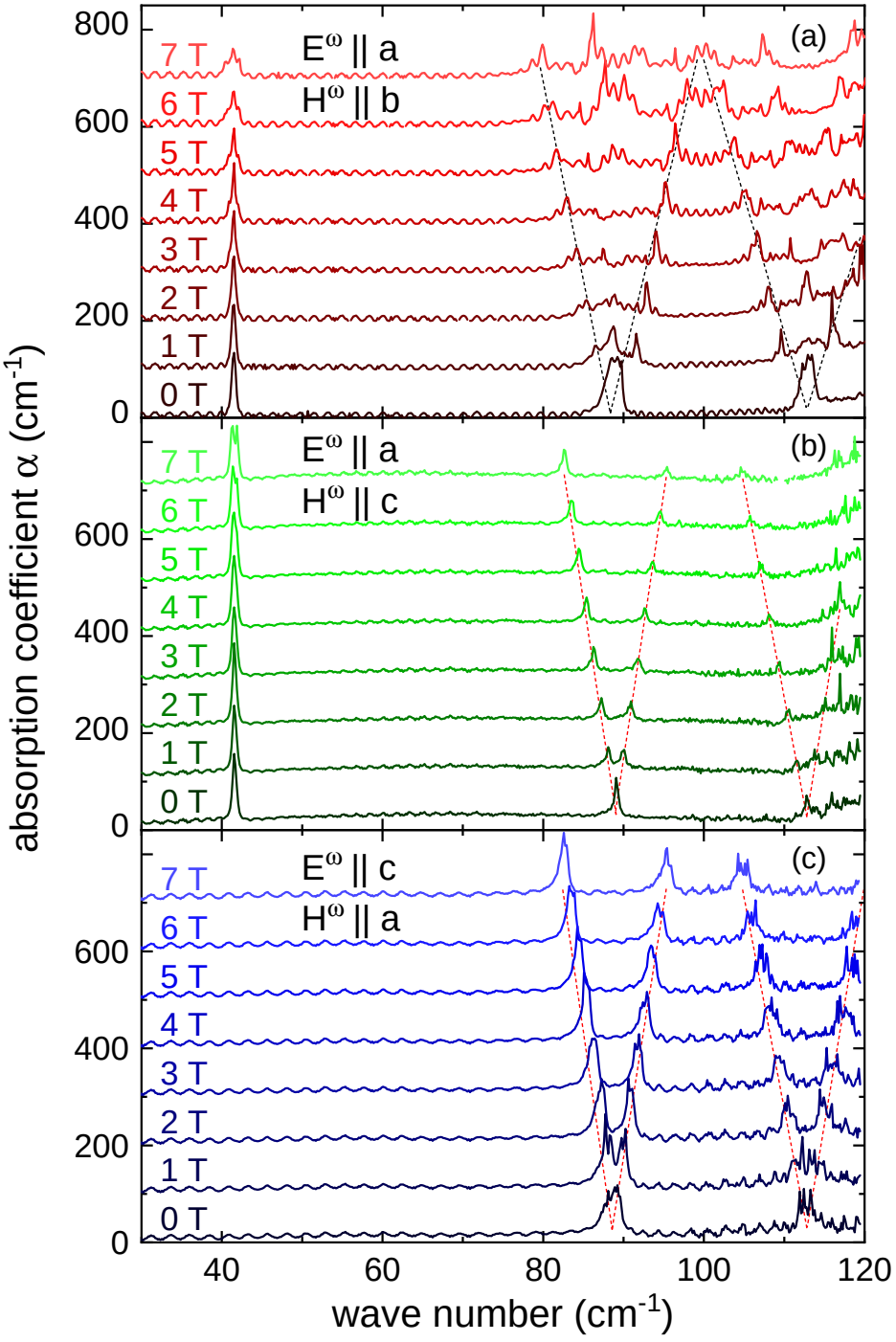

Figure 4.6.: Magnetic field dependence of the absorption spectra of $Fe_2Mo_3O_8$ at $T = 2\,\mathrm{K}$ for polarization (a) $E^\omega \parallel a$ / $H^\omega \parallel b$, (b) $E^\omega \parallel a$ / $H^\omega \parallel c$ and (c) $E^\omega \parallel c$ / $H^\omega \parallel a$. For clarity, the curves are shifted by an offset in proportion to the magnetic field $\boldsymbol{H} \parallel c$. Dashed lines indicate the splitting of the modes in magnetic field.

Table 4.2.: Summary of the mode frequencies of $Fe_2Mo_3O_8$ in zero magnetic field, mode activity for the three different polarizations and corresponding selection rules. The presence or absence of a mode in a certain polarization direction is indicated by ✓ and ×, respectively. (✓)/(×) denotes a mode that could not be unambiguously be identified. When the experimental observation of a mode was not possible due to the low transmission, this is indicated by n.r. (not resolved). Under magnetic field $\boldsymbol{H} \parallel c$ the modes split with the given g-factor.

$H = 0\,\mathrm{T}$					$\boldsymbol{H} \parallel c$
ω_0 (cm^{-1})	$E^\omega \perp c$ $H^\omega \perp c$	$E^\omega \perp c$ $H^\omega \parallel c$	$E^\omega \parallel c$ $H^\omega \perp c$	selection rule	g-factor
41	✓	✓	×	$E^\omega \perp c$	$\gtrsim 0$
89	✓	✓	✓	H^ω, E^ω	2.0 / 3.0
113	✓	✓	✓	H^ω, E^ω	2.3 / 4.0
116	n.r.	(✓)	(×)	?	

be concluded that the mode at $41\,\mathrm{cm}^{-1}$ is purely electric dipole active with E^ω oscillating within the *ab*-plane, which is in line with the observations from Ref. [64], where this mode was ascribed to an electromagnon. The modes at 89 and $113\,\mathrm{cm}^{-1}$ are both magnetic and electric dipole active. In Ref. [64] the mode located at $89\,\mathrm{cm}^{-1}$ was observed, however, there it was found to be only magnetic dipole active. Apparently due to experimental limitations, the mode at $113\,\mathrm{cm}^{-1}$ was not reported there. A previously detected weak mode at $70\,\mathrm{cm}^{-1}$ [167] could not be observed by the THz measurements.

As in $Co_2Mo_3O_8$, also in $Fe_2Mo_3O_8$ more than two excitations are observed in zero magnetic field. In this case, the additional excitations may partly be ascribed to electronic transitions of the tetrahedral Fe^{2+} ions, as suggested by a theoretical study of Prof. Dr. Mikhail Eremin [166], who calculated the splitting of the ${}^5D$ ground term of the tetrahedral Fe^{2+} in $Fe_2Mo_3O_8$. These calculations result in the following energies for the lowest energy levels: 0, 12, 28, 46, 75, 76, 110 and $115\,\mathrm{cm}^{-1}$. Both the purely dipole active excitation at $41\,\mathrm{cm}^{-1}$ and the weak excitation at $116\,\mathrm{cm}^{-1}$ are in excellent agreement with the calculated values. Excitations at 12 and $28\,\mathrm{cm}^{-1}$ were not directly observed by the THz measurements, however, evidence of these energy levels has been found in the finestructure of the *d*-*d* transitions of tetrahedral Fe^{2+}, which have been observed in the IR measurements (see section 5.1). In a previous study the mode at $41\,\mathrm{cm}^{-1}$ has been ascribed to an in-plane oscillating polarization resulting from the precession of the spins via inverse Dzyaloshinskii-Moriya interaction or single-site anisotropy [64]. Furthermore, it is possible that besides the conventional preces-

sional modes also spin-stretching modes become active in $Fe_2Mo_3O_8$, as already discussed for $Co_2Mo_3O_8$.

The magnetic field dependent measurements on $Fe_2Mo_3O_8$ support the easy-axis character of the antiferromagnetic structure, with the c-axis being the easy axis. No splitting of the modes is observed in magnetic fields perpendicular to the c-axis, as exemplarily shown for one polarization direction in Fig. 4.8 (a). In magnetic fields $\boldsymbol{H} \parallel c$ a V-shape splitting of the modes at 89 and 113 cm^{-1} is found, as shown in Fig. 4.6. In the ac-cut sample, as shown in Fig. 4.6 (b)& (c), these splittings are characterized by g-factors of 2.0 and 2.3, respectively. On the ab-cut also an overall V-shape splitting is observed, however, in this case additional peaks occur. Furthermore, considering the outermost frequencies yields higher g-factors of 3.0 and 4.0, respectively. This different behavior of the ab-cut was reproducible on different samples, its reason, however, remains unclear so far. The mode located at 41 cm^{-1} exhibits only a weak magnetic field dependence. The observed broadening of the peak in fields up to 7 T is in line with a weak second order splitting observed in previous high-field measurements [167]. If considering this purely electric dipole active mode as an electronic excitation within the spin-orbit coupling split ground state of the tetrahedral Fe^{2+}, indeed a weak quadratic splitting in magnetic field could be expected [168].

As it can be seen in the phase diagram (Fig. 2.5), with our experimental setup the ferrimagnetic phase can only be reached at temperatures close to T_N. Therefore, the antiferromagnetic-to-ferrimagnetic phase transition and the excitations of the ferrimagnetic phase were studied at 50 K. In Fig. 4.7 the magnetic field dependence of the absorption spectra at 50 K is shown for the two polarizations (a) $E^\omega \parallel a$ / $H^\omega \parallel c$ and (b) $E^\omega \parallel c$ / $H^\omega \parallel a$. Compared to the spectra at 2 K the modes are considerably broadened and their absorption strength is reduced due to the vicinity to T_N. For this reason, the modes at 89 and 113 cm^{-1} are not discernible in the spectra for $E^\omega \parallel a$ / $H^\omega \parallel c$. In the antiferromagnetic phase the field dependence is in agreement with the observations at 2 K, with the mode at 41 cm^{-1} being nearly field independent and the modes at 89 and 113 cm^{-1} splitting with the magnetic field. Above 5 T the ferrimagnetic phase is entered, concomitant with changes in the absorption spectra. For $E^\omega \parallel a$ / $H^\omega \parallel c$ the mode at 41 cm^{-1} is abruptly suppressed in the ferrimagnetic phase. For $E^\omega \parallel c$ / $H^\omega \parallel a$ the 89 cm^{-1} mode is suppressed and a new mode appears in the ferrimagnetic phase at 78 cm^{-1}, which slightly shifts in field. This is in line with the observations reported in Ref. [64]. The mode at 113 cm^{-1} also seems to be suppressed in the ferrimagnetic phase.

In analogy to $Co_2Mo_3O_8$, also in $Fe_2Mo_3O_8$ the directional dichroism resulting from the dynamical magnetoelectric effect was studied. Figure 4.8 (a) shows the field dependent absorption spectra of $Fe_2Mo_3O_8$ for the polarization direction $E^\omega \parallel a$ / $H^\omega \parallel c$ at 2 K in positive and negative magnetic fields $\boldsymbol{H} \parallel a$. Directional dichroism resulting from the time-reversal odd χ'_{zx} is observed for the two both

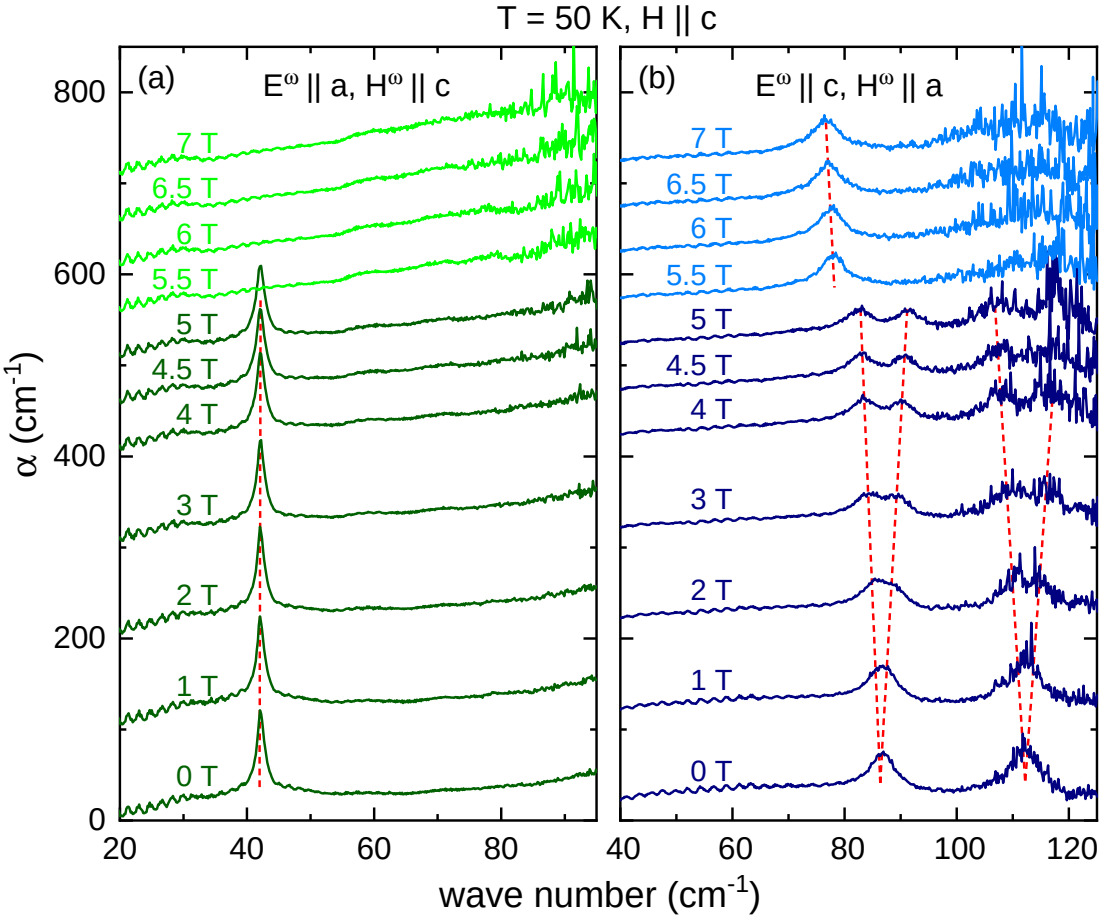

Figure 4.7.: Magnetic field dependence of the absorption spectra of $Fe_2Mo_3O_8$ at $T = 50\,\mathrm{K}$ for polarization direction (a) $E^\omega \parallel a$ / $H^\omega \parallel c$ and (b) $E^\omega \parallel c$ / $H^\omega \parallel a$. Above 5 T the ferrimagnetic phase is entered. For clarity the curves are shifted by an offset in proportion to the magnetic field $\boldsymbol{H} \parallel c$. Dashed lines indicate the mode frequencies.

electric and magnetic dipole active modes at 89 and $113\,\mathrm{cm}^{-1}$. While the absorption strength of the mode at $89\,\mathrm{cm}^{-1}$ is reduced in positive and enhanced in negative magnetic fields, the field dependent behavior of the mode located at $113\,\mathrm{cm}^{-1}$ is opposite.

Again the directional dichroism was studied not only by the reversal of $\boldsymbol{M}$, but also by the reversal of $\boldsymbol{k}$ and $\boldsymbol{P}$. Figure 4.8 (b) shows a comparative plot of the difference spectra $\Delta\alpha_H$, $\Delta\alpha_k$ and $\Delta\alpha_P$, as defined by Eqs. 2.22, at 2 K in $|H| = 7\,\mathrm{T}$. Besides slight differences in the baseline the three curves are in satisfactorily agreement. For both modes a significant directional dichroism with $\Delta\alpha$ in the range of 70–$100\,\mathrm{cm}^{-1}$ is found.

For the perpendicular polarization $E^\omega \parallel c$ / $H^\omega \parallel a$ (not shown) no directional dichroism is observed.

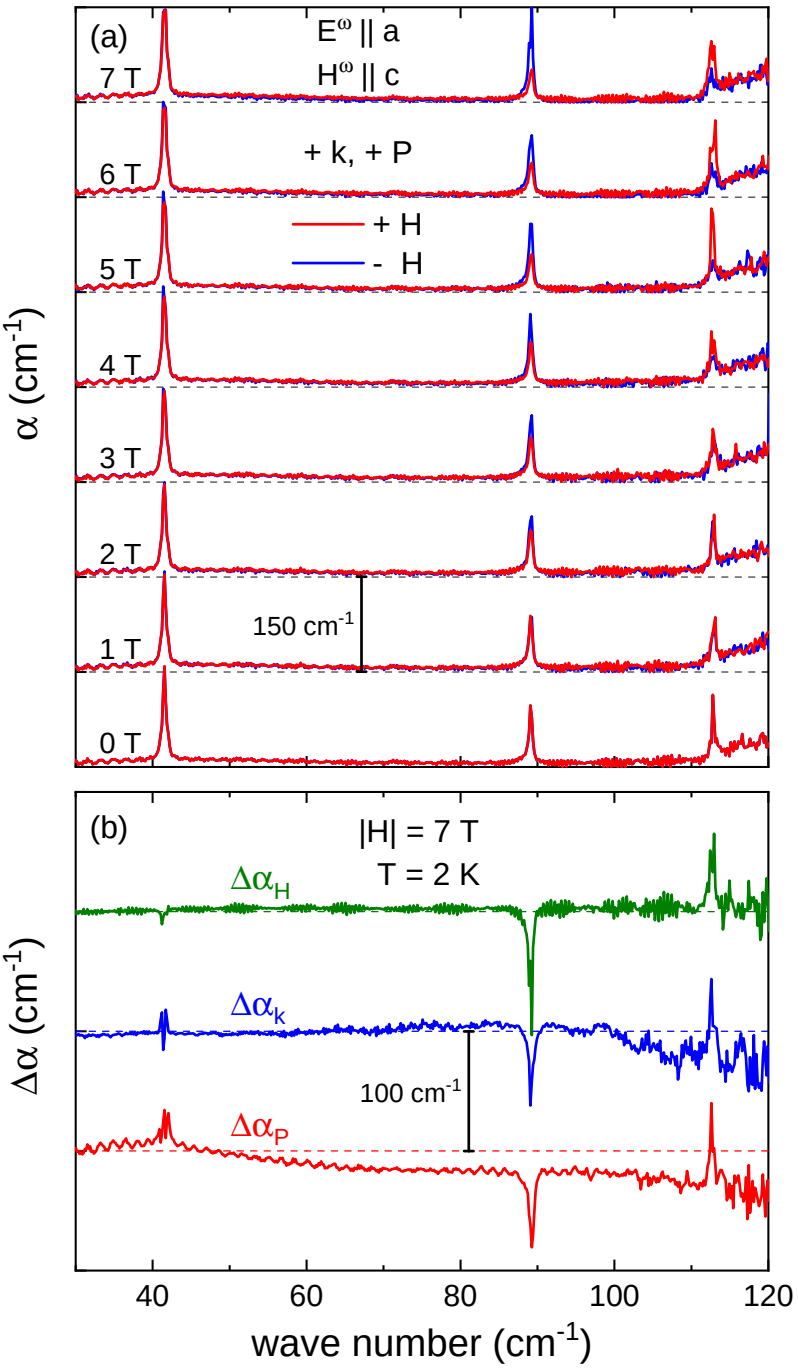

Figure 4.8.: (a) Magnetic field dependence ($\boldsymbol{H} \parallel a$) of the absorption spectra of $Fe_2Mo_3O_8$ for polarization $E^\omega \parallel a$ / $H^\omega \parallel c$ measured at 2 K in $+\boldsymbol{k}$, $+\boldsymbol{P}$ configuration. Red and blue curves represent positive and negative magnetic fields, respectively. (b) Difference spectra $\Delta\alpha_H$, $\Delta\alpha_k$ and $\Delta\alpha_P$ at 2 K in $|H| = 7$ T. The spectra are shifted by a constant offset, as indicated by the dashed lines.

4.2.2. Magnons and vibronic excitation in $Fe_{1.86}Zn_{0.14}Mo_3O_8$

Measurements on $Fe_{1.86}Zn_{0.14}Mo_3O_8$ allow to study the effect of Zn doping on the magnon spectrum and to investigate the observed two-step antiferromagnetic-to-ferrimagnetic phase transition with two critical fields H_{c1} and H_{c2} (see Fig 2.5). The zero-field absorption spectra of $Fe_2Mo_3O_8$ at 2 K are shown in Fig. 4.9 for the three different polarization directions. Again the strong absorption strength of the nearby E_1 phonon limits the measurements of the high-frequency part in the $E^\omega \perp c$ configurations.

Several excitations emerge in the antiferromagnetically ordered phase, as indicated by the triangular symbols. For $E^\omega \perp c$ / $H^\omega \perp c$ four modes are found at 44, 68, 88 and 96 cm^{-1}, as well as a broad asymmetric excitation band with its maximum around 25 cm^{-1}. For $E^\omega \parallel a$ / $H^\omega \parallel c$ only the two excitations at 25 and 44 cm^{-1} are observed , with the peak of the latter being not fully resolved due to low transmission. In the perpendicular polarization $E^\omega \parallel c$ / $H^\omega \parallel a$ four modes at 68, 88 and 114 cm^{-1} are identified.

The mode frequencies are summarized in Tab. 4.3 together with the derived selection rules. The excitations at 25 and 44 cm^{-1} are purely electric dipole active for $E^\omega \perp c$. The modes located at 68 and 88 cm^{-1} are found to be purely magnetic dipole active for $H^\omega \perp c$. For the modes at 96 and 114 cm^{-1} the selection rules can not be unambiguously be determined, however, these modes are presumably at least magnetic dipole active for $H^\omega \perp c$.

The observation of the modes at 44, 88 and 114 cm^{-1} in $Fe_{1.86}Zn_{0.14}Mo_3O_8$ is in agreement with the excitations found in pure $Fe_2Mo_3O_8$ at almost the identical frequencies (see Tab. 4.2). Concerning the large number of modes, clearly exceeding the number of magnetic sublattices of the antiferromagnetic state of $Fe_2Mo_3O_8$, the arguments presented in section 4.2.1 remain valid. Furthermore, the presence of additional modes in $Fe_{1.86}Zn_{0.14}Mo_3O_8$ compared to pure $Fe_2Mo_3O_8$ may indicate an increase of magnetic sublattices due to the partial replacement of the tetrahedral Fe^{2+} by nonmagnetic Zn^{2+}. A systematic Mößbauer study investigating samples with different Zn dopings [44] revealed four different types of octahedral Fe^{2+} sites, depending on how many of their three nearest neighbor tetrahedral Fe^{2+} sites have been substituted by Zn^{2+}.

The most significant feature of the $Fe_{1.86}Zn_{0.14}Mo_3O_8$ spectra is the purely electric dipole active and magnetic-field independent broad asymmetric excitation band around 25 cm^{-1}. Such an excitation so far has neither been observed in pure $Fe_2Mo_3O_8$ nor in any Zn-doped analogue [31,63,64]. Its temperature dependence is shown in Fig. 4.10 (a). Above T_N only the phonon contribution is observed in the spectrum. On lowering the temperature the phonon contribution in this frequency range is reduced due to the sharpening of the E_1 phonon modes (see section 5.1) and the broad excitation evolves in the antiferromagnetic phase together with the modes at 44 and 68 cm^{-1}. The phonon contribution at the lowest temperatures (dashed

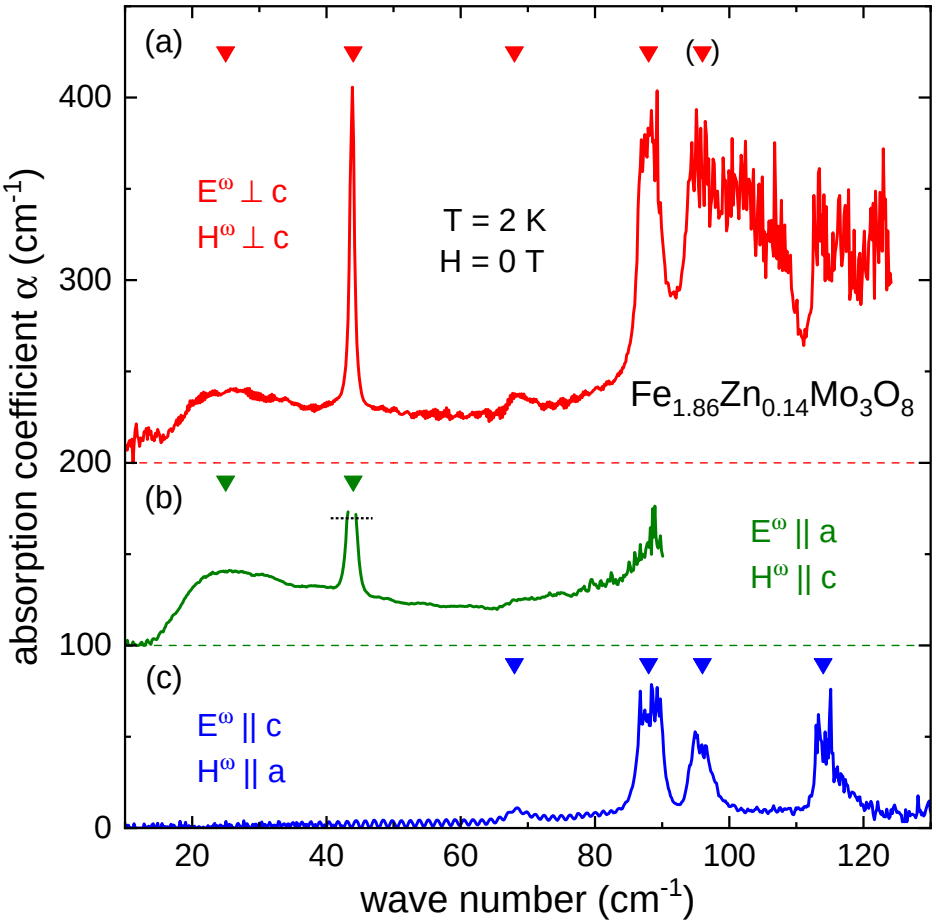

Figure 4.9.: Frequency-dependent absorption coefficient α of $Fe_{1.86}Zn_{0.14}Mo_3O_8$ at $T = 2\,\mathrm{K}$ in zero magnetic field for polarization direction (a) $E^\omega \perp c$ / $H^\omega \perp c$, (b) $E^\omega \parallel a$ / $H^\omega \parallel c$ and (c) $E^\omega \parallel c$ / $H^\omega \parallel a$. For clarity, the curves are shifted by an offset, as illustrated by the dashed horizontal lines. Triangular symbols mark the excitation frequencies.

line in Fig. 4.10 (a)) was obtained from a fit of the FIR reflectivity by an oscillator model (c. f. section 5.1), as illustrated in Fig. 4.10 (b).

The existence of a broad asymmetric excitation band suggests a coupling of electronic and structural or vibrational degrees of freedom in $Fe_{1.86}Zn_{0.14}Mo_3O_8$. The coupling of electronic and vibrational transitions leads to vibronic excitations. Figure 4.10 (c) shows the absorption spectrum of $Fe_{1.86}Zn_{0.14}Mo_3O_8$ at 2 K with subtracted phonon contribution. As illustrated by the red solid line, the broad asymmetric excitation was successfully simulated by Benjamin Csizi with the model of a vibronic excitation, including $n = 1$, 2 and 3 phonon processes and a zero-phonon line, i. e. a purely electronic transition, at $12\,\mathrm{cm}^{-1}$. Details of the simulation are found in Appendix A.1.

Table 4.3.: Summary of the mode frequencies of $Fe_{1.86}Zn_{0.14}Mo_3O_8$ in zero magnetic field, mode activity for the three different polarizations and corresponding selection rules. The presence or absence of a mode in a certain polarization direction is indicated by ✓ and ×, respectively. (✓) denotes a mode that could not be unambiguously be identified. When the experimental observation of a mode was not possible due to the low transmission, this is indicated by n.r. (not resolved). Under magnetic field $\boldsymbol{H} \parallel c$ the modes of the antiferromagnetic phase split with the given g-factor.

$H = 0\,\mathrm{T}$					$\boldsymbol{H} \parallel c$
ω_0 (cm^{-1})	$E^\omega \perp c$ $H^\omega \perp c$	$E^\omega \perp c$ $H^\omega \parallel c$	$E^\omega \parallel c$ $H^\omega \perp c$	selection rule	g-factor
25	✓	✓	×	$E^\omega \perp c$	
44	✓	✓	×	$E^\omega \perp c$	
68	✓	×	✓	$H^\omega \perp c$	4.0
88	✓	×	✓	$H^\omega \perp c$	2.0
96	(✓)	n.r.	✓	?	2.6
114	n.r.	n.r.	✓	?	2.5

The zero-phonon line at $12\,\mathrm{cm}^{-1}$ is not directly observed in the absorption spectrum, however, its energy is in agreement with the splitting of the lowest-lying d-levels of the tetrahedral Fe^{2+} in $Fe_2Mo_3O_8$, as determined from theoretical calculations [44, 166] and from IR spectroscopy [section 5.1], [60]. These findings support the assignment of the broad excitation band to a vibronic excitation related to the lowest electronic transition of tetrahedral Fe^{2+}.

To study the excitations of the ferrimagnetic phase and the two-step antiferromagnetic-to-ferrimagnetic transition, magnetic field dependent measurements with $\boldsymbol{H} \parallel c$ were performed at 13 K, where both magnetic phases are accessible with the 7 T experimental setup. Magnetic field dependent absorption spectra are exemplarily shown for polarization $E^\omega \parallel c$ / $H^\omega \parallel a$ in Fig. 4.11 (a). In the antiferromagnetic phase a V-shape splitting of the modes is observed, which can be described by the g-factors summarized in Tab. 4.3. The g-factors of the intrinsic modes of pure $Fe_2Mo_3O_8$ (44, 88, $114\,\mathrm{cm}^{-1}$) are in agreement with the values in Tab. 4.2. The modes of the antiferromagnetic phase are suppressed in the ferrimagnetic state, where new modes evolve, which show a approximately linear field dependence. Interestingly, for magnetic fields $H_{c1} < H < H_{c2}$ the modes of both the antiferromagnetic and the ferrimagnetic phase can be observed simultaneously. This finding implies a coexistence of the two magnetic phases in the intermediate field region $H_{c1} < H < H_{c2}$.

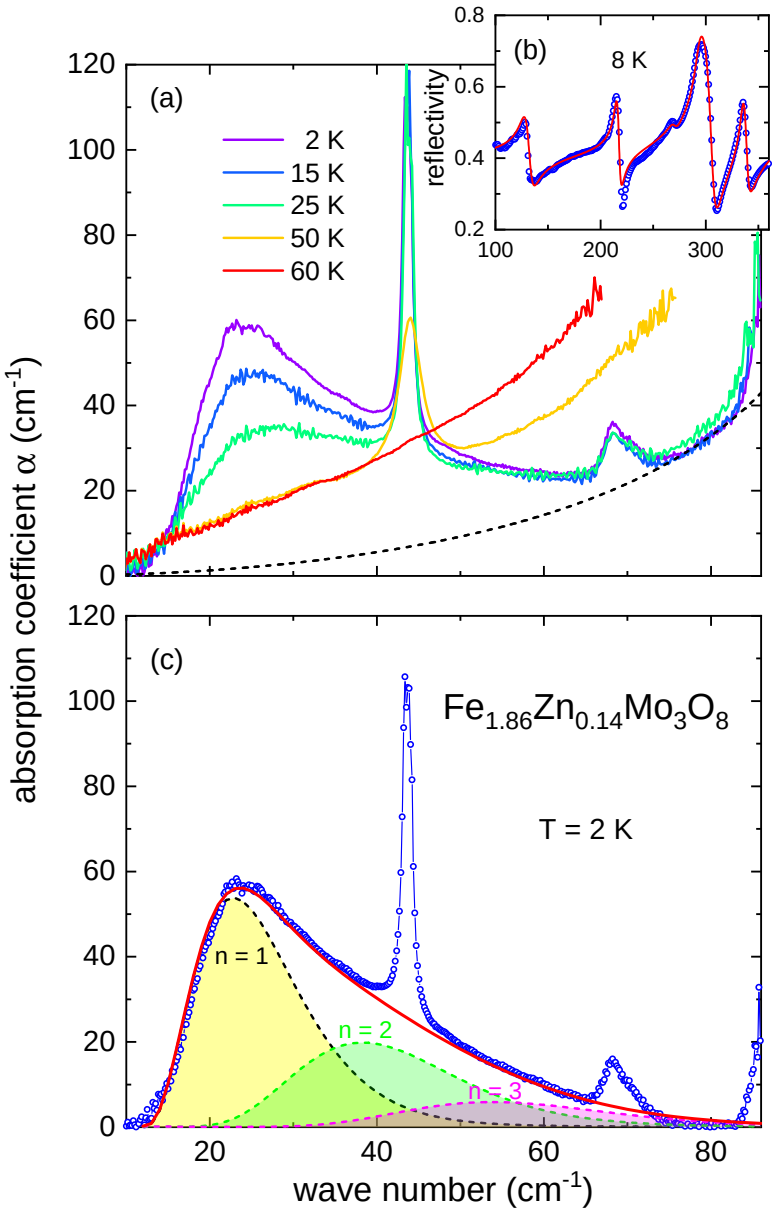

Figure 4.10.: (a) Temperature dependence of the broad asymmetric excitation band in $Fe_{1.86}Zn_{0.14}Mo_3O_8$ for polarization $E^\omega \perp c$ / $H^\omega \perp c$. The dashed line accounts for the phonon contribution, as derived from a fit of the phonon reflectivity spectrum (b). (c) Absorption spectrum at 2 K with subtracted phonon contribution. The red solid line represents the simulation of the spectrum with the model of a vibronic excitation, as described in the text. Shaded areas illustrate its deconvolution into $n = 1$, 2 and 3 phonon processes.

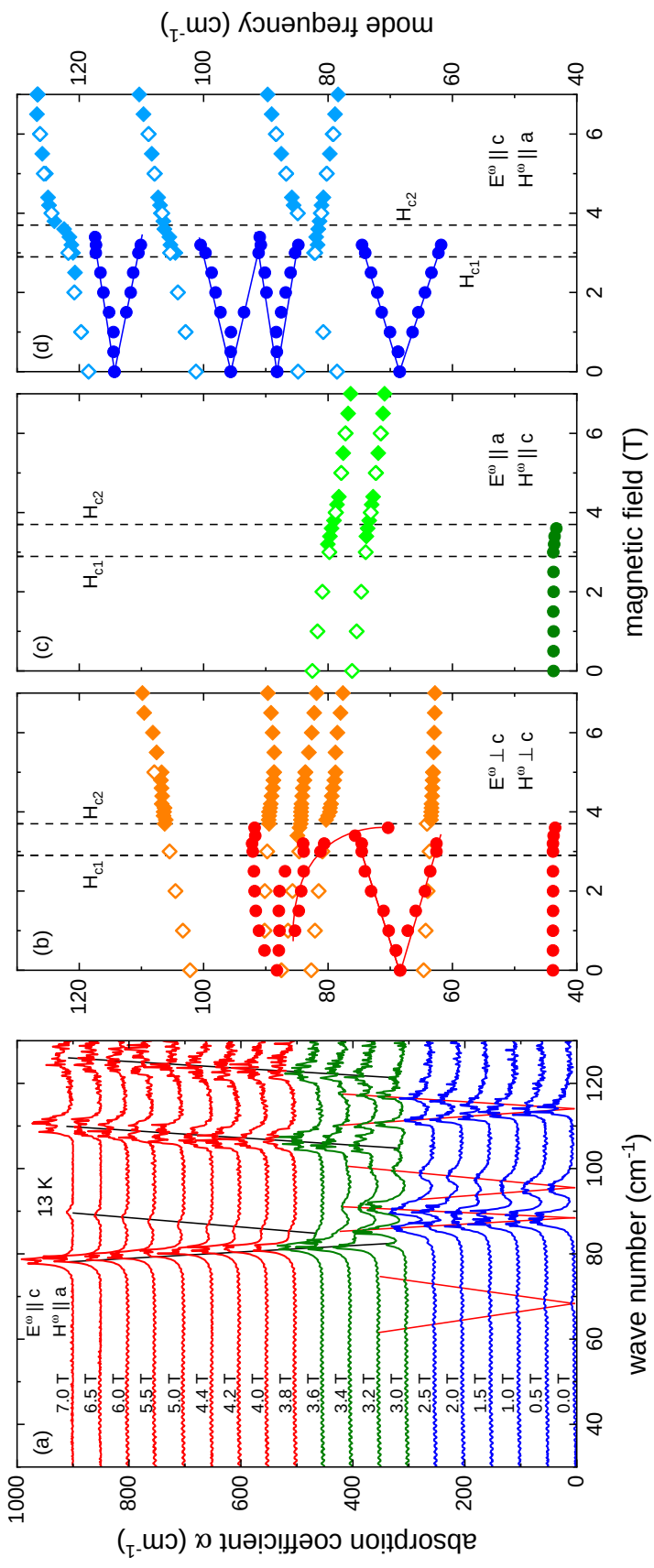

Figure 4.11.: (a) Field dependence of the absorption spectra of $Fe_{1.86}Zn_{0.14}Mo_3O_8$ at 13 K for polarization $E^\omega \parallel c$ / $H^\omega \parallel a$ in $\boldsymbol{H} \parallel c$. Blue and red curves represent the spectra of the antiferromagnetic and the ferrimagnetic phase, respectively. Green spectra are measured in the intermediate phase $H_{c1} < H < H_{c2}$. Red and black solid lines trace the mode frequencies in the antiferromagnetic and ferrimagnetic phase, respectively. (b)-(d) Mode frequencies obtained from THz transmission measurements in the three different polarization directions at 13 K as a function of magnetic field $\boldsymbol{H} \parallel c$. Dark colored circles indicate modes of the antiferromagnetic phase. Light colored diamonds represent modes of the ferrimagnetic phase. Mode frequencies in decreasing fields are shown as open symbols. Dashed vertical lines indicate the critical magnetic fields H_{c1} and H_{c2}.

The field dependence of the mode frequencies for all polarization directions is shown in Fig. 4.11 (b)-(d), which in addition also includes the eigenfrequencies of the ferrimagnetic modes in decreasing magnetic fields, demonstrating the hysteretic behavior. Unlike in the antiferromagnetic phase, it is not straightforward to relate the ferrimagnetic modes observed for the different polarizations to each other or to derive selection rules. On one hand, demagnetization effects on the different samples may influence the mode frequencies. On the other hand, the latest measurements on an *ab*-cut sample, which would be expected to be isotropic, revealed a polarization direction dependence of the eigenfrequencies in the ferrimagnetic phase, which allows to shift the modes by more than $20\,\mathrm{cm}^{-1}$. The origin of this unexpected behavior remains unclear so far.

As in $Co_2Mo_3O_8$ and pure $Fe_2Mo_3O_8$, also in the Zn doped $Fe_{1.86}Zn_{0.14}Mo_3O_8$ the magnetic point group symmetry would allow directional dichroism in the antiferromagnetic phase for magnetic fields applied perpendicular to the *c*-axis. Although directional dichroism was found for some modes in pure $Fe_2Mo_3O_8$ (see section 4.2.1), it was not observed in $Fe_{1.86}Zn_{0.14}Mo_3O_8$.

Summarizing the results from THz spectroscopy on the transition metal Mo oxides $Co_2Mo_3O_8$, $Fe_2Mo_3O_8$ and $Fe_{1.86}Zn_{0.14}Mo_3O_8$, in all three compounds the magnon spectra are more complex than expected for the reported four-sublattice collinear easy-axis antiferromagnetic structure. As a rule of thumb, linear spin-wave theory predicts the number of precessional magnon modes to be equal to the number of magnetic sublattices. However, in each case more modes are observed. As, nevertheless, the field-dependent optical data as well as INS measurements support the easy-axis nature of the magnetically ordered phase, the possibility of transitions with $\Delta S > 1$, spin-stretching modes and low-lying electronic excitations was discussed. Polarization-dependent measurements reveal the selection rules of the modes. Beyond the conventional magnons, electromagnons and magnetoelectric resonances are found in the $M_2Mo_3O_8$ compounds.

Strong directional dichroism has been observed in $Co_2Mo_3O_8$ and $Fe_2Mo_3O_8$, impressively demonstrating the dynamical magnetoelectric effect. The trilinear product $\boldsymbol{k} \cdot (\boldsymbol{P} \times \boldsymbol{M})$ is a measure of the magnetoelectric directional anisotropy. By independent switching of $\boldsymbol{k}$, $\boldsymbol{P}$ and $\boldsymbol{M}$, all three possibilities of switching the sign of $\boldsymbol{k} \cdot (\boldsymbol{P} \times \boldsymbol{M})$ and, thus, realizing directional dichroism, have been proven experimentally for the first time within the course of this work.

5. Tracing symmetry lowering by phonon excitations

In the following chapter the results obtained from phonon spectroscopy on $Fe_2Mo_3O_8$ and on lacunar spinels AM_4X_8 will be presented. As phonons are directly related to the crystal symmetry, their investigation allows to trace a possible symmetry lowering. The infrared study of $Fe_2Mo_3O_8$ reveals an unusual temperature dependence of the E_1 modes, which is ascribed to the coupling of the phonons to orbital degrees of freedom. Systematic investigation of the phonons over a broad series of lacunar spinels allows to assign the modes to individual structural units. The results of my work presented in section 5.1 have been published in Ref. [59], results discussed in section 5.2 have been published in Ref. [169].

5.1. Lattice dynamics and orbital degrees of freedom in $Fe_2Mo_3O_8$

5.1.1. Diffraction studies

As discussed in section 2.4, at room temperature $Fe_2Mo_3O_8$ exhibits a hexagonal structure with polar space group $P6_3mc$. As the magnetic phase transition at $T_N = 60\,K$ happens concomitant with a significant increase of the ferroelectric polarization and therefore is associated with ionic shifts [7], the question arises, whether the high-temperature symmetry is preserved below T_N. On the basis of infrared and Raman measurements the authors of Ref. [60] recently claimed a symmetry lowering in $Fe_2Mo_3O_8$, as additional excitations were observed below T_N, which were ascribed to phonon modes. However, a direct measurement of the low-temperature structure had not been reported.

To clarify the low-temperature symmetry, high-resolution x-ray and neutron diffraction experiments in the temperature range from 1.7 to 300 K were recently performed by Dr. Alexander Tsirlin and Dr. Nazir Khan. Exemplary diffraction patterns are included in Appendix A.2. The x-ray data show no changes when crossing T_N. Increased intensities in the neutron data below T_N are purely ascribed to magnetic scattering. The neutron diffraction data at 1.7 K could be refined with the $P6_3mc$ symmetry and the reported collinear antiferromagnetic structure. Thus, these data clearly exclude a symmetry lowering below T_N. In agreement

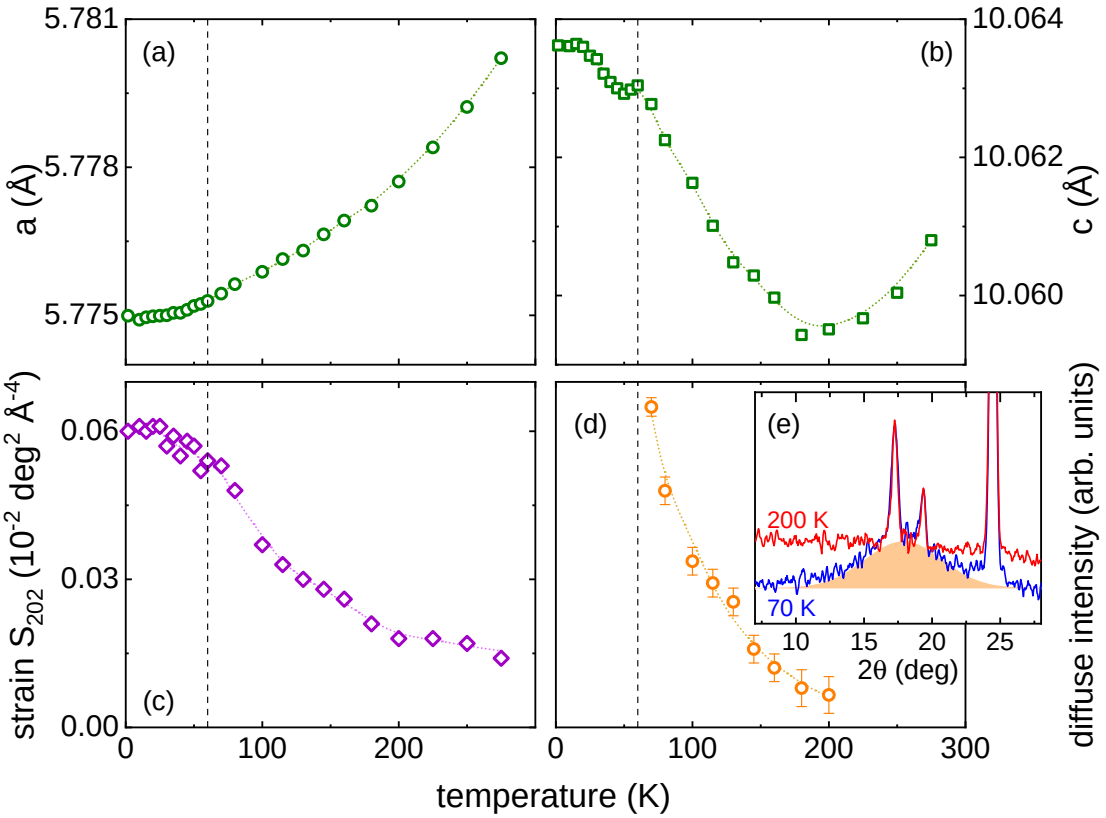

Figure 5.1.: (a), (b) Temperature-dependent in-plane lattice parameter a and out-of-plane lattice parameter c. (c) Temperature dependence of the strain parameter S_{202} and (d) the magnetic diffuse scattering intensity, as determined from the broad diffuse feature (shaded area in frame (e)) appearing in the neutron diffraction data below 200 K. Dashed vertical lines indicate the phase transition temperature $T_N = 60$ K.

with the previously reported study [45], the refined ordered moment of 4.61 μ_B exceeds the spin-only value of 4 μ_B and indicates significant orbital contributions to the magnetic moment.

From the neutron diffraction measurements the temperature dependence of the lattice parameters a and c has been determined, which is shown in Fig. 5.1 (a) and (b), respectively. As expected, the in-plane lattice parameter a monotonically increases with temperature due to thermal expansion. The temperature dependence of the out-of-plane lattice parameter c, however, is rather unusual. Starting at room temperature, c initially decreases upon cooling, but it exhibits an anomalous minimum around 200 K an then increases towards the lowest temperatures with a slight kink at T_N. As no spectroscopic evidence of this anomalous behavior of the lattice parameter c had been reported previously, these findings were a key motivation for the performed IR study on $Fe_2Mo_3O_8$.

As shown in Fig. 5.1 (c), the anomaly of the lattice parameter c is also reflected in the temperature dependence of the strain parameter S_{202}, which represents the anisotropic strain contribution to the reflection width (c. f. Appendix A.2). While nearly constant for the highest temperatures, at 200 K S_{202} starts to increase with decreasing temperature and gets saturated below T_N.

Furthermore, below 200 K a broad feature develops in the neutron diffraction data, as indicated by the shaded area in Fig. 5.1 (e). This feature, gaining most intensity in the magnetically ordered phase, is ascribed to magnetic diffuse scattering. The temperature dependence of the magnetic diffuse scattering intensity is shown in Fig. 5.1 (d). Appearing below 200 K, it continuously increases on lowering the temperature towards T_N.

From these findings it can be concluded that in $Fe_2Mo_3O_8$ below 200 K short-range magnetic ordering sets in. The onset of magnetic order can be connected with a lattice expansion, if this stabilizes the ordered state and optimizes the exchange energy [170]. Therefore, the short-range ordering in $Fe_2Mo_3O_8$ can be reflected in the strain parameter S_{202} and in the anomalous minimum of the lattice parameter c. Like the onset of long-range antiferromagnetic order at T_N, also the short-range ordering below 200 K is found to take place without any symmetry lowering.

5.1.2. Optical spectroscopy studies

Motivated by the x-ray and neutron diffraction study, infrared reflectivity measurements on $Fe_2Mo_3O_8$ were carried out in the frequency range from 100 to 8000 cm^{-1} for temperatures between 5 and 300 K. Figure 5.2 shows the IR reflectivity spectra for the two polarizations $E^\omega \perp c$ and $E^\omega \parallel c$ at 5 and 100 K, i. e. for one temperature above and one temperature below the antiferromagnetic ordering temperature of $T_N = 60$ K. In the FIR range up to 800 cm^{-1} several pronounced excitations are found, which are primarily identified as phonon modes. Around 3500 cm^{-1} several weaker excitations are observed. These are ascribed to the *d-d* transitions of the tetrahedrally coordinated Fe^{2+} ions, which are typically located in this frequency range [171–177]. While they show up as sharp features in the 5 K reflectivity, they get considerably broadened above T_N. The *d-d* transitions of the octahedral Fe^{2+} are usually found at higher energies [178, 179], which are not covered by the performed measurements.

In the following, the temperature dependence of the FIR excitations as well as the *d-d* transitions of $Fe_2Mo_3O_8$ will be analyzed in detail. The FIR reflectivity spectra of $Fe_2Mo_3O_8$ for the two polarizations $E^\omega \perp c$ and $E^\omega \parallel c$ are shown in Fig. 5.3 for selected temperatures. The spectra obtained in the course of this work are in agreement with previously reported data [60]. On the basis of these spectra, the FIR excitations can be classified into three different types, depending on the temperature ranges within which they occur:

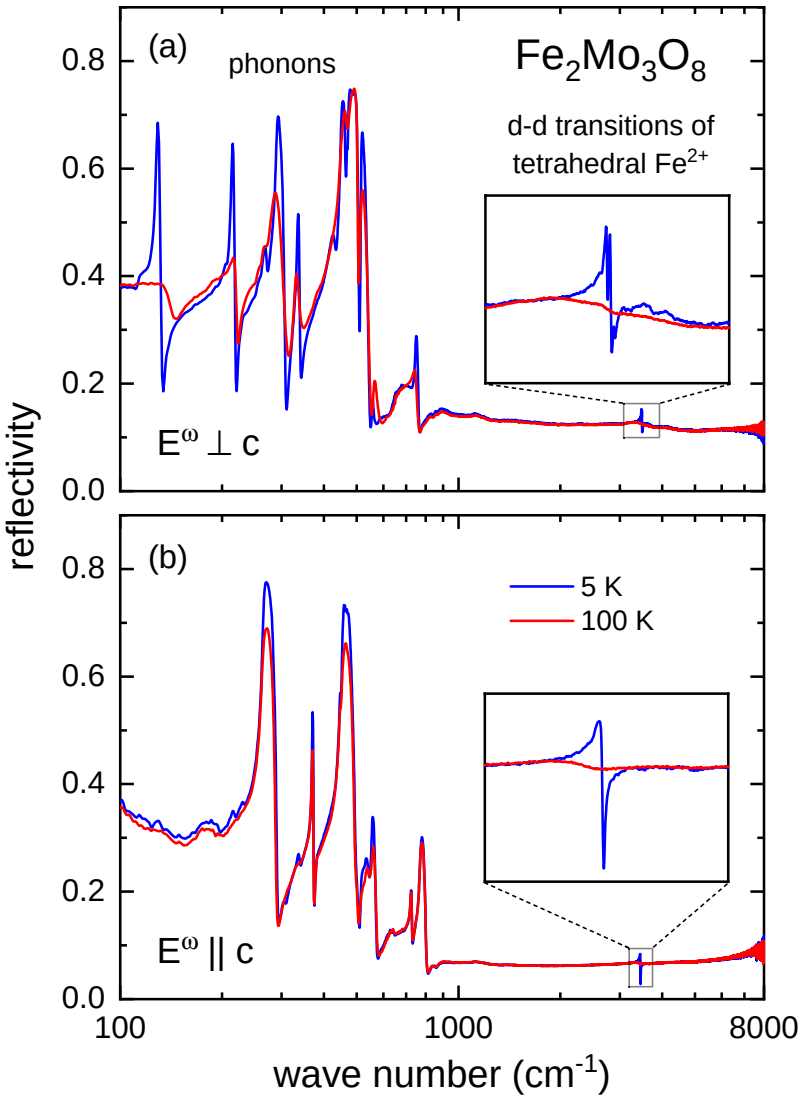

Figure 5.2.: Semilogarithmic plot of the frequency-dependent reflectivity spectra of $Fe_2Mo_3O_8$ measured at 5 K (blue curves) and 100 K (red curves) for polarization (a) $E^\omega \perp c$ and (b) $E^\omega \parallel c$ [59]. Phonons dominate the reflectivity spectra below 800 cm^{-1}. The *d-d* transitions of the tetrahedral Fe^{2+} ions are observed around 3500 cm^{-1}. The insets show zoom-ins of the *d-d* transitions.

1. Excitations, which are already present at room temperature. These are mainly phonons, but also weak excitations of presumably electronic origin (see Fig. 5.3 (d)).

2. A broad feature in the frequency range between 600 and 700 cm^{-1}, which emerges for $E^\omega \perp c$ below 200 K (see Fig. 5.3 (c)) and therefore my be related to the short-range ordering.

3. Excitations appearing only below T_N, as indicated by the arrows in Fig. 5.3.

FIR excitations visible at room temperature

The FIR spectra, as shown in Fig. 5.3, are clearly dominated by the phonon modes. Group theory allows to directly determine the number of phonon modes on the basis of the crystal symmetry and the occupied Wyckoff positions. As discussed above, over the whole investigated temperature range $Fe_2Mo_3O_8$ exhibits the space group symmetry $P6_3mc$. With the Wyckoff positions from Ref. [45] the symmetry analysis results in the following phonon modes:

$$\begin{aligned} \Gamma = {} & 9A_1 + 12E_1 && \text{(Raman- and IR active)} \\ & + 13E_2 && \text{(Raman-active)} \\ & + A_1 + E_1 && \text{(acoustic)} \\ & + 3A_2 + 10B_1 + 3B_2 && \text{(silent).} \end{aligned} \tag{5.1}$$

Out of these, $9A_1$ and $12E_1$ modes are the zone-center IR active phonons, with the nine one-dimensional A_1 modes being active for $E^\omega \parallel c$ and the $12E_1$ modes being active for $E^\omega \perp c$.

Figure 5.4 shows the FIR optical conductivity σ at 5 K for the two polarization directions $E^\omega \perp c$ and $E^\omega \parallel c$, which has been determined from the broadband reflectivity spectra by Kramers-Kronig transformation using a ω^{-1} high-frequency extrapolation followed by a ω^{-4} extrapolation above $8 \cdot 10^5\,\mathrm{cm}^{-1}$. In the case of $E^\omega \parallel c$ the reflectivity data only above $150\,\mathrm{cm}^{-1}$ have been used.

The phonon modes show up as well pronounced peaks in the optical conductivity spectra. At room temperature nine of the twelve E_1 modes are observed for $E^\omega \perp c$. For the perpendicular polarization $E^\omega \parallel c$, eight out of the nine allowed IR active are identified. It should be noted that the weak features observed for $E^\omega \parallel c$ around 215, 305, 335 and $520\,\mathrm{cm}^{-1}$ (green triangles in Fig. 5.4 (b)) originate from a slight polarization leakage from the $E^\omega \perp c$ direction and are no intrinsic excitations of the $E^\omega \parallel c$ direction.

The experimental phonon eigenfrequencies of $Fe_2Mo_3O_8$ can directly be compared to those obtained from DFT+U+SO calculations, which were performed by Dr. Alexander Tsirlin. For the calculations the antiferromagnetic spin structure was imposed. The calculated phonon frequencies, as indicated by the blue triangles in Fig. 5.4, are in excellent agreement with the experimental values for $E^\omega \parallel c$. Only for the calculated A_1 mode at $201\,\mathrm{cm}^{-1}$ no direct counterpart is identified experimentally. Note that the feature observed around $190\,\mathrm{cm}^{-1}$ for $E^\omega \parallel c$ (better seen Fig. 5.3 (b)) is an experimental artefact stemming from the cryostat windows. However, also in Ref. [60] no further A_1 mode was found at this frequency. For polarization $E^\omega \perp c$ the calculated phonon frequencies are also in reasonable agreement with the experimental ones, however, in this case the deviations are slightly larger than for $E^\omega \parallel c$. For both polarizations all experimental FIR excitation frequencies determined from the optical conductivity at 70 K and 5 K are

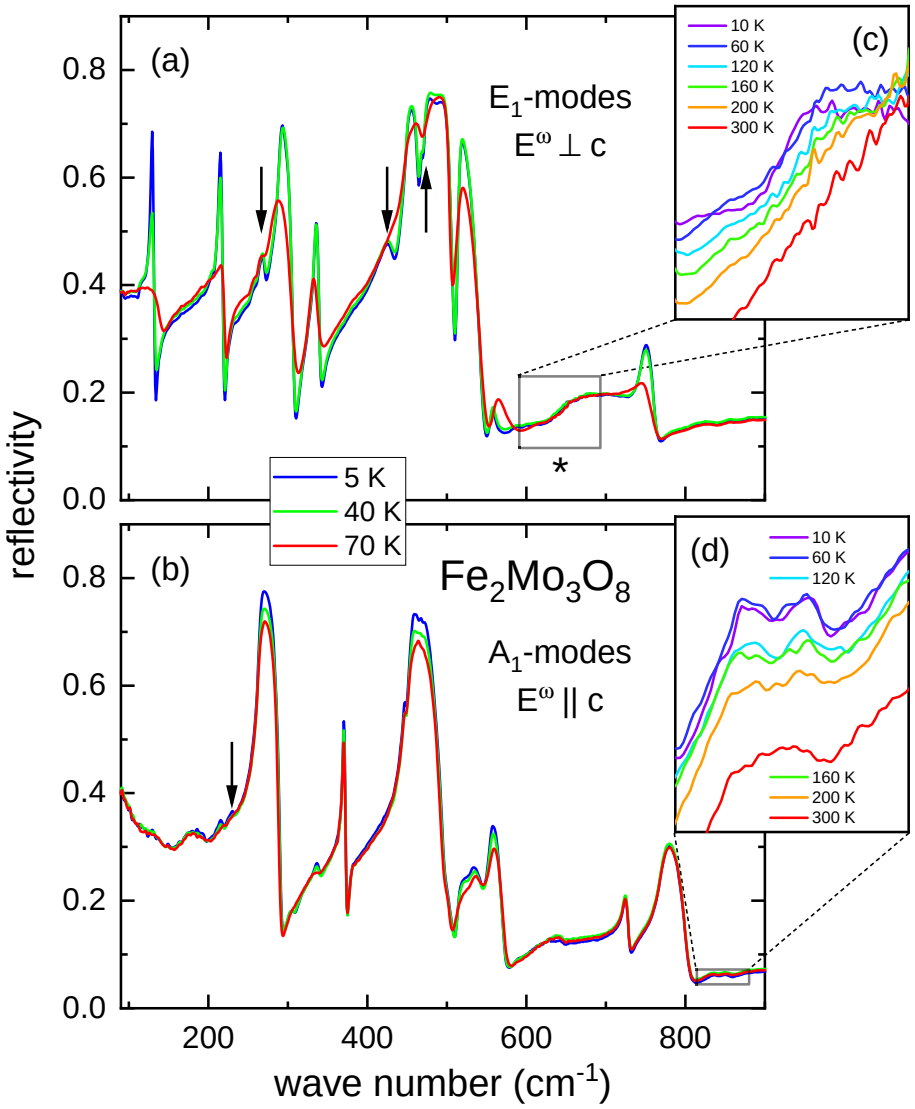

Figure 5.3.: Frequency-dependent FIR reflectivity spectra of $Fe_2Mo_3O_8$ for polarization (a) $E^\omega \perp c$ and (b) $E^\omega \parallel c$ at three selected temperatures [59]. Additional modes appearing below T_N are marked by arrows. The asterisk $*$ indicates the broad spectral feature appearing below 200 K. Its temperature dependence is shown in frame (c). (d) Temperature dependence of weak excitations around 850 cm^{-1}.

summarized in Tab. 5.1 together with the calculated values. A full list with all calculated phonon modes is found in Appendix A.3.

As shown in Fig. 5.4 (c) and (d), in addition to the phonon modes, further weak excitations are observed in the FIR spectra for both polarization directions around 850 cm^{-1}, which are already present at room temperature. In a previous IR study of $Fe_2Mo_3O_8$ [60] the authors ascribed these spectral features to an additional A_1 phonon mode, eventually promoting their claim of symmetry

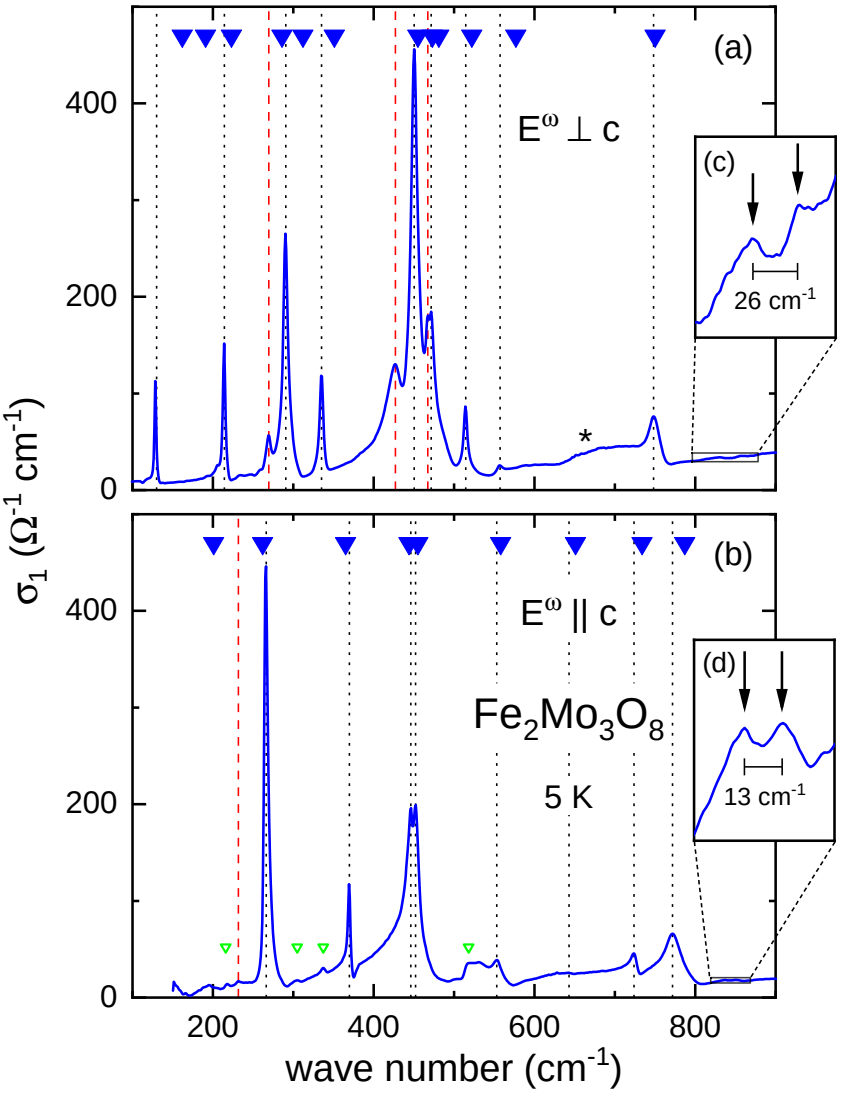

Figure 5.4.: Frequency-dependent optical conductivity σ of $Fe_2Mo_3O_8$ at 5 K for polarization (a) $E^\omega \perp c$ and (b) $E^\omega \parallel c$ [59]. Dotted black lines indicate the phonon eigenfrequencies, as determined from the peak maxima of σ. Modes appearing below T_N are marked by dashed red lines. Blue triangles indicate the phonon frequencies obtained from DFT+U calculations. Features in the $E^\omega \parallel c$ spectrum, which are marked by green triangles, stem from polarization leakage from the $E^\omega \perp c$ direction. The asterisk $*$ indicates the broad spectral feature appearing below 200 K. The insets show zoom-ins of the weak excitations observed at (c) 830 and 856 cm^{-1} for $E^\omega \perp c$ and (d) 837 and 850 cm^{-1} for $E^\omega \parallel c$.

Table 5.1.: Summary of the FIR excitation frequencies (in cm^{-1}) of $Fe_2Mo_3O_8$ at 70 K and at 5 K for the two polarizations $E^\omega \perp c$ and $E^\omega \parallel c$. Upper part: Eigenfrequencies of the excitations already visible at room temperature and phonon frequencies from DFT+U+SO. Middle part: Excitations emerging concomitantly with the short-range ordering below 200 K. Lower part: Additional excitations appearing only below T_N.

	$E^\omega \perp c$		E_1	$E^\omega \parallel c$		A_1
	70 K	5 K	DFT+U	70 K	5 K	DFT+U
$T > 200$ K	135	129	162			201
			191	269	269	262
	218	214	223	371	371	365
			286	447	446	444
	290	292	312	458	457	454
	333	335	351	558	556	558
	454	452	455	643	643	651
			473	727	727	734
	473	471	481	782	782	787
	510	514	522			
	561	559	577			
	751	754	750			
	836	837		831	830	
	850	850		857	856	
$T \leq 200$ K	613	596				
	697	692				
$T \leq T_N$		270			230	
		426				
		468				

lowering. However, on the basis of our data, the classification of these excitations as a phonon mode seems unlikely. From the DFT calculations no phonon modes are expected in this frequency range. Besides, when following the temperature dependence of these excitations, as exemplarily shown for $E^\omega \parallel c$ in Fig. 5.3 (d), a two-peak structure develops below 200 K with the onset of short-range magnetic ordering. At the lowest temperatures these excitations are located at 837 and 850 cm^{-1} for $E^\omega \perp c$ and at 830 and 856 cm^{-1} for $E^\omega \parallel c$, i. e. with frequency spacings of 26 and 13 cm^{-1}, respectively. As it will be discussed later, exactly the same frequency spacings are observed in the *d-d* transitions of the tetrahedral Fe^{2+}

sites. These findings suggest that the weak excitations located around 850 cm^{-1} have electronic origin.

In a next step, a closer look shall be taken at the temperature dependence of the phonon modes. Already at a first glance it becomes apparent from the reflectivity spectra shown in Fig. 5.3 that the temperature dependent behavior of the A_1 and E_1 modes is different. While the A_1 modes exhibit only a minor temperature dependence between 70 and 5 K, the E_1 modes are considerably narrowed below T_N. For a detailed analysis of their temperature dependence, the FIR reflectivity spectra of $Fe_2Mo_3O_8$ were fitted with a model consisting of a sum of Fano and Lorentz oscillators, as implemented in the RefFIT program [180, 181]. Its complex dielectric permittivity is given by:

$$\epsilon = \epsilon_\infty + \sum_n \frac{\omega_{p,n}^2}{\omega_{0,n}^2 - \omega^2 - i\gamma_n\omega} \left(1 + i\frac{\omega_{q,n}}{\omega}\right)^2 + \left(\frac{\omega_{p,n}\omega_{q,n}}{\omega_{0,n}\omega}\right)^2 \tag{5.2}$$

Here ω_0 and γ denote the eigenfrequency and the damping of the respective oscillator. The damping is directly related to the inverse phonon lifetime $\gamma = 1/\tau$. The plasma frequency ω_p accounts for the oscillator strength. Asymmetric line shapes are considered by the Fano parameter ω_q. The symmetric Lorentzian lineshape, which is the standard model for phonons, is obtained for $\omega_q = 0$. The high-frequency dielectric constant is denoted as ϵ_∞.

For the fitting of the $E^\omega \perp c$ spectra, starting at room temperature, nine oscillators corresponding to the observed phonons were used. Below 200 K two additional Lorentz oscillators were included to account for the broad spectral feature ($*$) developing with the onset of short-range ordering in the frequency range between 600 and 700 cm^{-1}. For the excitations appearing only below T_N, additional oscillators were included, except for the one at 468 cm^{-1}, which is too weak to be properly fitted (see Fig. 5.5 (a)). For polarization $E^\omega \parallel c$ the phonon spectra were fitted with seven oscillators. The weak mode located at 447 cm^{-1} as well as the mode at 230 cm^{-1}, which appears below T_N, were not included into the fitting procedure, as these are close to the resolution limit. To improve the fit quality for $E^\omega \parallel c$, the polarization leakage features were modelled by additional oscillators. As far as possible, pure Lorentzian oscillators were used ($\omega_q = 0$) for the fitting process. To account for their asymmetric lineshapes and to improve the fitting, Fano oscillators have only been used for the four lowest-lying modes for $E^\omega \perp c$, and for the two modes at 269 and 458 cm^{-1} for $E^\omega \parallel c$. The asymmetric Fano lineshape generally describes the coupling to a background continuum. As at present it remains unclear if this is the case in $Fe_2Mo_3O_8$, the use of the Fano oscillator might be regarded as a parameterization. Fits of the reflectivity spectra at 5 K for both polarization directions are shown in Fig. 5.5. The fits are in satisfactorily agreement with the experimental data. Solely the increase of the reflectivity towards the lowest frequencies for $E^\omega \parallel c$ is not covered by the fit. The

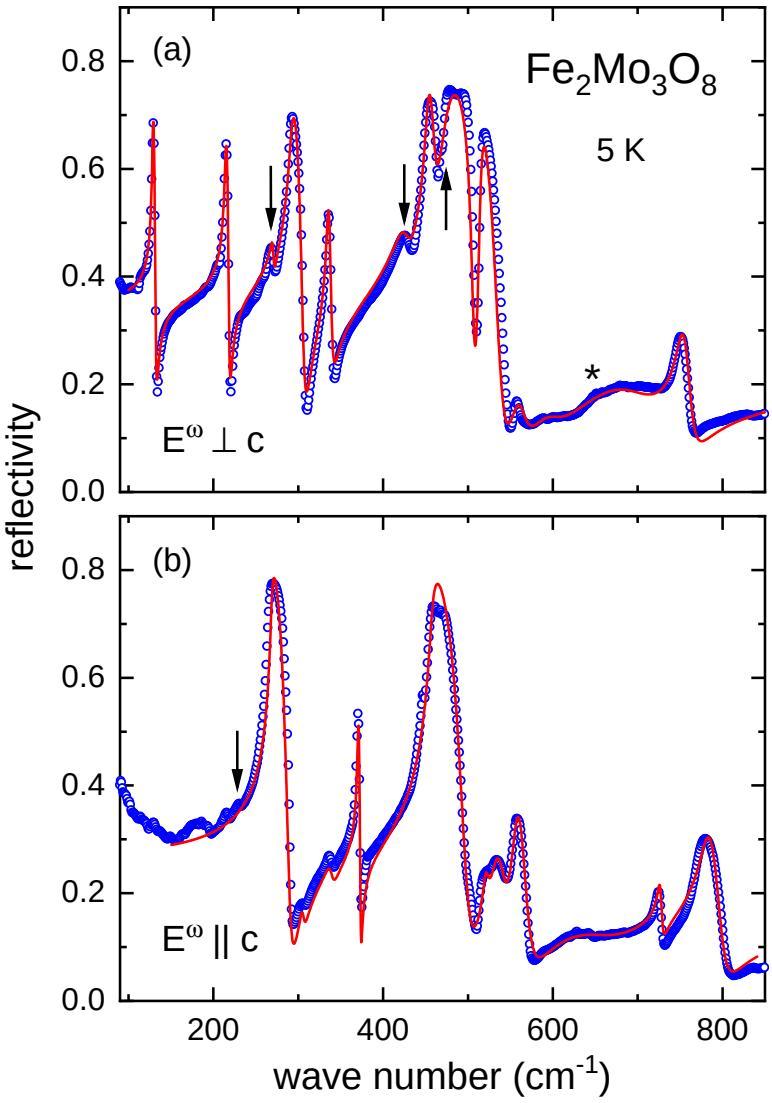

Figure 5.5.: Reflectivity spectra of $Fe_2Mo_3O_8$ at 5 K for polarization (a) $E^\omega \perp c$ and (b) $E^\omega \parallel c$ [59]. Arrows indicate the modes appearing only below T_N. The red solid lines represent the fits of the experimental data with the oscillator model from Eq. 5.2, as described in the text.

origin of this low-frequency increase is unknown and has not been observed in the previously reported reflectivity data [60]. From the fitting , the high-frequency dielectric constants have been determined as 7.6 for $E^\omega \perp c$ and 5.8 for $E^\omega \parallel c$ at the lowest temperature.

From the fitting of the reflectivity spectra the temperature dependence of the eigenfrequency ω_0 and the damping γ is obtained, which is shown for polarization $E^\omega \perp c$ in Fig. 5.6. All E_1 phonon modes exhibit clear anomalies in both the eigenfrequency and the damping at T_N. Already above T_N for some of the

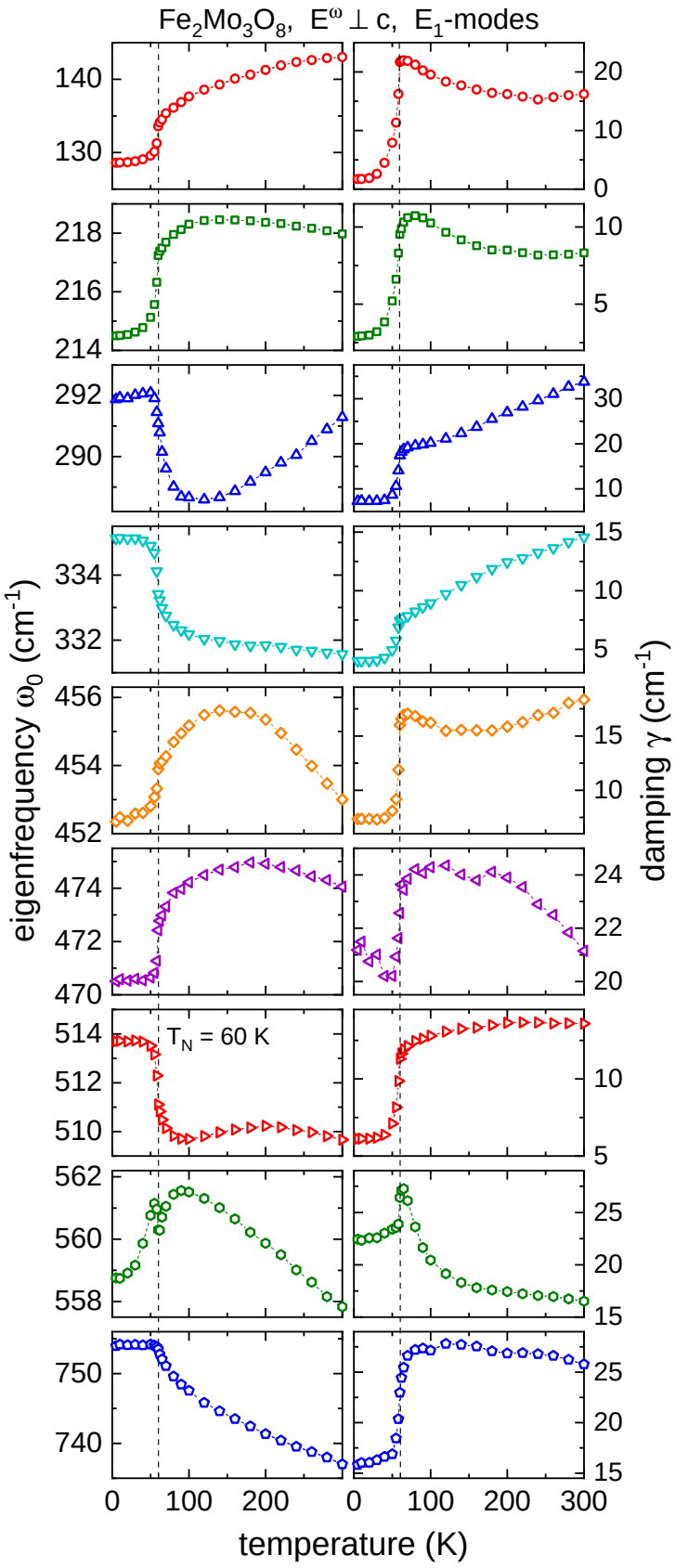

Figure 5.6: Temperature dependence of eigenfrequency ω_0 and damping γ of the strongest E_1 phonon modes active for $E^\omega \perp c$ [59]. The dashed lines indicate the magnetic ordering temperature of $T_N = 60\,\mathrm{K}$.

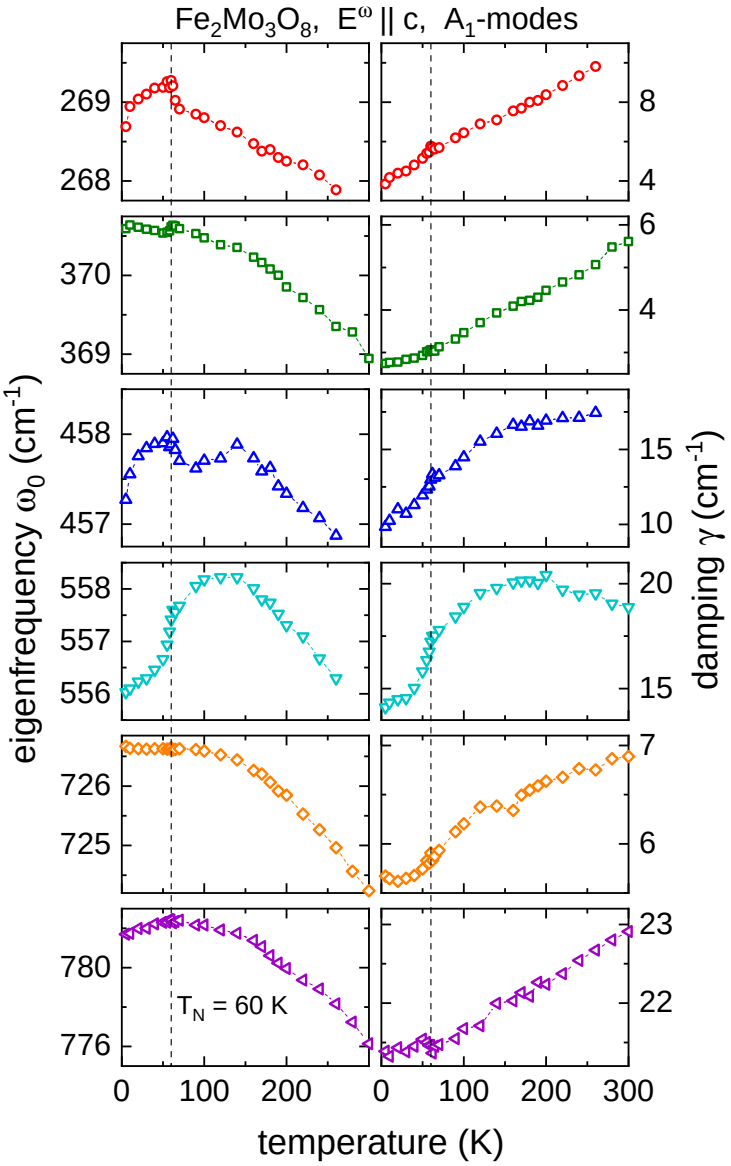

Figure 5.7: Temperature dependence of eigenfrequency ω_0 and damping γ of the strongest A_1 phonon modes active for $E^\omega \parallel c$ [59]. The dashed lines indicate the magnetic ordering temperature of $T_\mathrm{N} = 60\,\mathrm{K}$.

modes the eigenfrequency shows a non-monotonous behavior, such as for the modes at 454, 473 and 510 cm^{-1} around 200 K. Therefore, one may surmise a connection to the short-range magnetic ordering. Besides the sudden jumps of the eigenfrequencies at T_N, which happen both upwards and downwards, regarding the whole investigated temperature range there is no common discernible trend of the eigenfrequencies, either. Commonly, phonon frequencies often increase continuously towards lower temperatures due to anharmonic effects [182–185]. Such a hardening of the phonon modes would also be expected according to the temperature dependent DFT+U+SO calculations, as shown in Appendix A.3. However, such a behavior in not observed experimentally for most of the E_1 modes. Most significant is the temperature dependent behavior of the E_1 phonons at the

antiferromagnetic phase transition. As already evident from the sharpening of the phonons in the reflectivity spectra (see Fig. 5.3 (a)), the damping of all E_1 modes is considerably reduced below T_N. For the lowest-lying phonons this sudden change of the damping with the onset of antiferromagnetic ordering is up to one order of magnitude.

The temperature dependence of the eigenfrequencies and the dampings of the A_1 phonon modes, which are active for $E^\omega \parallel c$, is shown in Fig. 5.7. The A_1 modes exhibit a different temperature dependent behavior than the E_1 modes. The eigenfrequencies show an overall increase towards low temperatures, as commonly observed due to anharmonicity, arising from thermal expansion and phonon-phonon interactions [182–185]. Furthermore, the hardening of the phonons with decreasing temperature is in line with the DFT+U+SO calculations (see Appendix A.3). At T_N no or only minor anomalies of the eigenfrequencies are found. The damping of all A_1 phonons is continuously decreased on lowering the temperature. In contrast to the E_1 modes, the dampings of the A_1 modes show no sudden jumps when entering the antiferromagnetically ordered phase, but rather exhibit a smooth behavior when crossing T_N. It should be noted that the slight anomaly observed at T_N for the mode at 557 cm^{-1} could be related to difficulties in the fitting process due to the nearby overlapping feature of comparable strength stemming from polarization leakage from the $E^\omega \perp c$ direction.

Excitations related to short-range ordering

A further type of excitations is observed in the frequency range between 600 and 700 cm^{-1} for polarization direction $E^\omega \perp c$, as indicated by the asterisk ($*$) in Figs. 5.3–5.5. The temperature dependence of this broad spectral feature is shown in Fig. 5.3 (c). While it is not present in the room-temperature reflectivity, it starts to emerge below 200 K with the onset of short-range magnetic ordering and continuously gains spectral weight on decreasing the temperature.

This spectral feature could be successfully fitted with two Lorentzian oscillators located at approximately 600 and 700 cm^{-1}. The temperature dependent fitting parameters are shown in Fig. 5.8. For the mode around 700 cm^{-1} the eigenfrequency is nearly constant over the whole investigated temperature range. Its damping remains constant in the antiferromagnetically ordered phase and continuously increases with temperature above T_N. The eigenfrequency of the oscillator around 600 cm^{-1} is nearly constant both above and below T_N and exhibits a sudden drop when entering the magnetically ordered phase. Its damping is constant within the error bar. The temperature dependence of the overall oscillator strength of the two oscillators $\Delta\epsilon = \sum_{n=1}^{2} \omega_{p,n}^2/\omega_{0,n}^2$ is shown in Fig. 5.8 (e). Starting from 200 K, it continuously increases with decreasing temperature and gets saturated below T_N. This behavior is strongly resembling the anomalous temperature dependence of the lattice parameter c or the strain parameter S_{202} (see Fig. 5.1) and, thus, supporting

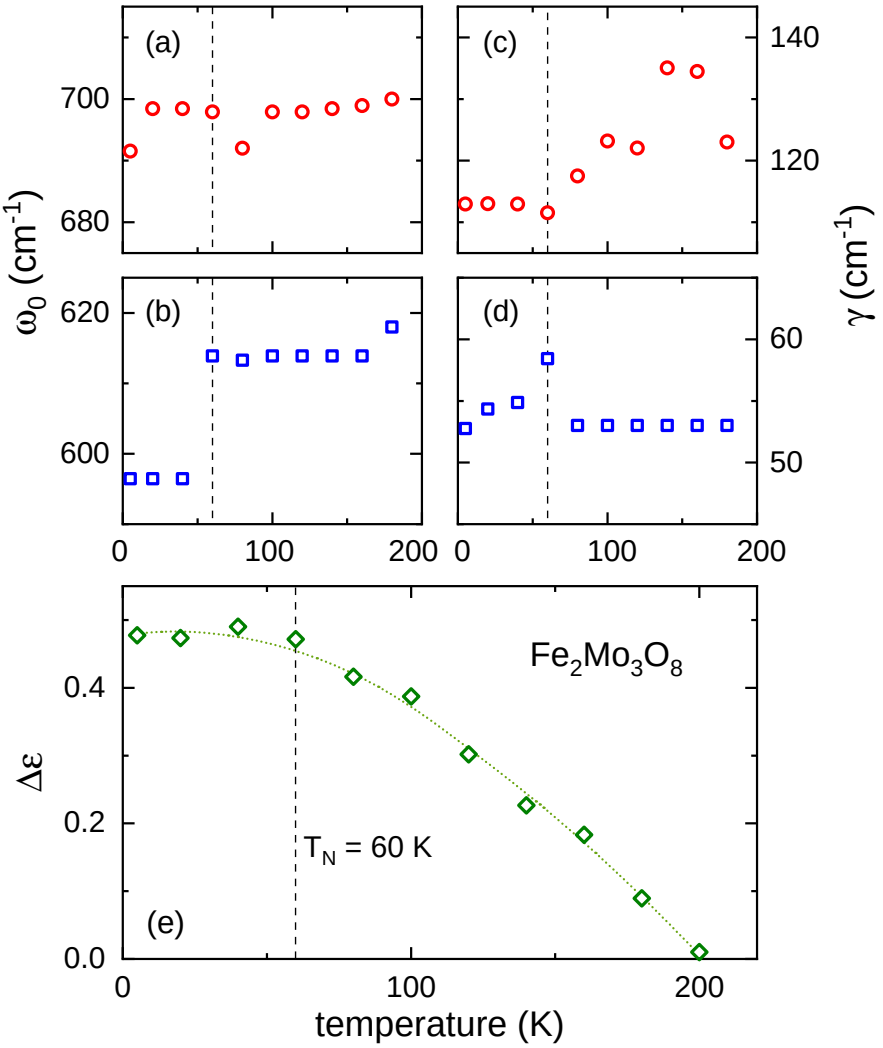

Figure 5.8.: Temperature-dependent (a), (b) eigenfrequencies and (c), (d) dampings of the two oscillators used for the modelling of the short-range order related feature observed for $E^\omega \perp c$ in the frequency range between 600 and 700 cm^{-1}. (e) Temperature dependence of the overall oscillator strength.

a short-range ordering origin of these spectral features. A purely phononic origin of these excitations seems excludable from the unusual broad spectral shape and the fact that no E_1 phonons are expected from the calculations in this frequency range, either (see Tab. 5.1).

Additional excitations below T_N

As indicated in Figs. 5.3–5.5, further FIR excitations appear in the spectra only below T_N. For polarization $E^\omega \perp c$ three additional excitations are observed at 270, 426 and 468 cm^{-1}. In the perpendicular polarization direction one addi-

tional excitation is identified at 230 cm^{-1}. In Ref. [60] all additional FIR excitations emerging below T_N have been assigned to phonon modes and consequently a symmetry lowering concomitant with the magnetic phase transition has been proposed. However, this scenario is excluded by the diffraction data. Besides, following the assignment of the excitations as done in the course of this work, the number of observed phonon modes does not exceed the number of the allowed IR active phonons of the $P6_3mc$ symmetry. As can be recognized from the FIR excitation frequencies summarized in Tab. 5.1, the additional modes observed for $E^\omega \perp c$ at 270 and 468 cm^{-1} may be assigned to the missing E_1 phonons, which would be expected from the DFT+U+SO calculations at 286 and 473 cm^{-1}. The modes observed at 426 cm^{-1} for $E^\omega \perp c$ and at 230 cm^{-1} for $E^\omega \parallel c$ have no counterpart in the calculations. As will be discussed later, for these excitations an origin related to electronic transitions seems possible.

d-d transitions of tetrahedral Fe^{2+}

In the following also the MIR *d-d* transitions of the tetrahedrally coordinated Fe^{2+} site are discussed, as the electronic transitions play an important role for the FIR excitations. As typical for tetrahedral Fe^{2+} [171–177], the *d-d* transitions show up in the frequency range between 3450 and 3500 cm^{-1}. This is illustrated in Figs. 5.9 (a) and (b), which show the MIR reflecticity for the two polarizations $E^\omega \perp c$ and $E^\omega \parallel c$ for a series of temperatures.

In the antiferromagnetically ordered phase at the lowest temperatures for both polarization directions the *d-d* transitions of the tetrahedral Fe^{2+} appear as sharp features in the reflectivity spectra. On increasing the temperature towards T_N the *d-d* transitions get gradually suppressed and broadened. Above T_N they are only visible as a broad feature.

The excitation energies have been determined from the peak maxima of the dielectric loss ϵ_2, as illustrated in Fig. 5.9 (c) and (d). Dependent on the polarization, excitation frequencies of 3472, 3485 and 3498 cm^{-1} are obtained for $E^\omega \perp c$ and 3446 cm^{-1} for $E^\omega \parallel c$. These observations are in agreement with the previously reported data [60].

It should be noted that the authors of Ref. [60] in addition report a broad feature around 3000 cm^{-1}, which was speculated to represent *d-d* transitions of the octahedral Fe^{2+}, although not observed in all of their studied samples. As evident from the reflectivity spectra shown in Fig. 5.2, this feature is not present in our measurements. Furthermore, in general the crystal field splitting of octahedral ions is bigger than that of tetrahedral ions [178, 179], thus, the *d-d* transitions of the octahedral Fe^{2+} ions should be located at considerably higher energies. Therefore, the feature around 3000 cm^{-1} reported in Ref. [60] may most likely not be related to the *d-d* transitions of the octahehral Fe^{2+} sites, but rather to e. g. defects.

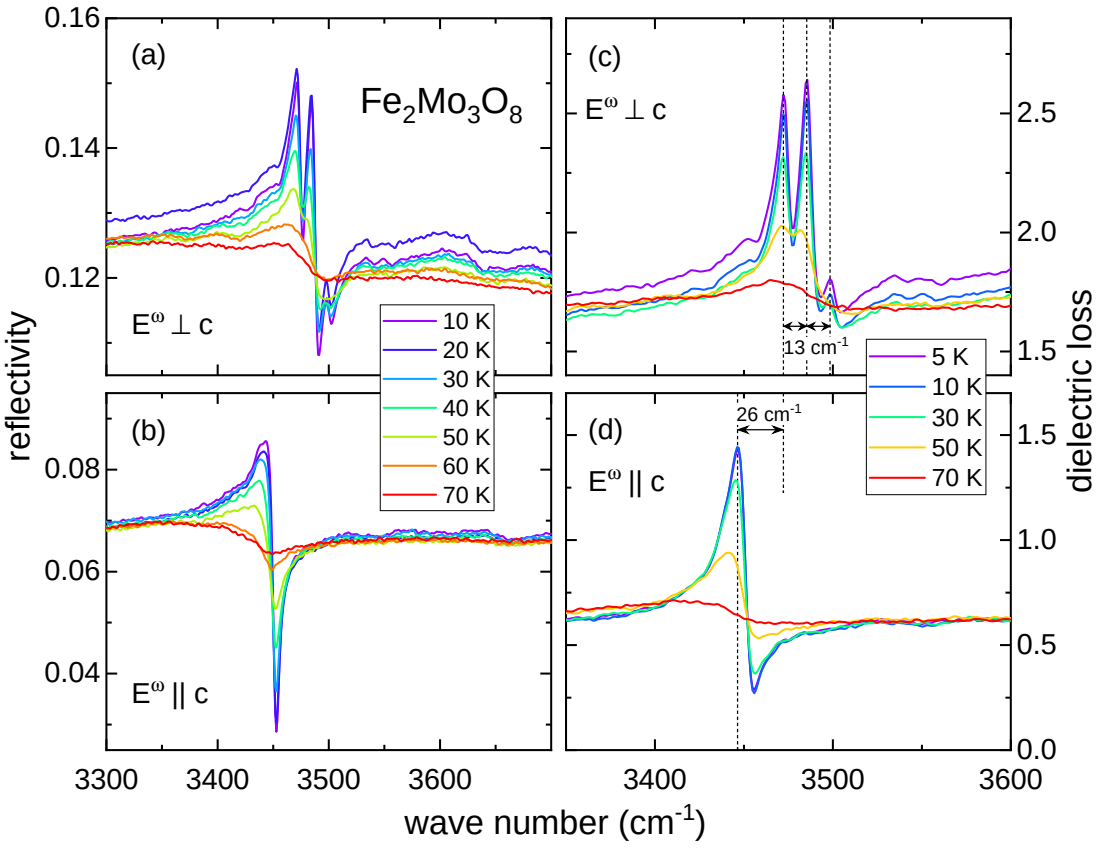

Figure 5.9.: (a), (b) Frequency-dependent MIR reflectivity of $Fe_2Mo_3O_8$ in the range of the *d*-*d* transitions for polarization $E^\omega \perp c$ and $E^\omega \parallel c$ for selected temperatures. (c), (d) Corresponding dielectric loss spectra [59]. Dashed lines indicate the excitation frequencies and illustrated the energy spacings of 13 and 26 cm^{-1}, respectively.

As illustrated in Fig. 5.9 (c) and (d), the *d*-*d* transitions exhibit either an equidistant spacing of 13 cm^{-1} or of twice this value of 26 cm^{-1}. These are the same frequency spacings as those already observed for the excitations found in the frequency range between 830 and 860 cm^{-1}. The *d*-*d* transitions may be interpreted in terms of the standard energy level scheme of the split ^5D term of tetrahedrally coordinated Fe^{2+} ions. In tetrahedral crystal field the ^5D level of the Fe^{2+} is split into a lower orbital doublet ^5E and an upper orbital triplet $^5T_2$ [168], which are separated in energy by the tetrahedral crystal field splitting $\Delta_t \approx 3400 - 3500\,\mathrm{cm}^{-1}$. As it will be discussed in more detail in connection with Fig. 5.10, in cubic symmetry the lower ^5E doublet is split by second order spin-orbit coupling into five equidistant levels. Their spacing is given by [168, 176]

$$\Delta_{\mathrm{SO}} = \frac{6\lambda^2}{\Delta_t}, \tag{5.3}$$

where λ denotes the spin-orbit coupling constant. With the experimental value of $\Delta_{\mathrm{SO}} = 13\,\mathrm{cm}^{-1}$ and assuming cubic symmetry, the spin-orbit constant can be estimated. Equation 5.3 yields a value of $\lambda = 87\,\mathrm{cm}^{-1}$, which is in satisfactorily agreement with the spin-orbit coupling constant reported for tetrahedral Fe^{2+} in other compounds [176, 186].

Discussion

As described above, in the room-temperature FIR spectra nine out of the twelve E_1 phonon modes and eight out of the nine allowed A_1 modes could be observed. While the A_1 modes exhibit the common anharmonic temperature dependence in line with the DFT+U+SO calculation of the phonons, the E_1 modes show a rather anomalous behavior with a partly non-monotonic temperature dependence of the eigenfrequencies and especially with a significant increase of the phonon lifetime below T_{N}. The latter may be explained by a quenching of fluctuations of the orbital moment, as will be discussed in the following.

The energies of the crystal-field levels of the octahedrally and tetrahedrally coordinated Fe^{2+} ions in $Fe_2Mo_3O_8$ have been determined from DFT by Dr. Alexander Tsirlin by projecting the calculated band structure onto Wannier functions. The corresponding crystal-field level diagram is shown in Fig. 5.10. From the calculations crystal-field splittings of $\Delta_o = 0.68\,\mathrm{eV}$ and $\Delta_t = 0.33\,\mathrm{eV}$ are obtained for the octahedral and the tetrahedral site, respectively. Although somewhat lower than the observed *d-d* transitions, the latter value is in reasonable agreement with the experimentally determined energy.

In an undistorted structure both the octahedral and the tetrahedral high-spin Fe^{2+} ions posses orbital degrees of freedom. The weak trigonal distortion in $Fe_2Mo_3O_8$ results in further secondary splittings $\delta_o = 0.17\,\mathrm{eV}$ and $\delta_t = 0.02\,\mathrm{eV}$ of the triplet states on the octahedral and the tetrahedral sites, respectively, as illustrated in Fig. 5.10. With the minority-spin electron occupying the a_1 orbital, the orbital degeneracy gets lifted and orbital degrees of freedom are quenched on the octahedral Fe^{2+} sites. In contrast, the lower e_1 orbital of the tetrahedrally coordinated Fe^{2+} sites remains doubly degenerate under the trigonal distortion. This degeneracy is only lifted by spin-orbit coupling concomitant with a considerable orbital moment. In the case of $\delta_t = 0$, spin-orbit coupling creates equally spaced levels separated by Δ_{SO}, as given by Eq. 5.3. Thus, the observed *d-d* transitions with equal spacings of 13 and $26\,\mathrm{cm}^{-1}$, respectively, strongly support a $\delta_t \ll \lambda$ scenario and the calculated value of δ_t may rather be considered as an approximation.

From the calculations also the orbital moment could be determined. For the octahedral Fe^{2+}, where the orbital degeneracy is lifted by the trigonal distortion, expectedly only a negligible orbital moment below $0.01\,\mu_{\mathrm{B}}$ is found. For the tetrahedrally coordinated Fe^{2+} sites the calculations yield a orbital moment of $0.5\,\mu_{\mathrm{B}}$

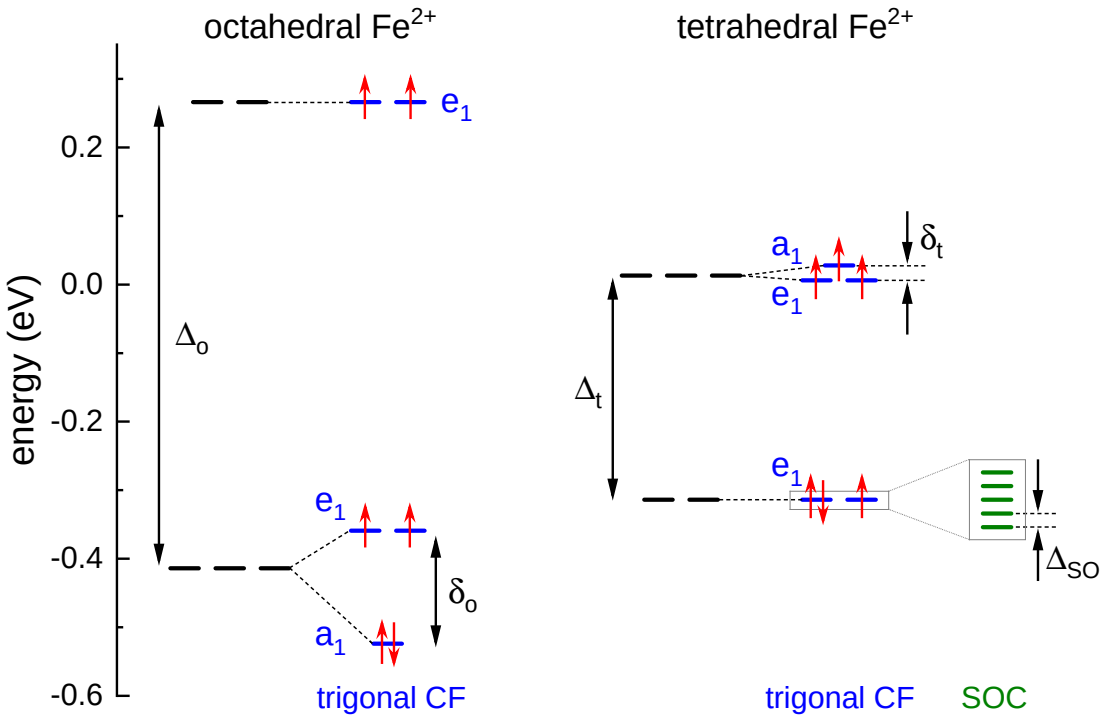

Figure 5.10.: Crystal-field levels of the octahedrally and the tetrahedrally coordinated Fe^{2+} ions in $Fe_2Mo_3O_8$. The energies E were calculated by DFT, including splittings from the trigonal crystal field (CF). $E = 0$ corresponds to the Fermi level of the uncorrelated band structure. Δ_{SO} indicates the splitting of the lower e_1 orbital of tetrahedral Fe^{2+} due to spin-orbit coupling (SOC) in the $\delta_t = 0$ limit.

along the c-axis, in agreement with the enhanced ordered moment exceeding the spin-only value (c. f. section 5.1.1). Furthermore, in line with the experimentally determined magnetic structure, the calculations reveal a strong easy-axis anisotropy with not only the spins, but also the orbital moment being preferably oriented along the c-axis.

Orbital degrees of freedom may be the reason for the sudden increase of the phonon lifetime of the E_1 modes when entering the antiferromagnetically ordered phase. As this anomalous behavior is only observed for the E_1 modes, it seems natural to relate these to the e_1 electronic levels of the tetrahedral Fe^{2+} with the same symmetry, which exhibit the orbital degeneracy. In this case, fluctuations of the direction of the orbital moment can occur as long as no magnetic order is established. As described above, the direction of the orbital moment is expected to be along the c-axis, but it is not fixed and can point either in the $+c$ or the $-c$ direction. With the onset of magnetic ordering, below T_N the direction of the orbital moment gets fixed by the internal fields and, consequently, the fluctuations of the direction of the orbital moment are quenched, which is reflected in the temperature dependence of the E_1 modes.

Besides the unambiguously identified E_1 and A_1 phonon modes, further excitations observed for temperatures above T_N cannot be classified as phonons. The weak excitations found for both $E^\omega \perp c$ and $E^\omega \parallel c$ in the frequency range around 850 cm^{-1} exhibit the same energy spacings as the *d-d* transitions of the tetrahedral Fe^{2+} sites and are furthermore affected by the short-range magnetic ordering below 200 K, where additional modes emerge in the frequency range between 600 and 700 cm^{-1}. These findings suggest a combined vibrational and electronic origin of these excitations. The observation of a splitting of 13 cm^{-1} of the lowest lying *d*-levels is in agreement with the onset of the presumably vibronic excitation at 12 cm^{-1} in the THz spectra of $Fe_{1.86}Zn_{0.14}Mo_3O_8$, as discussed in section 4.2.2.

Concerning the four additional excitations becoming visible in the FIR spectra below T_N, only two of them might be considered as phonons of the $P6_3mc$ symmetry. Furthermore, it is not fully clear if some of these additional modes are already present above T_N and only become explicitly visible below T_N, e. g. due to sharpening similar to the E_1 modes. Weak signatures of the mode at 270 cm^{-1} ($E^\omega \perp c$) might already be barely visible at 100 K. In the spectra of Ref. [60] the excitation observed for $E^\omega \parallel c$ at 230 cm^{-1} is already visible above T_N. Therefore, for this class of excitations either a combined phononic and magnonic or a combined phononic and electronic origin seems plausible. In any case, the FIR spectra down to the lowest temperature give no reason for claiming a symmetry lowering in $Fe_2Mo_3O_8$, as also excluded by the structural measurements.

It should be noted that a energy level scheme different from that shown in Fig. 5.10, explicitly derived for tetrahedral Fe^{2+} in $Fe_2Mo_3O_8$, has already been reported earlier by Varret *et al.* [44]. This level scheme is reproduced in Appendix A.4. In this case, again the *d* levels of the free Fe^{2+} ion are split by the tetrahedral crystal field into a lower *e* doublet and a upper t_2 triplet separated by $\Delta_t \approx 3500\,cm^{-1}$. The autors of Ref. [44] point towards the importance of a forth order crystal field term, which was included in their model to describe the temperature dependence of their Mössbauer data. According to this calculations, the trigonal crystal field splits the upper t_2 level by a large δ_t and, thus, lowers the energy of one level so that it comes close to the lower doublet. The lowest levels are further split by spin-orbit and spin-spin coupling, and under a molecular field HS_z accounting for the magnetism of the compound. This rather unconventional level scheme would in principle allow the interpretation of additional excitations, as observed in the FIR beyond phonons, in terms of electronic transitions. Besides, it yields a similar energy of 14 cm^{-1} for the first excited state. However, this scenario of $\lambda \ll \delta_t \simeq \Delta_t$ is not supported by our DFT calculations and does not result in equally spaced *d-d* transitions, either.

5.2. Sytematics of phonon excitations in lacunar spinels AM_4X_8

The phonons in the studied lacunar spinels are found in the FIR range up to 500 cm^{-1}. Fig 5.11 shows the frequency-dependent phonon spectra measured at room temperature in the cubic $F\bar{4}3m$ phase (red spectra) and at 10 K in the Jahn-Teller distorted ($R3m$, $Imm2$, $P\bar{4}2_1m$, $P\bar{4}m2$) and magnetically ordered phase (blue spectra). For single-crystalline samples of GaV_4S_8, GeV_4S_8, $GaMo_4S_8$, $GaNb_4S_8$, AlV_4S_8, $AlMo_4S_8$ and GaV_4Se_8 the reflectivity spectra R were obtained from as-grown (111) surfaces. For $AlMo_4S_8$, $GaMo_4Se_8$ and $GaTa_4Se_8$ no single-crystalline samples were available. Therefore, in this case the transmission T was measured on polycrystalline samples, which were prepared as described in section 3.3.2. The phonons show up as clearly pronounced resonances in the spectra. For $GaMo_4S_8$ and $GaNb_4S_8$ the reflectivity spectra show a slight increase towards low frequencies below approximately 300 - 400 cm^{-1}. Although the origin of this low-frequency upturn of the reflecticity is not fully clear at present, these features were found to be reproducible.

Before having a closer look at the phonon spectra, at first some group theory aspects shall be considered. From the crystal symmetry and the occupied Wyckoff positions group theory directly allows to determine the allowed zone center optical phonon modes. In the high-temperature phase all studied lacunar spinels have cubic symmetry $F\bar{4}3m$. With the Wyckoff positions from Ref. [68] the following allowed phonon modes are obtained for the A site, the M site and the two different ligand sites X_1 and X_2:

$$\begin{aligned} \Gamma_A &= F_2 \\ \Gamma_M &= A_1 + E + F_1 + 2F_2 \\ \Gamma_{X_1} &= A_1 + E + F_1 + 2F_2 \\ \Gamma_{X_2} &= A_1 + E + F_1 + 2F_2 \end{aligned} \tag{5.4}$$

From this follows the total number of zone-center phonon modes of the lacunar spinels in the high-temperature cubic state:

$$\Gamma_{F\bar{4}3m} = 3A_1 + 3E + 3F_1 + 7F_2 \tag{5.5}$$

Out of these modes only the F_2 modes are IR active. Furthermore, one of the triply degenerate F_2 phonon modes accounts for the three acoustic modes, which are not observed by IR spectroscopy. This results in six IR-active phonon modes in the $F\bar{4}3m$ cubic state:

$$\Gamma^{\mathrm{IR}}_{F\bar{4}3m} = 6F_2 \tag{5.6}$$

Similarly, also for the low-temperature symmetries the number of IR-active phonon modes can be determined. Below T_{JT} the number of allowed phonon modes increases due to the lowering of the crystal symmetry. With the acoustic modes already being subtracted, from the structural data of Ref. [68] 21 IR-active phonon modes are obtained for the rhombohedral symmetry $R3m$, which is found in GaV_4S_8, $GaMo_4S_8$, AlV_4S_8, $AlMo_4S_8$, GaV_4Se_8 and $GaMo_4Se_8$:

$$\Gamma^{\mathrm{IR}}_{R3m} = 9A_1 + 12E \tag{5.7}$$

For the orthorhombic low-temperatrure symmetry $Imm2$ of GeV_4S_8 [84] group theory predicts a total number of 30 IR-active phonons:

$$\Gamma^{\mathrm{IR}}_{Imm2} = 12A_1 + 9B_1 + 9B_2 \tag{5.8}$$

For the tetragonal phase with space group symmetry $P\bar{4}2_1m$ [78] the symmetry analysis results in 58 allowed IR-active phonon modes:

$$\Gamma^{\mathrm{IR}}_{P\bar{4}2_1m} = 21B_2 + 37E \tag{5.9}$$

The tetragonal space group $P\bar{4}2_1m$ was previously reported for $GaNb_4S_8$ and $GaTa_4Se_8$ below T_{JT}, however, the exact low-temperature symmetry of these compounds is still under debate [80, 81, 118] (see section 2.5).

The FIR measurements allow to trace the symmetry lowering structural phase transition in the lacunar spinels by the appearing of additional phonons below T_{JT}, although in each case only a subset of the IR-allowed zone-center phonon modes could be observed experimentally, as evident from the spectra shown in Fig. 5.11. The spectral weight of the remaining modes obviously is too small to be detected in these measurements.

As indicated by the red triangles in Fig. 5.11, in the case of GaV_4S_8 four out of the six IR-allowed F_2 phonon modes can be observed in the cubic phase in the frequency range between 300 and 450 cm^{-1} by FIR spectroscopy. The two remaining weak modes have been detected at 130 and 193 cm^{-1} by Raman spectroscopy [187]. Due to the symmetry lowering from cubic to rhombohedral, two additional phonon modes appear below $T_{\mathrm{JT}} = 44\,\mathrm{K}$. Below the magnetic ordering temperature $T_{\mathrm{C}} = 13\,\mathrm{K}$ no additional phonons can be observed and also the phonon parameters are not affected by the magnetic ordering.

In GeV_4S_8 also four phonon modes can be identified at room temperature. Despite some differences in their relative oscillator strengths, their eigenfrequencies are very similar to those observed in GaV_4S_8, which can be understood by the similar atomic masses of Ga (69.7 u) and Ge (72.6 u). Three additional modes are observed when entering the orthorhombic phase at $T_{\mathrm{JT}} = 30\,\mathrm{K}$. Moreover, in GeV_4S_8 three more modes appear in the antiferromagnetically ordered phase

below $T_N = 15\,K$, as indicated by the green arrows in Fig. 5.11. The appearance of additional modes at T_N in GeV_4S_8 is a distinct feature among the studied lacunar spinels. For better comparison, in addition the 25 K spectrum is included in the insets as green curve. Although the lattice symmetry is not further reduced, further lattice distortions at T_N have been reported in GeV_4S_8 [84]. Besides, the appearing of additional modes below T_N may be explained by the observed doubling of the unit cell due to the antiferromagnetic ordering [75] in combination with spin-lattice coupling.

In the case of $GaMo_4S_8$ four phonon modes are observed at room temperature, which surprisingly have eigenfrequencies very similar to GaV_4S_8 and GeV_4S_8, despite the large difference of the masses of V (50.9 u) and Mo (96.0 u). The two phonon modes located at 305 and 370 cm^{-1} dominate the spectrum, whereas the two further modes are comparatively weak. When the symmetry is reduced from cubic to rhombohedral at $T_{JT} = 45\,K$, six additional phonon modes appear in the spectrum, which all have only low spectral weight compared to the two dominating modes. To make the changes in the spectrum upon crossing T_{JT} more visible, the spectrum measured at 50 K, just above the phase transition, is included as a green curve in the insets. In $GaMo_4S_8$ no changes in the phonon spectrum are identified upon magnetic ordering below $T_C = 20\,K$.

In $GaNb_4S_8$ three phonon modes are observed in the high-temperature cubic phase. It is natural to compare the spectrum of $GaNb_4S_8$ with those of GaV_4S_8 and $GaMo_4S_8$ in order to elucidate the influence of exchanging the M-site ion on the phonons, as these three compounds only differ in the M site. The phonon frequencies in $GaNb_4S_8$ are only slightly, but not significantly lower than in GaV_4S_8 and $GaMo_4S_8$. Furthermore, the relative oscillator strength of the phonon modes in these three compounds is similar. These findings suggest that the phonon spectra are not significantly affected by the M-site ion. In $GaNb_4S_8$, where the structural and magnetic phase transition occur concomitantly, one weak additional mode appears below 32 K.

The reflectivity measurements on AlV_4S_8 reveal three IR-active phonon modes at room temperature. The eigenfrequencies in the range from 300 to 450 cm^{-1} are again very similar to the previously described compounds, although the atomic mass of Al (27.0 u) is less than half of the atomic mass of Ga (69.7 u). While the phonon frequencies are only weakly influenced by the exchange of Ga by Al, the relative strength of the phonon modes in AlV_4S_8 is different compared to the Ga compounds, with the modes at 315 and 445 cm^{-1} clearly dominating the phonon response. Below $T_{JT} = 40\,K$ in the lower-symmetry rhombohedral phase three additional modes are identified. No additional phonon modes upon magnetic ordering could be observed, however, the reported $T_C = 10\,K$ is the lower temperature limit of the used optical cryostat. Therefore, it is not clear, if the magnetically ordered phase was really established in the experiment.

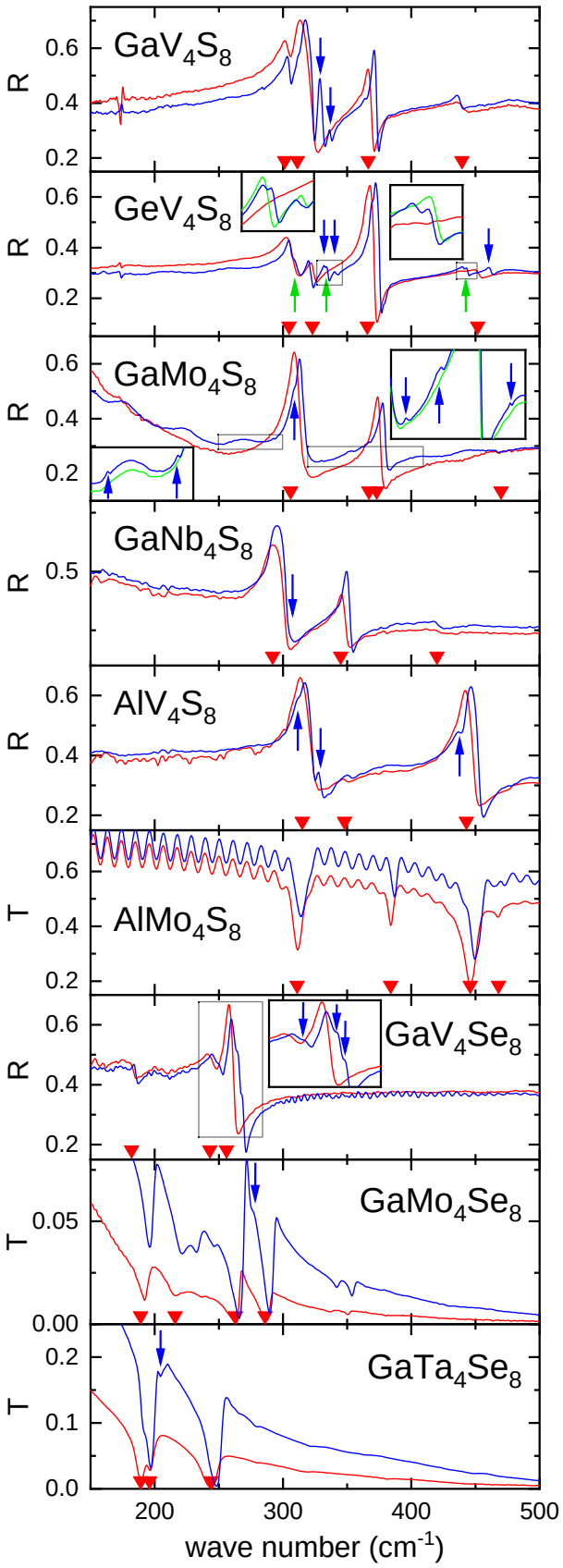

Figure 5.11: Frequency dependent FIR phonon spectra of the studied lacunar spinels measured at room temperature (red curves) and at 10 K (blue curves) [169]. For single crystalline samples the reflectivity was measured on as-grown (111) surfaces. Transmission spectra were obtained from polycrystalline samples. Red triangles indicate the phonon frequencies at room temperature. Phonons appearing below T_{JT} are marked with blue arrows. Green arrows indicate additional modes observed below the magnetic ordering temperature. For GeV_4S_8 the 25 K spectrum and for $GaMo_4S_8$ the 50 K spectrum is included in addition (green curves) for better comparison. The insets show zoom-ins of weak phonon modes.

In the case of $AlMo_4S_8$ four phonon modes are observed in the transmission spectrum in the cubic phase. As evident from Fig. 5.11, in this compound no additional modes could be identified down to the lowest temperatures. With the phonon excitations being found once more in the same frequency range, the two strongest modes in $AlMo_4S_8$ are located at 310 and 445 cm^{-1}, like in AlV_4S_8. The comparison of the relative mode strengths makes the Al compounds distinct from their Ga analogues. This reveals the impact of the *A*-site ions on the oscillator strengths.

A clear change in the phonon spectrum can be observed when replacing S with Se. In the studied selenides the IR-active phonon modes are found in the frequency range between 180 and 270 cm^{-1}, which is considerably lower than in the sulfides. The lower phonon eigenfrequencies in the selenides can be directly understood by the different masses of S and Se. The simplest approach for the description of phonons is the model of the harmonic oscillator. Within this model the ratio of the phonon frequencies of the Se and S compounds can be connected to the mass ratio of S and Se as follows:

$$\frac{\omega_{\mathrm{Se}}}{\omega_{\mathrm{S}}} = \sqrt{\frac{m_{\mathrm{S}}}{m_{\mathrm{Se}}}} = 0.64 \tag{5.10}$$

As it will be shown later explicitly, the phonon frequencies of the lacunar spinels follow this ratio. This observation clearly suggests that the ligand ions are strongly involved in the phonon response of these compounds.

In GaV_4Se_8 three out of the six IR-allowed zone-center F_2 modes can be identified in the reflectivity spectrum of the cubic phase. While three additional phonons appear when entering the rhombohedral phase at $T_{\mathrm{JT}} = 41$ K, no changes in the spectrum can be found below $T_{\mathrm{C}} = 18$ K.

When comparing the FIR spectra of GaV_4Se_8, $GaMo_4Se_8$ and $GaTa_4Se_8$, which differ in the transition metal site, again only a minor influence of the *M*-site ion on the phonon frequencies can be discerned, which is in line with the observations in the sulfides. The measurements on polycrystalline $GaMo_4Se_8$ reveal four phonon modes at room temperature. The features in the spectrum around 350 cm^{-1} were observed in different $GaMo_4Se_8$ pellets, irrespective of the corresponding sample concentration and are therefore not considered as phonons of $GaMo_4Se_8$. One additional mode is found in the rhombohedral phase below $T_{\mathrm{JT}} = 25$ K, while entering the magnetically ordered phase happens without changes to the measured FIR spectrum. In the case of $GaTa_4Se_8$ three phonon modes can be observed at room temperature and one more mode is identified below the magnetostructural transition temperature of 53 K in the tetragonal phase.

A general aspect of the phonon modes in the studied lacunar spinels is their hardening with decreasing temperature. When comparing the phonon spectra obtained at room temperature and at 10 K in Fig. 5.11, a shift of the modes towards

higher frequencies is clearly observed in the 10 K spectra for all phonon modes that are already present at room temperature. As already mentioned in section 5.1, such an anharmonic temperature dependence is a commonly found behavior of phonons originating from thermal expansion and phonon-phonon interactions [182–185]. It has been shown that the anharmonic shift of the i-th phonon mode as a function of temperature can be described by the following expression [188–190]:

$$\omega_{0,i}(T) = \omega_{0,i}(T=0) \cdot \left(1 - \frac{c_i}{\exp\left(\frac{\hbar\Omega}{k_\mathrm{B}T}\right) - 1}\right) \tag{5.11}$$

Here $\omega_{0,i}(T=0)$ is the phonon frequency of the i-th mode in the $T = 0\,\mathrm{K}$ limit. The parameters c_i account for the strength of the anharmonic shift of the respective mode and Ω is a characteristic frequency of the decayed phonons [189]. This formula describes a continuous increase of the eigenfrequency with decreasing temperature saturating at $\omega_{0,i}$.

In order to determine the temperature dependence of the phonon modes from the experimental data, the spectra were fitted by a sum of n Lorentz oscillators. As already mentioned in section 5.1, within this standard model of damped harmonic oscillators the complex dielectric permittivity is obtained from Eq. 5.2 by setting $\omega_{q,i} = 0$. With $\Delta\epsilon_i = \omega_{p,i}^2/\omega_{0,i}^2$ it follows [144]:

$$\epsilon(\omega) = \epsilon_\infty + \sum_{i=1}^{n} \frac{\omega_{p,i}^2}{\omega_{0,i}^2 - \omega^2 - i\omega\gamma_i} = \epsilon_\infty + \sum_{i=1}^{n} \frac{\Delta\epsilon_i\omega_{0,i}^2}{\omega_{0,i}^2 - \omega^2 - i\omega\gamma_i} \tag{5.12}$$

For the fitting of the measured data again the RefFIT routine [180, 181] was used.

In Fig. 5.12 exemplarily the temperature dependence of the eigenfrequencies of the two strongest phonon modes in $GaMo_4S_8$ and GaV_4Se_8 is shown in a semilogarithmic representation. All four modes exhibit the same qualitative temperature dependent behavior in the cubic phase. Starting at room temperature, the frequencies monotonically increase on lowering the temperature. Upon approaching T_JT the curves gradually flatten. The overall increase of the phonon frequencies in lacunar spinels in the temperature range between room temperature and 10 K is of the order of 3 - 7 cm^{-1}. As indicated by the red solid lines in Fig. 5.12, the fits of the temperature dependent ω_0 are in excellent agreement with the experimental data. For the characteristic frequency Ω the fit yields values of 292 cm^{-1} for $GaMo_4S_8$ and 172 cm^{-1} for GaV_4Se_8. These values are in line with the interpretation of Ω as an average phonon frequency [188, 189]. Furthermore, their ratio of 0.59 is close to the value of 0.64 expected from Eq. 5.10. The deviation of the mode frequencies from the anharmonic behavior below T_JT is a consequence of the crystal symmetry lowering. For both compounds the eigenfrequencies of the phonon modes are not

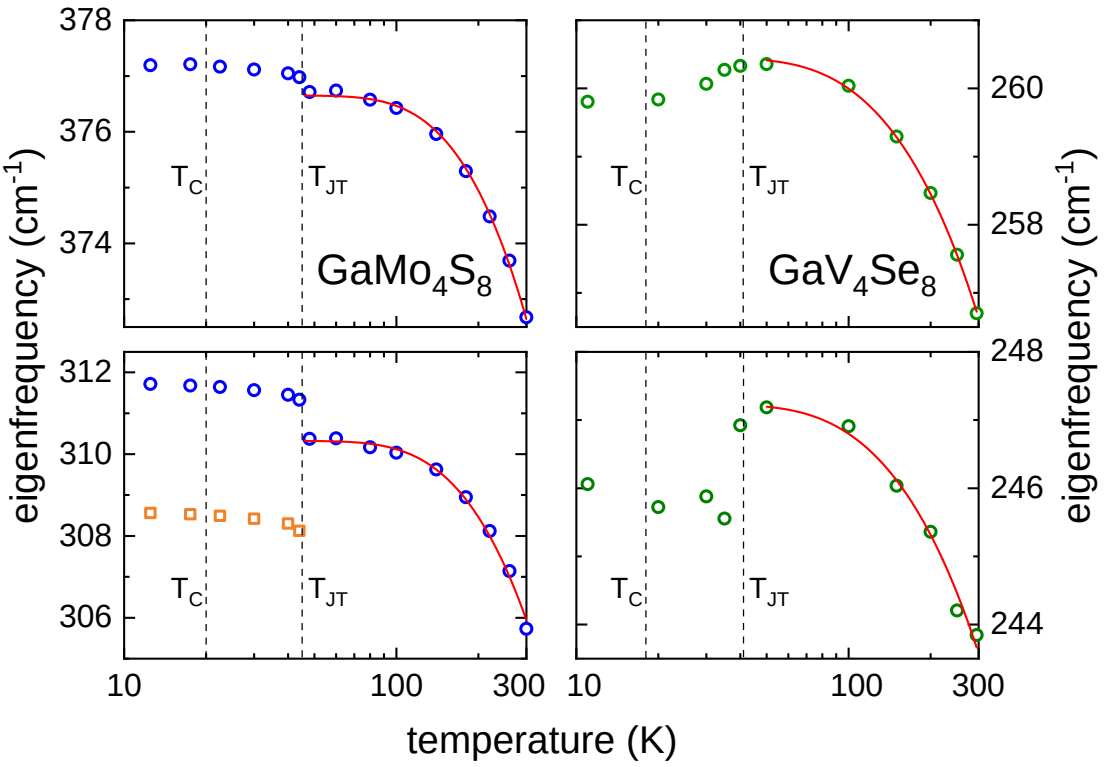

Figure 5.12.: Semilogarithmic plot of the temperature-dependent eigenfrequencies ω_0 of the two strongest phonon modes in $GaMo_4S_8$ (left) and GaVSe (right). Dashed vertical lines indicate the phase transition temperatures. Red solid lines represent fits of the experimental data with the anharmonic model from Eq. 5.11, as described in the text.

affected by the magnetic transition within the experimental accuracy, which is in accordance with the observations discussed in connection with Fig. 5.11.

We have also reported similar findings in GaV_4S_8 and GeV_4S_8 earlier [191], where we have analyzed the temperature dependence of ω_0 in detail: Also in these two compounds the temperature dependence of ω_0 for all modes is described by Eq. 5.11 with a value of $\Omega = 243\,\mathrm{cm}^{-1}$ similar to the one found in $GaMo_4S_8$. Slight deviations from the anharmonic behavior above T_{JT} may be ascribed to orbital fluctuations. While in none of the other investigated lacunar spinels changes in the phonon spectrum due to magnetic ordering were observed, in the antiferromagnetic phase of GeV_4S_8 not only additional modes were identified, but also shifts in the phonon parameters were found [191], making this compound distinct from the other studied lacunar spinels.

Figure. 5.13 shows the frequency dependence of the real part ϵ_1 and imaginary part ϵ_2 of the complex dielectric permittivity of the investigated compounds in the FIR range at 10 K and at room temperature. In the case of the singlecrystalline samples (GaV_4S_8, GeV_4S_8, AlV_4S_8, GaV_4Se_8, $GaMo_4S_8$, $GaNb_4S_8$) ϵ_1 and ϵ_2 were

directly obtained from the reflectivity spectra by the so-called variational dielectric function method (VDF), which was developed by A. Kuzmenko [180, 181] and allows to determine the complex dielectric function without the need of a high-frequency extrapolation and consecutive Kramers-Kronig transformation. For the polycrystalline samples ($AlMo_4S_8$, $GaTa_4Se_8$, $GaMo_4Se_8$), which were embedded in polyethylene, an exact determination of the dielectric function is more difficult, as the actual sample thickness is not well-defined and also an absolutely homogeneous distribution of the sample powder over the pellet might not always be perfectly realized. In this case, according to the sample concentration in the pellet, only an effective sample thickness could be determined. This allowed to estimate ϵ_2 from the transmission data. For these spectra a baseline was subtracted in order to account for the polyethylene background.

As already mentioned before, the reflectivity spectra of $GaNb_4S_8$ and especially of $GaMo_4S_8$ exhibit an increase towards low frequencies. In the case of $GaMo_4S_8$ this circumstance results in obviously unrealistic ϵ curves on the low-frequency side of the spectra. For this reason, the low-frequency increase of R in $GaMo_4S_8$, possibly originating from a higher conductivity at the sample surface, was modeled by a Drude term, which describes the behavior of free charge carriers. Its contribution to the complex dielectric permittivity is given by

$$\epsilon(\omega) = -\frac{\omega_p^2}{\omega^2 + i\omega\gamma}, \tag{5.13}$$

which formally corresponds to a Lorentz oscillator with $\omega_0 = 0$. At 10 K this Drude term can be described by the parameters $\omega_p = 950\,\mathrm{cm}^{-1}$ and $\gamma = 235\,\mathrm{cm}^{-1}$, which only have a minor temperature dependence. Afterwards, the Drude contribution was subtracted from the permittivity to obtain the $GaMo_4S_8$ spectra shown in Fig. 5.13. As indicated by the open circles, now the low-frequency dielectric constant is in agreement with the values obtained at $100\,\mathrm{cm}^{-1}$ from THz-TDS transmission measurements on the same crystal. While the reflectivity measurement mainly probes the sample surface, the transmission measurement mainly probes the bulk of the crystal. This confirms that the increase of R in $GaMo_4S_8$ towards low frequencies most likely can be ascribed to an enhanced conductivity at the sample surface. In $GaNb_4S_8$, however, the situation is less clear, as the same procedure was not applicable in this case.

In GaV_4S_8 and GeV_4S_8, where the crystal size was large enough, the complex dielectric permittivity obtained from the reflectivity could also be verified by THz-TDS measurements, which allow a very precise determination of ϵ. For all investigated single-crystalline samples the high-frequency ϵ_1 is in the range between 10 and 20. The dielectric loss ϵ_2 of these compounds, which is otherwise close to zero, typically reaches values from 30 to 60 for the strongest phonon modes. In the case of GaV_4S_8 and GeV_4S_8 the calculated ϵ_2 at 10 K for some frequencies

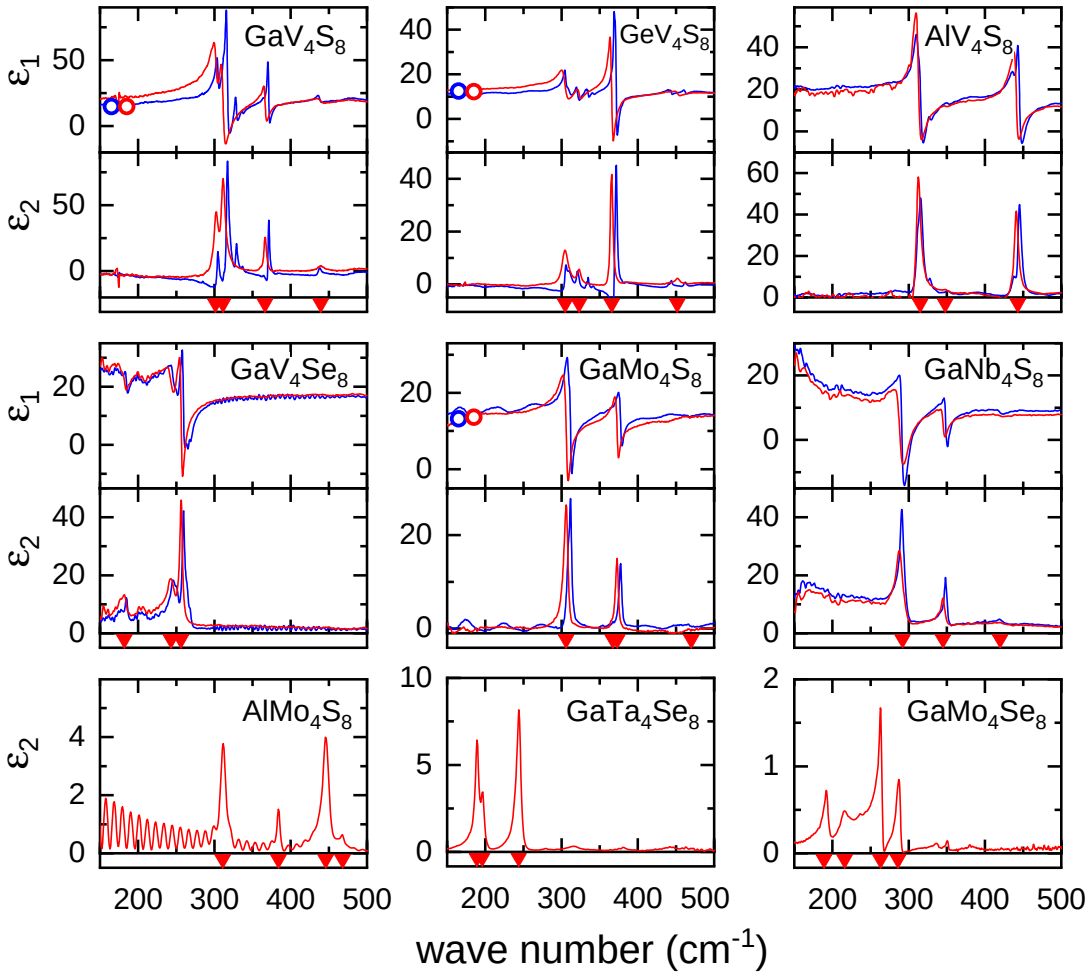

Figure 5.13.: Frequency-dependent real part ϵ_1 and imaginary part ϵ_2 of the complex dielectric permittivity in the FIR range [169]. Red and blue curves represent the spectra obtained at room temperature and 10 K, respectively. Red triangles indicate the phonon eigenfrequencies at room temperature. The open circles represent the values of ϵ_1 at 100 cm^{-1} obtained from THz-TDS transmission measurements.

reaches slightly negative values. This obviously results from a small background on the experimental reflectivity data, which apparently is also temperature dependent and therefore cannot be easily corrected.

For the polycrystalline samples, where only ϵ_2 could be calculated via an effective sample thickness, the determined absolute values are considerably lower. In this case, ϵ_2 reaches only values between 2 and 8 at the strongest phonon modes. It seems very unlikely that the dielectric loss for the phonons in $AlMo_4S_8$, $GaTa_4Se_8$ and $GaMo_4Se_8$ is approximately one order of magnitude smaller than in the other studied lacunar spinels. Instead, this results demonstrate that for these

polycrystalline samples the calculated ϵ_2 values give only an approximation of the intrinsic values and that in this case ϵ_2 is underestimated.

The summary of the basic results from the comparative phonon study is visualized in Fig. 5.14. It shows the phonon eigenfrequencies for each of the studied lacunar spinels at room temperature and at 10 K. The symbol area represents the oscillator strength $\Delta\epsilon$ of the phonon modes, which were obtained from fitting the experiential data with the Lorentz-oscillator model from Eq. 5.12. For visibility reasons, in the case of $AlMo_4S_8$ and $GaMo_4Se_8$, $\Delta\epsilon$ has been multiplied by a factor of 5 and 10, respectively. As discussed previously, the mode strengths obtained in the polycrystalline compounds are most likely underestimated.

At first the influence of the ligand ion shall be considered, as the shift of the phonons to lower frequencies when replacing S by Se is most obvious. For all sulfides the strongest phonon modes are located in the frequency range between 280 and 460 cm^{-1}, as indicated by the grey shaded area. In the case of the selenides the strongest phonons are found between 180 and 290 cm^{-1}. The shift of the eigenfrequencies is related to the different masses of S and Se and corresponds to the expected ratio of $\omega_{\mathrm{Se}}/\omega_{\mathrm{S}} = \sqrt{m_{\mathrm{S}}/m_{\mathrm{Se}}} = 0.64$. This is emphasized by the shaded area in Fig. 5.14, which is exactly scaled by this factor for the selenides. Thus, the ligands are strongly involved in the lattice vibrations.

Next, the impact of the exchange of the A-site ion on the phonon response is considered. For this purpose the sulfides hosting Ga and Al are compared. Despite the large mass difference of Ga and Al, no significant changes in the eigenfrequencies are found. However, a systematic effect on the relative spectral weight of the phonon modes is observed. In the room temperature spectra of the Ga-based compounds the strongest mode is typically found around 300 cm^{-1}. A second relatively strong, though somewhat weaker mode is observed in the frequency range between 350 and 380 cm^{-1} and a relatively weak modes is identified around 450 cm^{-1}. In the compounds hosting Al at the A position, the room-temperature FIR spectrum is dominated by two strong phonon modes located around 300 and 450 cm^{-1}. One further, comparatively weak mode is found in between the two dominating ones. These findings imply that the A-site atoms are involved in the observed IR-active phonon modes located around 350 - 380 cm^{-1} and 450 cm^{-1}.

The phonon spectrum seems to be much less affected by replacing the M-site ion. Both within the sulfides and the selenides no systematic changes in the eigenfrequency or the mode strength due to the replacement of the M site element can be discerned. Solely in $GaNb_4S_8$ the phonon frequencies are slightly lower than in the comparable compounds. However, this is not significant enough to connect the observed phonon modes with the transition metal site.

The fact that in the cubic phase only a limited subset of the six allowed zone-center F_2 modes is observed in the FIR measurements is in agreement with the assignment of these modes to vibrations of the atoms at the A-sites and the ligand

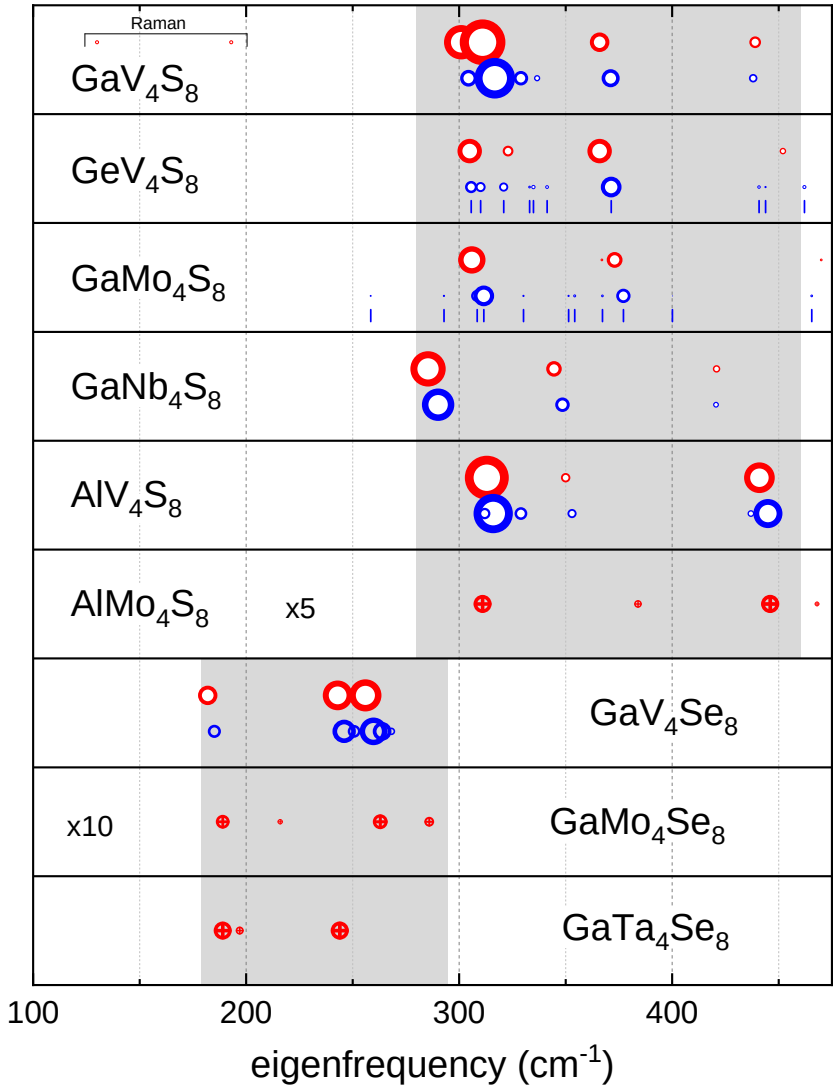

Figure 5.14.: Summary of the comparative phonon study on lacunar spinels [169]. For each compound the phonon eigenfrequency is shown at room temperature (red symbols) and at 10 K (blue symbols). The oscillator strength $\Delta\epsilon$ is represented by the area of the symbols. Grey shaded areas mark the frequency ranges within which the strongest phonon modes are found. For GaV_4S_8 the two F_2 modes reported from Raman spectroscopy [187] are also included. For better visibility, in the case of weak modes the frequencies are indicated by vertical lines. For the same reason, $\Delta\epsilon$ of $AlMo_4S_8$ and $GaMo_4Se_8$ has been multiplied by the given factors.

positions. For each of the studied compound either three or four phonon modes were found at room temperature. When going back to the symmetry analysis in Eq. 5.4, taking into account the IR-allowed F_2 phonon modes of the A-site and the two ligand sites X_1 and X_2 results in a total number of four modes after subtracting one acoustic F_2 mode. Thus, both the experimental results and

group theory considerations are in line with the assignment of the observed IR phonon modes to vibrations of the AX_4 tetrahedra and the ligand atoms within the cubane M_4X_4 clusters.

The detection of the two missing weak F_2 modes in GaV_4S_8 at frequencies of 130 and 193 cm^{-1} by Raman spectroscopy [187] and the overall systematic behavior of the phonon modes in lacunar spinels found in the present study suggest that also in the other compounds the missing modes may be located at the low frequency side of the observed modes.

Additional modes appearing below T_{JT} provide evidence for symmetry lowering at the structural transition, however, in the low-temperature Jahn-Teller distorted phase for all compounds also only a subset of the allowed phonon modes was detected. In contrast to the cubic phase, a direct comparison of the low-temperature phonon spectra of the studied lacunar spinels is difficult, as in the different compounds different crystal symmetries are realized below T_{JT}.

6. Systematics of electronic excitations in multiferroic lacunar spinels

In this chapter the results from broadband reflectivity spectroscopy on a series of lacunar spinels will be presented. The optical conductivity clearly illustrates the semiconducting behavior of these compounds over the whole studied temperature range. The size of band gap is obtained from the optical data and its temperature dependence will be discussed. The comparison of the different lacunar spinels allows to derive the systematics of the gap size when exchanging the atoms at the transition metal and the ligand site. The results of my work presented in the following chapter have been published in Ref. [169].

Figure 6.1 shows a semilogarithmic plot of the broadband reflectivity of single-crystalline GaV_4S_8, GeV_4S_8, GaV_4Se_8, $GaMo_4S_8$, $GaNb_4S_8$ and AlV_4S_8 in the frequency range between 150 and 20000 cm^{-1}. For each compound a spectrum of the room-temperature cubic phase (red curves) and the low-temperature Jahn-Teller distorted phase (blue curves) is shown. The spectra of the different lacunar spinels are qualitatively very similar. For frequencies below 600 cm^{-1} the phonons, which have been discussed in detail in section 5.2, are observed as sharp resonances. Depending on the compound, in the frequency range between 2000 and 6000 cm^{-1} a broadband feature is observed in the reflectivity spectrum, as indicated by the arrows in Fig. 6.1. While it is very broad and weak at room temperature, it gets clearly pronounced on decreasing the temperature. Not taking into account the details of the exact band structure, this feature can be associated with the electronic band gap. A further significant feature is exclusively observed in $GaMo_4S_8$ around 750 cm^{-1}, however, its origin uncertain at the moment.

For the analysis of the electronic band gap it is instructive to examine the optical conductivity spectrum. From the broadband reflectivity the optical conductivity σ is obtained via Kramers-Kronig transformation. For this purpose the experimental reflectivity spectrum was continued by a $\omega^{-1.5}$ extrapolation, which was followed by a ω^{-4} high-frequency extrapolation above $8 \cdot 10^5\,cm^{-1}$.

The frequency-dependent optical conductivity spectra of GaV_4S_8, GeV_4S_8, GaV_4Se_8, $GaMo_4S_8$, $GaNb_4S_8$ and AlV_4S_8 are shown in Fig. 6.2. For each compound the room-temperature broadband conductivity spectrum over the whole

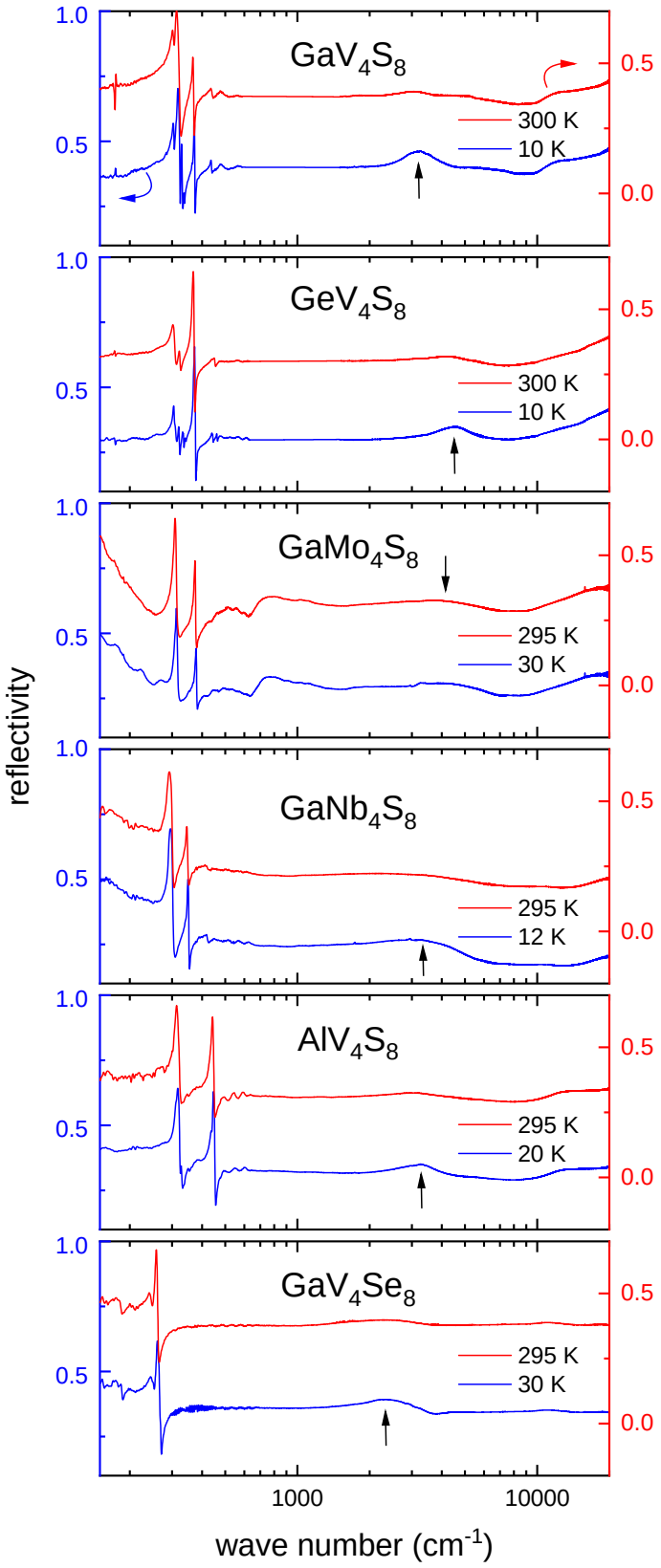

Figure 6.1: Frequency dependent reflectivity spectra of GaV_4S_8, GeV_4S_8, $GaMo_4S_8$, $GaNb_4S_8$, AlV_4S_8 and GaV_4Se_8 between 150 and 20000 cm^{-1}, measured in the low-temperature distorted phase (blue curves) and in the room temperature cubic phase (red curves) [169]. The marked broad, hump-like features in the frequency range between 2000 and 6000 cm^{-1} are associated with the band gap.

investigated spectral range is given in the right column, in the left column the conductivity is shown in the frequency range of the band gap up to 7000 cm^{-1} for selected temperatures. Irrespective of the temperature, the optical conductivity vanishes in the low-frequency limit. In agreement with resistivity measurements, this finding clearly classifies the lacunar spinels as semiconductors, not only in the low-temperature distorted phases, but also in the high-temperature cubic state. The band gap manifests itself as an increase of the optical conductivity in the frequency range between 2000 and 5000 cm^{-1}. In GaV_4S_8 this increase is most pronounced at the lowest temperatures with an almost step-like behavior at 2500 cm^{-1}. With increasing temperature the band edge gets continuously broadened and smeared out. We have primarily ascribed this temperature dependent behavior to orbital fluctuations in the high-temperature cubic phase [191]. A qualitatively similar behavior of the band edge is observed in GeV_4S_8, GaV_4Se_8, $GaNb_4S_8$ and $AlMo_4S_8$. Solely in $GaMo_4S_8$ no pronounced temperature dependence of the optical conductivity in the vicinity of the band gap was found. The broadband conductivity spectra at room temperature illustrate a further increasing behavior of σ above the band gap for all studied compounds.

Generally, the gap size E_g of semiconductors can be determined from a power-law behavior of the band edge $(\alpha\hbar\omega)^n \propto \hbar\omega - E_\mathrm{g}$ [192, 193]. Thereby the exponent n is determined by whether the electronic transition is direct or indirect, whether it is allowed or forbidden. The detailed analysis of the optical conductivity revealed that in the lacunar spinels this method is not strictly applicable. Besides, the partly very strong temperature dependent smearing out of the band edge suggests orbital fluctuations being involved. Therefore, the band gap E_g was instead determined by a linear extrapolation of the increase of the optical conductivity to zero. In Fig. 6.2 this is exemplarily indicated for the lowest and highest temperatures by the dashed lines. The temperature dependence of the band gap of the studied lacunar spinels is plotted in Fig. 6.3. It reveals band gap values in the range between 175 and 475 meV, in line with the classification of this compound family as narrow-gap semiconductors [107]. An overall increase of the gap size with decreasing temperature is observed, as commonly found in semiconductors [194, 195]. Table 6.1 summarizes the optically derived band gap E_g of the lacunar spinels for the lowest temperatures and at 300 K and in addition gives a comparison with literature values obtained from temperature dependent resistivity measurements.

In GaV_4S_8 a band gap of 260 meV is found at room temperature. This is in satisfactory agreement with the value of 240 meV obtained from resistivity measurements in Ref. [97]. On lowering the temperature, in the cubic phase the band gap increases and gets saturated below 100 K. At T_JT the gap increases by approximately 10 meV. A further increase of E_g is observed below T_JT with a slight anomaly at T_C. At 10 K the gap value reaches 330 meV in agreement with Ref. [196].

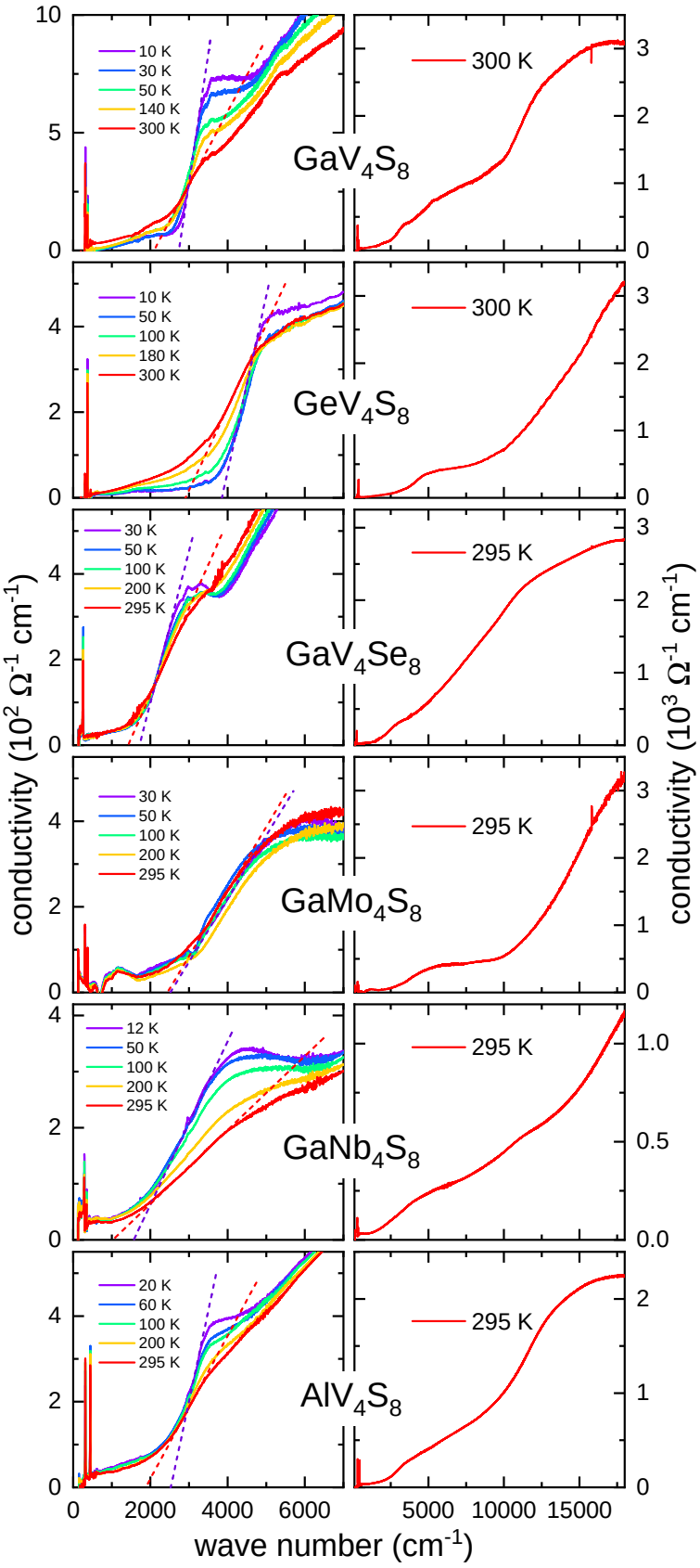

Figure 6.2: Frequency dependent optical conductivity of the studied lacunar spinels at selected temperatures in the region of the band gap [169]. Dashed lines show the linear extrapolation of σ for the determination of the gap energy. For room temperature the broadband optical conductivity is shown up to 18000 cm^{-1}.

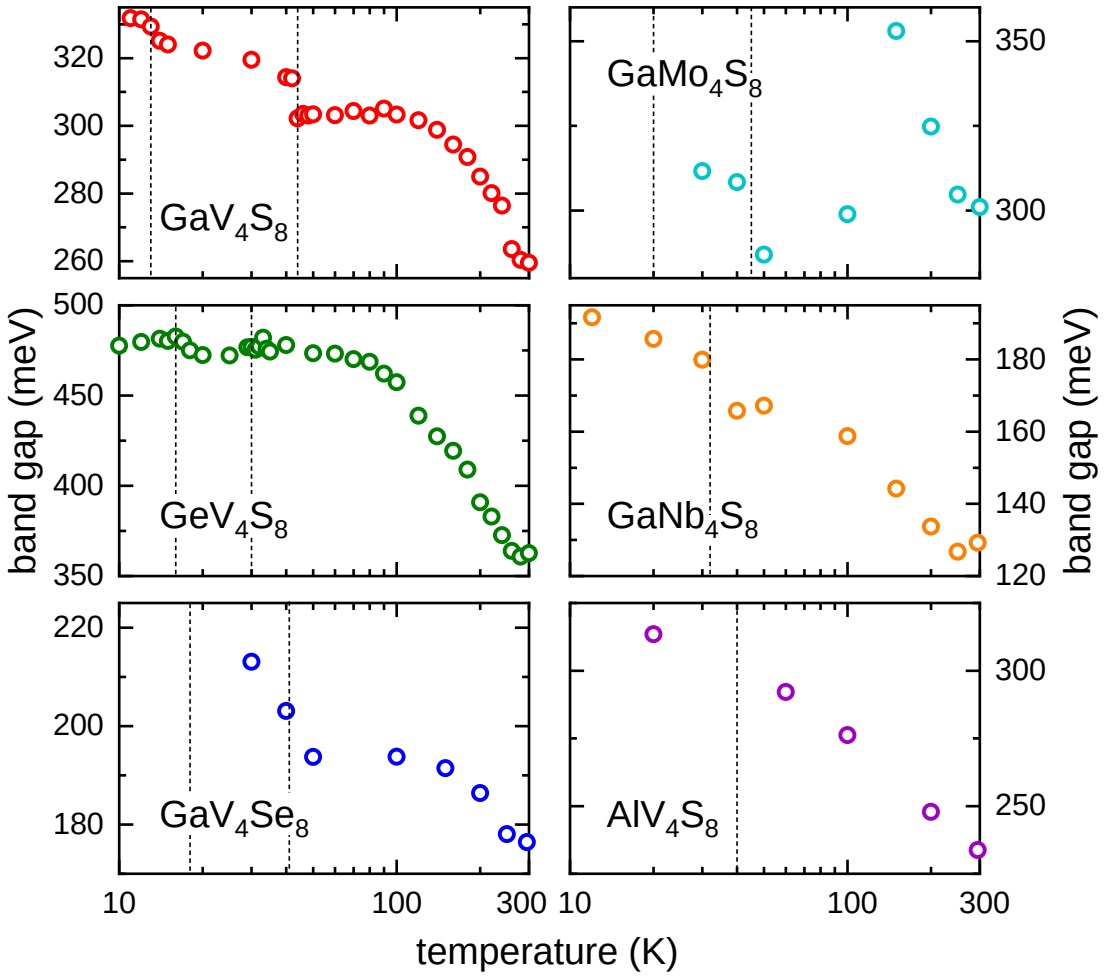

Figure 6.3.: Temperature dependence of the band gap of GaV_4S_8, GeV_4S_8, GaV_4Se_8, $GaMo_4S_8$, $GaNb_4S_8$ and AlV_4S_8, as determined from the linear extrapolation of the optical conductivity, in a semilogarithmic representation. The dashed vertical lines indicate the structural and magnetic phase transition temperatures.

For GeV_4S_8, GaV_4Se_8, $GaNb_4S_8$ and AlV_4S_8 a qualitatively similar behavior is observed. The band gap of GeV_4S_8 at room temperature is 350 meV, which is relatively close to the value of 300 meV from the electrical resistivity [98]. With slight anomalies both at T_{JT} and T_N the band gap of GeV_4S_8 increases up to 475 meV at 10 K. In GaV_4Se_8 the size of the gap is smaller and its temperature dependence is less pronounced. Nevertheless, also in this compound E_g experiences a blue shift from 175 meV at 300 K to 215 meV at the lowest measured temperature with an anomaly at T_{JT}. From resistivity measurements on GaV_4Se_8 a somewhat higher value of 270 meV was reported previously [72]. In $GaNb_4S_8$, where the temperature dependence of the optical conductivity is most pronounced, the lowest band gap energies have been observed. It increases from 130 meV at room temperature to 190 meV at 12 K. Again the temperature dependence of E_g exhibits an anomaly at the magnetostructural phase transition. For $GaNb_4S_8$ the difference between the band gap obtained from the optical measurements and the value of 280 meV from resistivity [74] is comparatively large. In the case of AlV_4S_8 a continuous increase of the band gap is observed on decreasing the temperature. Gap energies of 230 meV at room temperature and 310 meV at 20 K have been found. From the experimental data no anomaly of E_g at the structural phase transition can be resolved.

Only for $GaMo_4S_8$ no clear trend in the temperature dependence of the band gap energy can be discerned. In this case, the values of E_g show large scattering. Within the experimental error the band gap adopts a mean value of approximately 300 meV in the investigated temperature range.

In general, the observed relative change of the band gap energy at the structural phase transition does not exceed 5 % in the lacunar spinels under investigation. The occurrence of anomalies in the temperature dependence of E_g at the structural phase transition, with the band gap of GaV_4S_8, GaV_4Se_8 and $GaNb_4S_8$ being sightly enhanced below T_{JT}, emphasizes the influence of structural distortions on the electronic structure of the lacunar spinels, as previously discussed in theoretical studies [117, 119]. However, as the changes of the band gap are small compared to its absolute value, the influence of structural distortions on the electronic structure can be considered small.

As evident from Tab. 6.1, the band gap energies determined from temperature-dependent resistivity measurements are mostly in reasonable agreement with those obtained from the optical experiments. The determination of E_g from the electrical resistivity relies on the assumption of a thermally activated Arrhenius-like behavior and does not consider the observed temperature dependence of E_g. It has been shown that a purely thermally activated behavior cannot be generally assumed in lacunar spinels for all temperatures [97]. Therefore, due to deviations from the Arrhenius behavior the determined value of the band gap can depend on the chosen temperature range, which may explain the discrepancies between some of the

Table 6.1.: Summary of the band gap energies E_g of the studied lacunar spinels determined from the optical conductivity spectra at low temperatures and at 300 K. Values obtained from temperature dependent resistivity measurements are included for comparison. The values without reference have been determined in the course of this work.

	E_g (meV) from optical conductivity		E_g (meV) from resistivity	
	low T	300 K		
GaV_4S_8	330 (10 K)	260	240	[97]
			330	[196]
GeV_4S_8	475 (10 K)	350	300	[98]
AlV_4S_8	310 (20 K)	230		
$GaMo_4S_8$	300 (30 K)	300		
$GaNb_4S_8$	190 (12 K)	130	280	[74]
GaV_4Se_8	215 (30 K)	175	270	[72]
$GaNb_4Se_8$			190	[74]
			280	[196]
$GaTa_4Se_8$		120 [196]	160	[74]
			240	[197]

literature values in Tab. 6.1. The linear extrapolation of the optical conductivity represents a more reliable method for the determination of the band gap in lacunar spinels. Therefore, for the analysis of the systematics of E_g over the series of investigated compounds the values obtained from the optical conductivity were used as far as possible.

When replacing S by Se at the ligand site, the size of the band gap is reduced when comparing the optically derived E_g of GaV_4S_8 and GaV_4Se_8. Similarly, a clear reduction of the band gap is observed when comparing the values of $GaNb_4S_8$ and $GaNb_4Se_8$ obtained from the resistivity measurements in Ref. [74]. Furthermore, in Ref. [196] the band gap has been investigated for the substitution series of $GaTa_4Se_{8-x}Te_x$ for $0 \leq x \leq 6.5$. Although the authors of Ref. [196] do not present data for pure $GaTa_4Te_8$, towards higher Te concentrations a clearly decreasing tendency of the band gap can be observed. Thus, these findings suggest a general decrease of the gap energy in lacunar spinels when exchanging the ligand atom within the series S $\rightarrow$ Se $\rightarrow$ Te. This decreasing tendency of E_g can most probably be explained by the increasing bandwidth of the cluster orbitals in the selenides and tellurides.

When exchanging the elements at the transition metal site, the following observations can be made: Replacing the $3d$ element V by the $4d$ element Nb leads to a clear reduction of the bad gap, as can be seen by the comparison of GaV_4S_8 and $GaNb_4S_8$. Similarly, also a reduction of E_g is discerned when replacing V by Mo, when comparing the low-temperature gap of GaV_4S_8 and $GaMo_4S_8$. The replacement of the transition metal site with the $5d$ element Ta also results in a reduced band gap, as can be observed by comparison of GaV_4Se_8 and $GaTa_4Se_8$. When considering the gap energies obtained for $GaNb_4Se_8$ and $GaTa_4Se_8$ from the resistivity measurements of Ref. [74], a similar reduction of E_g can be found when replacing Nb by Ta. These results indicate a decreasing trend of the bad gap when going from $3d$ to $4d$ and $5d$ elements, suggesting a weakening of the correlations within the series $3d \rightarrow 4d \rightarrow 5d$.

Figure 6.4 shows the temperature dependence of the spectral weight transfer of GaV_4S_8, GeV_4S_8, GaV_4Se_8, $GaNb_4S_8$ and AlV_4S_8 relative to 100 K. It has been determined by integration the optical conductivity spectra up to 6000 cm^{-1}, so that the frequency range of the band gap is covered. Generally, the area under the conductivity spectrum is a measure of the electronic density [144]. Thus, the analysis of the spectral weight transfer gives insight into changes of the electronic structure and shifts of spectral weight from or towards higher energies. The data shown in Fig. 6.4 reveal only a weak temperature dependence of the spectral weight transfer up to 100 K, which is in the order of magnitude of 10 %. Weak anomalies at the structural phase transition can be observed in GaV_4S_8, GeV_4S_8 and $GaNb_4S_8$, which, however, do not exceed 10 %. This again indicates a weak influence of the structural transition on the electronic structure of the lacunar spinels, which is in line with the temperature dependent analysis of the band gap shown in Fig. 6.3.

In conclusion, all studied lacunar spinels are characterized as narrow-gap semiconductors with gap sizes ranging from 130 to 400 meV. This holds not only for the low-temperature distorted phase, but also for the high-temperature cubic phase, a fact that is usually uncaptured by ab initio studies. Indeed, the temperature dependence of the gap energy and of the spectral weight suggests that the electronic structure is only weakly influenced by the structural transition. The systematic study and comparison of a broad series of lacunar spinel compounds reveals a decrease of the gap size when changing the ligand from S to Se, as well as when replacing $3d$ ions with $4d$ and $5d$ ions at the transition metal site.

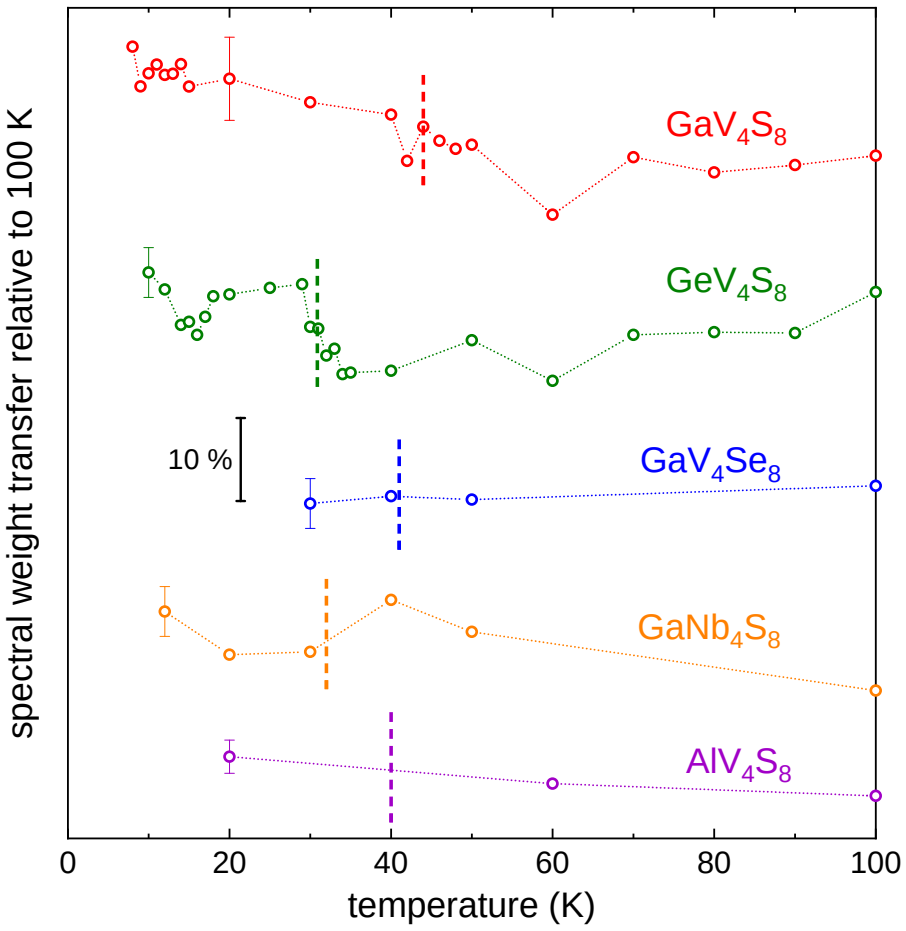

Figure 6.4.: Temperature dependence of the spectral weight of GaV_4S_8, GeV_4S_8, GaV_4Se_8, $GaNb_4S_8$ and AlV_4S_8 relative to 100 K [169]. The spectral weight has been determined by integration of the optical conductivity up to 6000 cm^{-1}. For better visibility the curves are shifted with respect to each other. The scale bar denotes the relative change. Dashed vertical lines indicate the structural phase transition temperature.

7. Summary

In the course of this work the optical properties of two compound families of multiferroics were studied in detail, namely the transition metal molybdenum oxides $M_2Mo_3O_8$ (M = Co, Fe, Zn) and a wide series of lacunar spinels AM_4X_8 (A = Ga, Ge, Al; M = V, Mo, Nb, Ta; X = S, Se). By means of optical spectroscopy, a broad energy range from THz frequencies over the FIR, MIR and NIR up to the visible range has been covered, that allowed the probing of spin, lattice, orbital and charge degrees of freedom in these multiferroic compounds. The main results obtained on the different degrees of freedom are summarized in the following.

The THz spectroscopy measurements in the magnetically ordered phase of $Co_2Mo_3O_8$ reveal complex magnon spectra, far richer than expected for the proposed four-sublattice collinear antiferromagnetic structure. While as a rule of thumb the number of precessional magnon modes should be equal to the number of magnetic sublattices, in the antiferromagnetic state of $Co_2Mo_3O_8$ 14 excitations emerge already in zero magnetic field. Inelastic neutron scattering measurements confirm the four-sublattice magnetic structure and, as expected, reveal two magnon branches in zero field, which are in agreement with the two strongest modes observed by THz spectroscopy. The magnetic field dependent optical measurements with $H \parallel c$ also support the easy-axis nature of $Co_2Mo_3O_8$. Thus, concerning the unexpected large number of modes in $Co_2Mo_3O_8$, beyond the scope of linear spin-wave theory, the possibility of transitions with $\Delta S > 1$ is discussed and an interpretation in terms of low-lying electronic transitions is considered. Moreover, modes may be identified as spin-stretching modes with an oscillating spin length. Along this line the optical measurements may provide the experimental basis for future theoretical studies.

Polarization dependent measurements reveal the selection rules of the modes. Besides the conventional magnetic dipole active magnon modes, purely electric dipole active electromagnons, and both magnetic and electric dipole active magnetoelectric resonances are found in $Co_2Mo_3O_8$. The dynamical magnetoelectric effect was studied via the investigation of unidirectional transmission. Strong directional dichroism is observed for some of the magnetoelectric resonances in $Co_2Mo_3O_8$. In the case of directional dichroism, the absorption strength is related to the trilinear product $\boldsymbol{k} \cdot (\boldsymbol{P} \times \boldsymbol{M})$. Within the course of this work, for the first time this relation has been proven experimentally by independent switching of the sign of $\boldsymbol{k}$, $\boldsymbol{P}$ and $\boldsymbol{M}$.

In a next step, the THz spectroscopy data obtained on $Co_2Mo_3O_8$ are compared to those of $Fe_2Mo_3O_8$ and $Fe_{1.86}Zn_{0.14}Mo_3O_8$. Similarly, the magnetic field dependent measurements support the easy-axis character of the magnetically ordered phase, although again the magnon spectra are more complex than expected from linear spin-wave theory. Distinct from $Co_2Mo_3O_8$ and $Fe_2Mo_3O_8$, in the $Fe_{1.86}Zn_{0.14}Mo_3O_8$ spectra a vibronic excitation was identified.

$Fe_2Mo_3O_8$ and especially $Fe_{1.86}Zn_{0.14}Mo_3O_8$, with their comparatively low critical fields, allow to study the antiferromagnetic-to-ferrimagnetic phase transition under magnetic fields $H \parallel c$. As found by magnetization measurements, in $Fe_{1.86}Zn_{0.14}Mo_3O_8$ this transition happens via a two-step process with two critical fields H_{c1} and H_{c2}. In this case, the field-dependent THz measurements reveal a phase coexistence for $H_{c1} < H < H_{c2}$.

Pure $Fe_2Mo_3O_8$ has also been investigated at higher energies in the IR range. So far the structure of $Fe_2Mo_3O_8$ below T_N has still been under debate [60]. The phonon study of $Fe_2Mo_3O_8$ was further motivated by recent neutron diffraction data, which revealed short-range magnetic ordering in below 200 K, showing up via an anomalous temperature dependence of the lattice parameter c. In line with the latest low-temperature diffraction data, the FIR spectra exhibit no signature of a symmetry lowering below T_N. The short-range ordering is reflected in the optical data in the temperature dependence of some excitations and in the occurrence of additional spectral features below 200 K, which are presumably of combined vibrational and electronic origin. Furthermore, the E_1 phonon modes show an anomalous nonmonotonic temperature dependence with a significantly increased phonon lifetime in the antiferromagnetically ordered phase. In this case, orbital degrees of freedom play a key role, with fluctuations of the direction of the orbital moment on the tetrahedral Fe^{2+} sites getting quenched below T_N. Besides the FIR excitations, the *d-d* transitions of tetrahedrally coordinated Fe^{2+} were identified in the MIR, with their finestructure reflecting the same energy scale as the vibronic excitation observed in the Zn-doped $Fe_{1.86}Zn_{0.14}Mo_3O_8$.

A broad series of lacunar spinels AM_4X_8 has been studied in detail in the FIR range to investigate the systematics of the phonon modes by sequential replacement of the different atomic sites. The successive replacement of the elements at the A-site, the transition metal M and the ligand site X allows to assign the observed modes in the cubic phase to the different structural units. While the phonon eigenfrequencies are strongly affected by the ligand, the A-site atoms influence the relative spectral weight of the modes. Exchanging the M-site element has negligible effect on the spectra. Thus, the strongest phonon modes of the lacunar spinels are ascribed to vibrations of the A-site and the ligand site atoms. Temperature dependent measurements allow to trace the Jahn-Teller driven symmetry lowering transition via the occurrence of additional modes below T_{JT}, however, in each case only a subset of the zone-center IR allowed phonons was visible.

The performed broadband reflectivity measurements on lacunar spinels up to the visible range allow to study the systematics of the electronic band gap of these semiconducting compounds. The gap is already open in the cubic state, which is a feature commonly uncaptured by ab initio studies. The lacunar spinels can be classified as narrow-gap semiconductors with a gap size between 130 and 400 meV, which is only weakly influenced by the structural transition. Comparing the different compounds, the gap size gets reduced within the series of transition metal sites from $3d$ to $4d$ and $5d$ elements, as well as when changing the ligand from S by Se. Despite recently reported promising approaches, reproducing the semiconducting behavior of the lacunar spinels is still a challenge for theory. Thus, these results from optical spectroscopy may provide a solid experimental basis for future theoretical studies.

A. Appendix

A.1. Simulation of the vibronic excitation in $Fe_{1.86}Zn_{0.14}Mo_3O_8$

In the following the basic aspects of the simulation of the vibronic excitation in $Fe_{1.86}Zn_{0.14}Mo_3O_8$ by Benjamin Csizi will be elucidated, as published in Ref. [57].

Following the approach of Refs. [198, 199], in the case of linear electron-phonon coupling the normalized absorption spectrum at $T = 0$ is given by

$$I(\omega) = \int_{-\infty}^{\infty} f(t) e^{i\omega t} \, \mathrm{d}t, \tag{A.1}$$

where $f(t)$ is the generating function

$$f(t) = e^{-i\omega_0 t - S(t=0) + S(t)}, \tag{A.2}$$

with ω_0 being the frequency of the zero-phonon line. $S(t)$ is given by

$$S(t) = \int_{0}^{\infty} s(\omega) e^{-i\omega t} \, \mathrm{d}\omega, \tag{A.3}$$

where $s(\omega)$ is the coupling function. For the simulation the following empirical coupling function by Rätsep et al. [200] was used:

$$s(\omega) = \exp\left(-\frac{\omega}{\omega_1}\right) \frac{\omega^2 S_1}{2\omega_1^3} + \exp\left(-\frac{\omega}{\omega_2}\right) \frac{\omega^3 S_2}{6\omega_2^4} \tag{A.4}$$

The generating function $f(t)$ can be written in an expansion in $S(t)$. From this it follows for $I(\omega)$:

$$I(\omega) = e^{-S} \sum_{n=0}^{\infty} \frac{S^n}{n!} \Gamma_n(\omega) \tag{A.5}$$

The parameter n corresponds to the number of phonons taking part in the vibronic absorption process. $\Gamma_n(\omega)$ is given by

$$\Gamma_n(\omega) = \int_{-\infty}^{\infty} e^{i(\omega-\omega_0)t} \left[\frac{S(t)}{S}\right]^n \mathrm{d}t, \tag{A.6}$$

which for $n > 1$ can be calculated iteratively according to

$$\Gamma_n(\omega) = \int_{-\infty}^{\infty} \Gamma_{n-1}(\omega')\Gamma_1(\omega + \omega_0 - \omega')\,\mathrm{d}\omega'. \tag{A.7}$$

Finally, the normalized absorption spectrum $I(\omega)$ is related to the experimental absorption spectrum $\alpha(\omega)$ by a scaling amplitude A:

$$\alpha(\omega) = A \cdot I(\omega) \tag{A.8}$$

The simulation of the broad vibronic absorption band in $Fe_{1.86}Zn_{0.14}Mo_3O_8$ uses $n = 3$ phonons and the following parameters: $\omega_0 = 12\,\mathrm{cm}^{-1}$, $S_1 = 0.02$, $S_2 = 1.1$, $\omega_1 = 12\,\mathrm{cm}^{-1}$, $\omega_2 = 3.6\,\mathrm{cm}^{-1}$ and $A = 2.4 \cdot 10^3\,\mathrm{cm}^{-1}$.

A.2. Neutron and x-ray diffraction on $Fe_2Mo_3O_8$

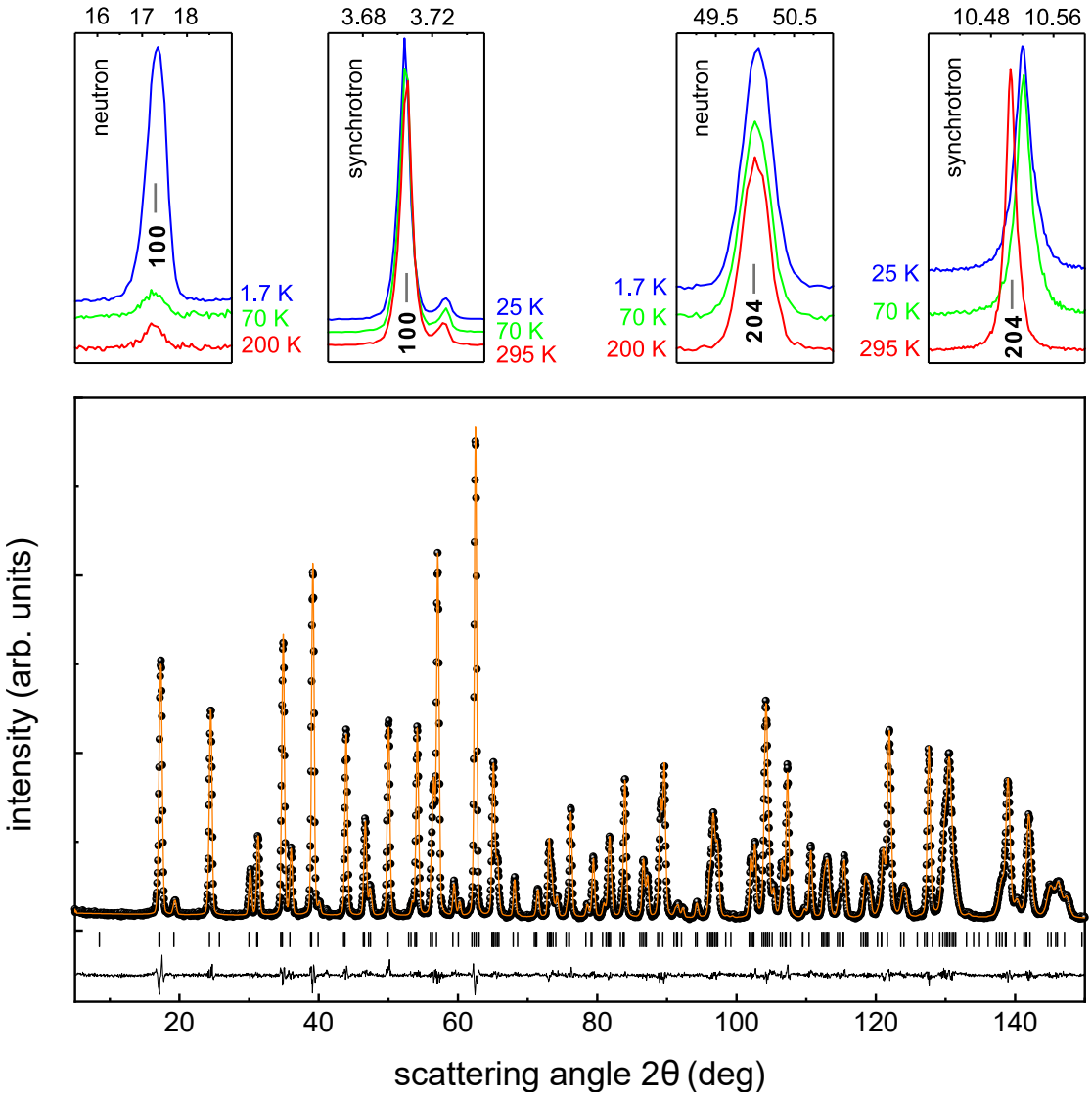

Figure A.1.: Top frames: Temperature evolution of the 100 and 204 reflections from high-resolution synchrotron and neutron measurements. Bottom frame: Neutron diffraction data at 1.7 K and corresponding Rietveld refinement using the $P6_3mc$ symmetry. The ticks mark the peak positions, the black line at the bottom shows the corresponding difference pattern. The measurements were performed by Dr. Alexander Tsirlin and Dr. Nazir Khan at the Swiss Neutron Source (SINQ) at the Paul Scherrer Institute (Villigen, Switzerland) and at the MSPD synchrotron beamline of ALBA (Barcelona, Spain).

A.3. Phonon frequencies of $Fe_2Mo_3O_8$ from DFT

Table A.1.: Phonon frequencies (in cm^{-1}) calculated by Dr. Alexander Tsirlin by DFT+U+SO for 1.7 and 275 K. Calculations were performed for ferromagnetic (fm) and antiferromagnetic (afm) order as well as for a uncorrelated non-magnetic state (nonmag).

$T = 1.7\,K$			$T = 275\,K$		$T = 1.7\,K$			$T = 275\,K$	
nonmag	fm	afm	fm	afm	nonmag	fm	afm	fm	afm
A_1					B_1				
724	792	787	789	784	739	824	815	821	812
694	733	734	730	730	707	739	738	736	734
547	653	651	653	651	540	650	647	648	648
461	568	558	565	563	483	594	586	593	591
423	456	454	455	452	427	491	481	492	483
387	453	444	453	447	377	450	449	448	446
275	363	365	363	365	290	356	363	355	362
236	267	262	267	264	212	251	253	251	253
154	207	201	207	203	167	212	208	213	212
					132	156	155	155	154
A_2					B_2				
486	438	434	437	435	483	431	427	428	428
450	405	403	405	402	461	416	413	417	412
138	139	141	139	142	141	141	143	141	144
E_1					E_2				
691	744	750	742	745	690	748	751	745	747
558	570	577	567	570	560	565	572	562	564
522	520	522	518	520	517	525	525	522	524
490	482	481	482	480	489	481	482	480	479
449	471	473	467	467	460	469	472	458	467
437	450	455	450	448	420	453	453	454	447
307	347	351	346	351	302	353	359	351	357
295	318	312	319	313	288	333	334	334	334
221	273	286	274	282	222	262	277	262	274
195	219	223	218	222	191	211	215	210	212
163	186	191	187	189	167	184	191	184	191
146	157	162	157	159	142	145	147	145	145
					44	68	77	66	71

A.4. Alternative level scheme for tetrahedral Fe^{2+} in $Fe_2Mo_3O_8$

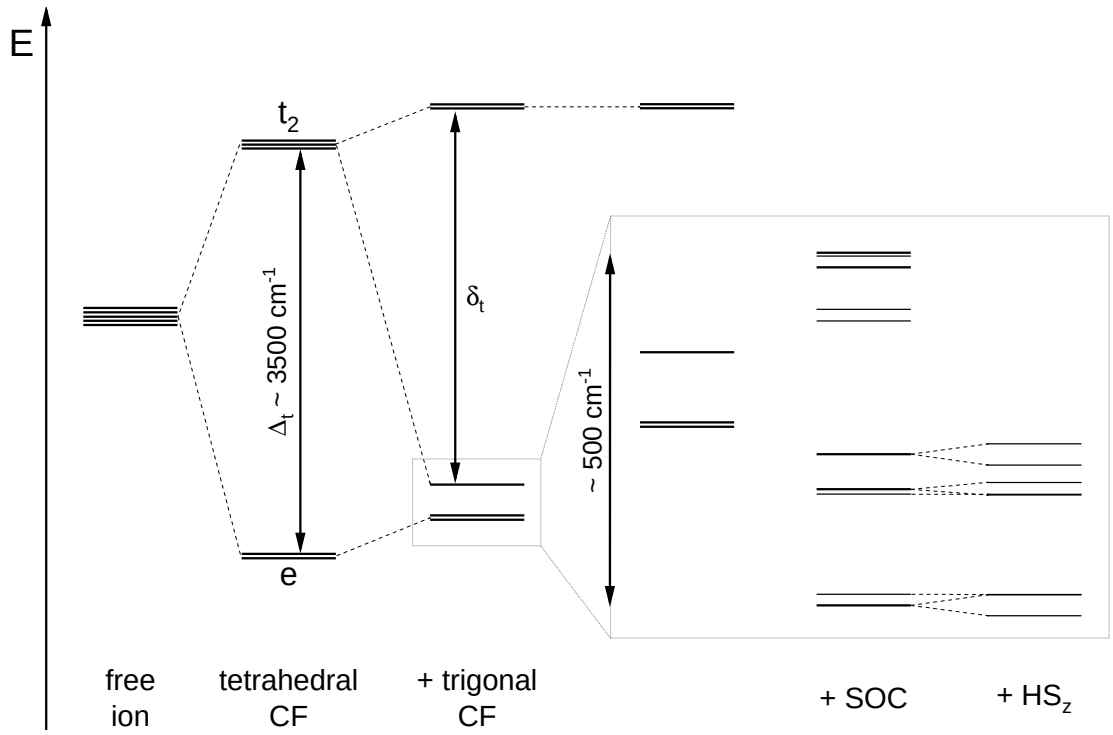

Figure A.2.: Alternative crystal-field level scheme of tetrahedral Fe^{2+} adapted from Ref. [44].

Bibliography

[1] H. Schmid. *Multi-ferroic magnetoelectrics.* Ferroelectrics **162**, 317 (1994)

[2] N. A. Spaldin and M. Fiebig. *The renaissance of magnetoelectric multiferroics.* Science **309**, 391 (2005)

[3] L. W. Martin, S. P. Crane, Y.-H. Chu, M. B. Holcomb, M. Gajek, M. Huijben, C.-H. Yang, N. Balke and R. Ramesh. *Multiferroics and magnetoelectrics: Thin films and nanostructures.* J. Phys.: Condens. Matter **20**, 434220 (2008)

[4] N. A. Spaldin, S.-W. Cheong and R. Ramesh. *Multiferroics: Past, present, and future.* Phys. Today **63**, 38 (2010)

[5] M. Fiebig, T. Lottermoser, D. Meier and M. Trassin. *The evolution of multiferroics.* Nat. Rev. **1**, 16046 (2016)

[6] N. A. Spaldin and R. Ramesh. *Advances in magnetoelectric multiferroics.* Nat. Mater. **18**, 203 (2019)

[7] Y. Wang, G. L. Pascut, B. Gao, T. A. Tyson, K. Haule, V. Kiryukhin and S.-W. Cheong. *Unveiling hidden ferrimagnetism and giant magnetoelectricity in polar magnet* $Fe_2Mo_3O_8$. Sci. Rep. **5**, 12268 (2015)

[8] M. Fiebig. *Revival of the magnetoelectric effect.* J. Phys. D: Appl. Phys. **38**, R123 (2005)

[9] D. B. Litvin. *Ferroic classifications extended to ferrotoroidic crystals.* Acta. Cryst. A **64**, 316 (2008)

[10] D. Khomskii. *Classifying multiferroics: Mechanisms and effects.* Physics **2**, 20 (2009)

[11] P. Curie. *Sur la symétrie dans les phénomènes physiques, symétrie d'un champ électrique et d'un champ magnétique.* J. Phys. Theor. Appl. **3**, 393 (1894)

[12] C.-W. Nan, M. I. Bichurin, S. Dong, D. Viehland and G. Srinivasan. *Multiferroic magnetoelectric composites: Historical perspective, status, and future directions.* J. Appl. Phys. **103**, 031101 (2008)

[13] W. Eerenstein, N. D. Mathur and J. F. Scott. *Multiferroic and magnetoelectric materials.* Nature **442**, 759 (2006)

[14] K. F. Wang, J.-M. Liu and Z. F. Ren. *Multiferroicity: The coupling between magnetic and polarization orders.* Adv. Phys. **58**, 321 (2009)

[15] K. Siratori, K. Kohn and E. Kita. *Magnetoelectric effect in magnetic materials.* Acta Phys. Pol. A **81**, 431 (1992)

[16] W. F. Brown jr., R. M. Hornreich and S. Shtrikman. *Upper bound on the magnetoelectric susceptibility.* Phys. Rev. **168**, 574 (1968)

[17] N. A. Spaldin, M. Fiebig and M. Mostovoy. *The toroidal moment in condensed-matter physics and its relation to the magnetoelectric effect.* J. Phys.: Condens. Matter **20**, 434203 (2008)

[18] R. Kubo. *Statistical-mechanical theory of irreversible processes. I.* J. Phys. Soc. Jpn. **12**, 570 (1957)

[19] R. Kubo, M. Toda and N. Hashitsume. *Statistical physics II: Nonequilibrium statistical mechanics.* Springer-Verlag Berlin Heidelberg, 2. edition (1991)

[20] I. Kézsmárki, D. Szaller, S. Bordács, V. Kocsis, Y. Tokunaga, Y. Taguchi, H. Murakawa, Y. Tokura, H. Engelkamp, T. Rõõm and U. Nagel. *One-way transparency of four-coloured spin-wave excitations in multiferroic materials.* Nat. Commun. **5**, 3203 (2014)

[21] I. Kézsmárki, N. Kida, H. Murakawa, S. Bordács, Y. Onose and Y. Tokura. *Enhanced directional dichroism of terahertz light in resonance with magnetic excitations of the multiferroic $Ba_2CoGe_2O_7$ oxide compound.* Phys. Rev. Lett. **106**, 057403 (2011)

[22] Y. Tokura and N. Nagaosa. *Nonreciprocal responses from noncentrosymmetric quantum materials.* Nat. Commun. **9**, 3740 (2018)

[23] M. Saito, K. Ishikawa, K. Taniguchi and T. Arima. *Magnetic control of crystal chirality and the existence of a large magneto-optical dichroism effect in CuB_2O_4.* Phys. Rev. Lett. **101**, 117402 (2008)

[24] M. Saito, K. Taniguchi and T. Arima. *Gigantic optical magnetoelectric effect in CuB_2O_4.* J. Phys. Soc. Jpn. **77**, 013705 (2008)

[25] M. Saito, K. Ishikawa, S. Konno, K. Taniguchi and T. Arima. *Periodic rotation of magnetization in a non-centrosymmetric soft magnet induced by an electric field.* Nat. Mater. **8**, 634 (2009)

[26] S. Bordács, I. Kézsmárki, D. Szaller, L. Demkó, N. Kida, H. Murakawa, Y. Onose, R. Shimano, T. Rõõm, U. Nagel, S. Miyahara, N. Furukawa and Y. Tokura. *Chirality of matter shows up via spin excitations.* Nat. Phys. **8**, 734 (2012)

[27] Y. Takahashi, R. Shimano, Y. Kaneko, H. Murakawa and Y. Tokura. *Magnetoelectric resonance with electromagnons in a perovskite helimagnet.* Nat. Phys. **8**, 121 (2010)

[28] Y. Takahashi, Y. Yamasaki and Y. Tokura. *Terahertz magnetoelectric resonance enhanced by mutual coupling of electromagnons.* Phys. Rev. Lett. **111**, 037204 (2013)

[29] S. Bordács, V. Kocsis, Y. Tokunaga, U. Nagel, T. Rõõm, Y. Takahashi, Y. Taguchi and Y. Tokura. *Unidirectional terahertz light absorption in the pyroelectric ferrimagnet $CaBaCo_4O_7$.* Phys. Rev. B **92**, 214441 (2015)

[30] I. Kézsmárki, U. Nagel, S. Bordács, R. S. Fishman, J. H. Lee, H. T. Yi, S.-W. Cheong and T. Rõõm. *Optical diode effect at spin-wave excitations of the room-temperature multiferroic $BiFeO_3$.* Phys. Rev. Lett. **115**, 127203 (2015)

[31] S. Yu, B. Gao, J. W. Kim, S.-W. Cheong, M. K. L. Man, J. Madéo, K. M. Dani and D. Talbayev. *High-temperature terahertz optical diode effect without magnetic order in polar $FeZnMo_3O_8$.* Phys. Rev. Lett. **120**, 037601 (2018)

[32] Y. Okamura, S. Seki, S. Bordács, Á. Butykai, V. Tsurkan, I. Kézsmárki and Y. Tokura. *Microwave directional dichroism resonant with spin excitations in the polar ferromagnet GaV_4S_8.* Phys. Rev. Lett. **122**, 057202 (2019)

[33] J. H. Jung, M. Matsubara, T. Arima, J. P. He, Y. Kaneko and Y. Tokura. *Optical magnetoelectric effect in the polar $GaFeO_3$ ferrimagnet.* Phys. Rev. Lett. **93**, 037403 (2004)

[34] M. Kubota, T. Arima, Y. Kaneko, J. P. He, X. Z. Yu and Y. Tokura. *X-Ray directional dichroism of a polar ferrimagnet.* Phys. Rev. Lett. **92**, 137401 (2004)

[35] T. Arima. *Magneto-electric optics in non-centrosymmetric ferromagnets.* J. Phys.: Condens. Matter **20**, 434211 (2008)

[36] G. L. J. A. Rikken, C. Strohm and P. Wyder. *Observation of magnetoelectric directional anisotropy.* Phys. Rev. Lett. **89**, 133005 (2002)

[37] S. Miyahara and N. Furukawa. *Theory of magnetoelectric resonance in two-dimensional $S = 3/2$ antiferromagnet $Ba_2CoGe_2O_7$ via spin-dependent metal-ligand hybridization mechanism.* J. Phys. Soc. Jpn. **80**, 073708 (2011)

[38] S. Miyahara and N. Furukawa. *Nonreciprocal directional dichroism and toroidalmagnons in helical magnets.* J. Phys. Soc. Jpn. **81**, 023712 (2012)

[39] Y. Tokura. *Multiferroics - toward strong coupling between magnetization and polarization in a solid.* J. Magn. Magn. Mater. **310**, 1145 (2007)

[40] C. Ederer and N. A. Spaldin. *Towards a microscopic theory of toroidal moments in bulk periodic crystals.* Phys. Rev. B **76**, 214404 (2007)

[41] D. Szaller, S. Bordács and I. Kézsmárki. *Symmetry conditions for nonreciprocal light propagation in magnetic crystals.* Phys. Rev. B **87**, 014421 (2013)

[42] F. E. Neumann. *Vorlesungen über die Theorie der Elastizität der festen Körper und des Lichtäthers.* edited by O. E. Meyer, B. G. Teubner-Verlag, Leipzig (1885)

[43] W. H. McCarroll, L. Katz and R. Ward. *Some ternary oxides of tetravalent molybdenum.* J. Am. Chem. Soc. **79**, 5410 (1957)

[44] F. Varret, H. Czeskleba, F. Hartmann-Boutron and P. Imbert. *Étude par effet Mössbauer de l'ion Fe^{2+} en symétrie trigonale dans les composés du type (Fe, M)$_2Mo_3O_8$ (M = Mg, Zn, Mn, Co, Ni) et propriétés magnétiques de (Fe, Zn)$_2Mo_3O_8$.* J. Phys. **33**, 549 (1972)

[45] D. Bertrand and H. Kerner-Czeskleba. *Étude structurale et magnétique de molybdates d'éléments de transition.* J. Phys. **36**, 379 (1975)

[46] Y. Le Page and P. Strobel. *Structure of iron(II) molybdenum(IV) oxide $Fe_2Mo_3O_8$.* Acta Cryst. B **38**, 1265 (1982)

[47] P. Strobel, Y. Le Page and S. P. McAlister. *Growth and physical properties of single crystals of $Fe^{II}_2Mo^{IV}_3O_8$.* J. Solid State Chem. **42**, 242 (1982)

[48] S. P. McAlister and P. Strobel. *Magnetic order in $M_2Mo_3O_8$ single crystals (M = Mn, Fe, Co, Ni).* J. Magn. Magn. Mater. **30**, 340 (1983)

[49] H. Abe, A. Sato, N. Tsujii, T. Furubayashi and M. Shimoda. *Structural refinement of $T_2Mo_3O_8$ (T = Mg, Co, Zn and Mn) and anomalous valence of trinuclear molybdenum clusters in $Mn_2Mo_3O_8$.* J. Solid State Chem. **183**, 379 (2010)

[50] T. Kurumaji, S. Ishiwata and Y. Tokura. *Doping-tunable ferrimagnetic phase with large linear magnetoelectric effect in a polar magnet $Fe_2Mo_3O_8$.* Phys. Rev. X **5**, 031034 (2015)

[51] Y. S. Tang, S. M. Wang, L. Lin, C. Li, S. H. Zheng, C. F. Li, J. H. Zhang, Z. B. Yan, X. P. Jiang and J.-M. Liu. *Collinear magnetic structure and multiferroicity in the polar magnet $Co_2Mo_3O_8$.* Phys. Rev. B **100**, 134112 (2019)

[52] F. A. Cotton. *Metal atom clusters in oxide systems.* Inorg. Chem. **3**, 1217 (1964)

[53] T. Kurumaji, S. Ishiwata and Y. Tokura. *Diagonal magnetoelectric susceptibility and effect of Fe doping in the polar ferrimagnet $Mn_2Mo_3O_8$.* Phys. Rev. B **95**, 045142 (2017)

[54] S. V. Streltsov, D.-J. Huang, I. V. Solovyev and D. I. Khomskii. *Ordering of Fe and Zn ions and the magnetic properties of $FeZnMo_3O_8$.* JETP Lett. **109**, 786 (2019)

[55] I. V. Solovyev and S. V. Streltsov. *Microscopic toy model for magnetoelectric effect in polar $Fe_2Mo_3O_8$.* Phys. Rev. Mater. **3**, 114402 (2019)

[56] S. Nakayama, R. Nakamura, M. Akaki, D. Akahoshi and H. Kuwahara. *Ferromagnetic behavior of $(Fe_{1-y}Zn_y)_2Mo_3O_8$ ($0 \leq y \leq 1$) induced by nonmagnetic Zn substitution.* J. Phys. Soc. Jpn. **80**, 104706 (2011)

[57] B. Csizi, S. Reschke, A. Strinić, L. Prodan, V. Tsurkan, I. Kézsmárki and J. Deisenhofer. *Magnetic and vibronic terahertz excitations in Zn-doped $Fe_2Mo_3O_8$.* Phys. Rev. B **102**, 174407 (2020)

[58] V. Tsurkan. *Private communication* (2019)

[59] S. Reschke, A. A. Tsirlin, N. Khan, L. Prodan, V. Tsurkan, I. Kézsmárki and J. Deisenhofer. *Structure, phonons, and orbital degrees of freedom in $Fe_2Mo_3O_8$.* Phys. Rev. B **102**, 094307 (2020)

[60] T. N. Stanislavchuk, G. L. Pascut, A. P. Litvinchuk, Z. Liu, S. Choi, M. J. Gutmann, B. Gao, K. Haule, V. Kiryukhin, S.-W. Cheong and A. A. Sirenko. *Spectroscopic and first principle DFT+eDMFT study of complex structural, electronic, and vibrational properties of $M_2Mo_3O_8$ (M=Fe, Mn) polar magnets.* Phys. Rev. B **102**, 115139 (2020)

[61] Y. Tokura, S. Seki and N. Nagaosa. *Multiferroics of spin origin.* Rep. Prog. Phys. **77**, 076501 (2014)

[62] Y. Li, G. Gao and K. Yao. *Dzyaloshinskii-Moriya interaction of polar magnet $Fe_2Mo_3O_8$ and its multiferroicity.* EPL (Europhysics Letters) **118**, 37001 (2017)

[63] T. Kurumaji, Y. Takahashi, J. Fujioka, R. Masuda, H. Shishikura, S. Ishiwata and Y. Tokura. *Optical magnetoelectric resonance in a polar magnet $(Fe,Zn)_2Mo_3O_8$ with axion-type coupling* . Phys. Rev. Lett. **119**, 077206 (2017)

[64] T. Kurumaji, Y. Takahashi, J. Fujioka, R. Masuda, H. Shishikura, S. Ishiwata and Y. Tokura. *Electromagnon resonance in a collinear spin state of the polar antiferromagnet $Fe_2Mo_3O_8$.* Phys. Rev. B **95**, 020405(R) (2017)

[65] H. Barz. *New ferromagnetic molybdenum spinels.* Mat. Res. Bull. **8**, 983 (1973)

[66] H. Ben Yaich, J. C. Jegaden, M. Potel, M. Sergent, A. K. Rastogi and R. Tournier. *Nouveaux chalcogénures et chalcohalogénures à clusters tétraédriques Nb_4 ou Ta_4.* J. Less Common Met. **102**, 9 (1984)

[67] D. Johrendt. *Crystal and electronic structure of the tetrahedral V_4 cluster compounds GeV_4Q_8 (Q = S, Se).* Z. anorg. Allg. Chem. **624**, 952 (1998)

[68] R. Pocha, D. Johrendt and R. Pöttgen. *Electronic and structural instabilities in GaV_4S_8 and $GaMo_4S_8$.* Chem. Mater. **12**, 2882 (2000)

[69] I. Kézsmárki, S. Bordács, P. Milde, E. Neuber, L. M. Eng, J. S. White, H. M. Rønnow, C. D. Dewhurst, M. Mochizuki, K. Yanai, H. Nakamura, D. Ehlers, V. Tsurkan and A. Loidl. *Néel-type skyrmion lattice with confined orientation in the polar magnetic semiconductor GaV_4S_8.* Nat. Mater. **14**, 1116 (2015)

[70] Á. Butykai, S. Bordács, I. Kézsmárki, V. Tsurkan, A. Loidl, J. Döring, E. Neuber, P. Milde, S. C. Kehr and L. M. Eng. *Characteristics of ferroelectric-ferroelastic domains in Néel-type skyrmion host GaV_4S_8.* Sci. Rep. **7**, 44663 (2017)

[71] J. M. Vandenberg and D. Brasen. *Structural behavior of the ferromagnetic spinels $Al_xMo_2S_4$ and $Ga_xMo_2S_4$ containing tetrahedral clusters of molybdenum atoms.* J. Solid State Chem. **14**, 203 (1975)

[72] D. Bichler and D. Johrendt. *Interplay of magnetism and bonding in $GaV_{4-x}Cr_xSe_8$.* Chem. Mater. **23**, 3014 (2011)

[73] S. Harris. *Structure, bonding and electron counts in cubane-type clusters having M_4S_4, $M_2M'_2S_4$ and MM'_3S_4 cores.* Polyhedron **8**, 2843 (1989)

[74] R. Pocha, D. Johrendt, B. Ni and M. M. Abd-Elmeguid. *Crystal structures, electronic properties, and pressure-induced superconductivity of the tetrahedral cluster compounds $GaNb_4S_8$, $GaNb_4Se_8$, and $GaTa_4Se_8$.* J. Am. Chem. Soc. **127**, 8732 (2005)

[75] H. Müller, W. Kockelmann and D. Johrendt. *The magnetic structure and electronic ground states of Mott insulators GeV_4S_8 and GaV_4S_8.* Chem. Mater. **18**, 2174 (2006)

[76] Y. Fujima, N. Abe, Y. Tokunaga and T. Arima. *Thermodynamically stable skyrmion lattice at low temperatures in a bulk crystal of lacunar spinel GaV_4Se_8.* Phys. Rev. B **95**, 180410(R) (2017)

[77] D. Bichler. *Magnetismus und strukturelle Phasenumwandlungen von Verbindungen mit tetraedrischen Metallclustern.* Ph.D. thesis, Ludwig-Maximilians-Universität München (2010)

[78] S. Jakob, H. Müller, D. Johrendt, S. Altmannshofer, W. Scherer, S. Rayaprol and R. Pöttgen. *Structural and magnetic transitions in the Mott insulator $GaNb_4S_8$.* J. Mat. Chem. **17**, 3833 (2007)

[79] S. Jakob. *Strukturen, Magnetismus und Phasenumwandlungen der Mott-Isolatoren $Ga(M_{4-x}M'_x)Q_8$ und $(M_{4-x}M'_x)Q_4I_4$ (M, M' = Mo, Nb, Ta; Q = S, Se; x = 0 – 4).* Ph.D. thesis, Ludwig-Maximilians-Universität München (2007)

[80] H. Ishikawa, T. Yajima, A. Matsuo, Y. Ihara and K. Kindo. *Nonmagnetic ground states and a possible quadrupolar phase in 4d and 5d lacunar spinel selenides GaM_4Se_8 (M = Nb, Ta).* Phys. Rev. Lett. **124**, 227202 (2020)

[81] K. Geirhos. *Private communication* (2020)

[82] M. François, W. Lengauer, K. Yvon, H. Ben Yaich-Aerrache, P. Gougeon, M. Potel and M. Sergent. *Structural phase transition in $GaMo_4S_8$ by X-ray powder diffraction.* Z. Kristallogr. **196**, 111 (1991)

[83] M. François, O. V. Alexandrov, K. Yvon, H. Ben Yaich-Aerrache, P. Gougeon, M. Potel and M. Sergent. *Structural phase transition in $GaMo_4Se_8$ and $AlMo_4S_8$ by X-ray powder diffraction.* Z. Kristallogr. **200**, 47 (1992)

[84] D. Bichler, V. Zinth, D. Johrendt, O. Heyer, M. K. Forthaus, T. Lorenz and M. M. Abd-Elmeguid. *Structural and magnetic phase transitions of the V_4-cluster compound GeV_4S_8.* Phys. Rev. B **77**, 212102 (2008)

[85] K. Singh, C. Simon, E. Cannuccia, M.-B. Lepetit, B. Corraze, E. Janod and L. Cario. *Orbital-ordering-driven multiferroicity and magnetoelectric coupling in GeV_4S_8.* Phys. Rev. Lett. **113**, 137602 (2014)

[86] Z. Wang, E. Ruff, M. Schmidt, V. Tsurkan, I. Kézsmárki, P. Lunkenheimer and A. Loidl. *Polar dynamics at the Jahn-Teller transition in ferroelectric GaV_4S_8.* Phys. Rev. Lett. **115**, 207601 (2015)

[87] E. Ruff, A. Butykai, K. Geirhos, S. Widmann, V. Tsurkan, E. Stefanet, I. Kézsmárki, A. Loidl and P. Lunkenheimer. *Polar and magnetic order in* GaV_4Se_8. Phys. Rev. B **96**, 165119 (2017)

[88] K. Geirhos, S. Krohns, H. Nakamura, T. Waki, Y. Tabata, I. Kézsmárki and P. Lunkenheimer. *Orbital-order driven ferroelectricity and dipolar relaxation dynamics in multiferroic* $GaMo_4S_8$. Phys. Rev. B **98**, 224306 (2018)

[89] E. Cannuccia, V. Ta Phuoc, B. Brière, L. Cario, E. Janod, B. Corraze and M. B. Lepetit. *Combined first-principles calculations and experimental study of the phonon modes in the multiferroic compound* GeV_4S_8. J. Phys. Chem. C **121**, 3522 (2017)

[90] Y. Tabata, Y. Kajinami, T. Waki, I. Watanabe and H. Nakamura. *μSR study on the spin singlet state in the $S = 1/2$ cluster magnet* $GaNb_4S_8$. J. Phys.: Conf. Ser. **225**, 012055 (2010)

[91] T. Waki, Y. Kajinami, Y. Tabata, H. Nakamura, M. Yoshida, M. Takigawa and I. Watanabe. *Spin-singlet state formation in the cluster Mott insulator* $GaNb_4S_8$ *studied by μSR and NMR spectroscopy.* Phys. Rev. B **81**, 020401(R) (2010)

[92] S. Kawamoto, T. Higo, T. Tomita, S. Suzuki, Z. M. Tian, K. Mochitzuki, A. Matsuo, K. Kindo and S. Nakatsuji. *Frustrated magnetism in a Mott insulator based on a transition metal chalcogenide.* J. Phys.: Conf. Ser. **683**, 012025 (2016)

[93] S. Bordács, A. Butykai, B. G. Szigeti, J. S. White, R. Cubitt, A. O. Leonov, S. Widmann, D. Ehlers, H.-A. Krug von Nidda, V. Tsurkan, A. Loidl and I. Kézsmárki. *Equilibrium skyrmion lattice ground state in a polar easy-plane magnet.* Sci. Rep. **7**, 7584 (2017)

[94] Á. Butykai and D. Szaller and L. F. Kiss and L. Balogh and M. Garst and L. DeBeer-Schmitt and T. Waki and Y. Tabata and H. Nakamura and I. Kézsmárki and S. Bordács. *Squeezing magnetic modulations by enhanced spin-orbit coupling of 4d electrons in the polar semiconductor* $GaMo_4S_8$. arXiv:1910.11523v1 (2019)

[95] B. Gross, S. Philipp, K. Geirhos, A. Mehlin, S. Bordács, V. Tsurkan, A. Leonov, I. Kézsmárki and M. Poggio. *Stability of Néel-type skyrmion lattice against oblique magnetic fields in* GaV_4S_8 *and* GaV_4Se_8. Phys. Rev. B **102**, 104407 (2020)

[96] K. Geirhos, B. Gross, B. G. Szigeti, A. Mehlin, S. Philipp, J. S. White, R. Cubitt, S. Widmann, S. Ghara, P. Lunkenheimer, V. Tsurkan, E. Neuber,

D. Ivaneyko, P. Milde, L. M. Eng, A. O. Leonov, S. Bordács, M. Poggio and I. Kézsmárki. *Macroscopic manifestation of domain-wall magnetism and magnetoelectric effect in a Néel-type skyrmion host.* npj Quantum Mater. **5**, 44 (2020)

[97] S. Widmann, E. Ruff, A. Günther, H.-A. Krug von Nidda, P. Lunkenheimer, V. Tsurkan, S. Bordács, I. Kézsmárki and A. Loidl. *On the multiferroic skyrmion-host* GaV_4S_8. Philos. Mag. **97**, 3428 (2017)

[98] S. Widmann, A. Günther, E. Ruff, V. Tsurkan, H.-A. Krug von Nidda, P. Lunkenheimer and A. Loidl. *Structural, magnetic, electric, dielectric, and thermodynamic properties of multiferroic* GeV_4S_8. Phys. Rev. B **94**, 214421 (2016)

[99] A. K. Rastogi, A. Berton, J. Chaussy, R. Tournier, M. P. R. Chevrel and M. Sergent. *Itinerant electron magnetism in the* Mo_4 *tetrahedral cluster compounds* $GaMo_4S_8$, $GaMo_4Se_8$, *and* $GaMo_4Se_4Te_4$. J. Low Temp. Phys. **52**, 539 (1983)

[100] H. Ben Yaich, J. Jegaden, M. Potel, C. Chevrel, M. Sergent, A. Berton, J. Chaussy, A. K. Rastogi and R. Tournier. *Nouveaux chalcogenures mixtes* $GaMo_4(XX')_8$ *(X = S, Se, Te) à clusters tetraedriques* Mo_4. J. Solid State Chem. **51**, 212 (1984)

[101] R. Ikeno, H. Nakamura and T. Kohara. *Cluster-spin dynamics in a* $GaMo_4S_8$*-type compound:* ^{27}Al *nuclear magnetic resonance study of* $AlMo_4S_8$. J. Phys.: Condens. Matter **19**, 046206 (2007)

[102] A. K. Rastogi and E. P. Wohlfarth. *Magnetic field-induced transitions in the* Mo_4 *cluster compounds* $GaMo_4S_8$ *and* $GaMo_4Se_8$ *showing heavy fermion behaviour.* Phys. stat. sol. (b) **142**, 569 (1987)

[103] M. M. Abd-Elmeguid, B. Ni, D. I. Khomskii, R. Pocha, D. Johrendt, X. Wang and K. Syassen. *Transition from Mott insulator to superconductor in* $GaNb_4Se_8$ *and* $GaTa_4Se_8$ *under high pressure.* Phys. Rev. Lett. **93**, 126403 (2004)

[104] M. J. Park, G. Sim, M. Y. Jeong, A. Mishra, M. J. Han and S. Lee. *Pressure-induced topological superconductivity in the spin-orbit Mott insulator* $GaTa_4Se_8$. npj Quantum Mater. **5**, 41 (2020)

[105] V. Ta Phuoc, C. Vaju, B. Corraze, R. Sopracase, A. Perucchi, C. Marini, P. Postorino, M. Chligui, S. Lupi, E. Janod and L. Cario. *Optical conductivity measurements of* $GaTa_4Se_8$ *under high pressure: Evidence of a bandwidth-controlled insulator-to-metal Mott transition.* Phys. Rev. Lett. **110**, 037401 (2013)

[106] A. Camjayi, C. Acha, R. Weht, M. G. Rodríguez, B. Corraze, E. Janod, L. Cario and M. J. Rozenberg. *First-order insulator-to-metal Mott transition in the paramagnetic 3D system $GaTa_4Se_8$.* Phys. Rev. Lett. **113**, 086404 (2014)

[107] L. Cario, C.Vaju, B. Corraze, V. Guiot and E. Janod. *Electric-field-induced resistive switching in a family of mott insulators: Towards a new class of RRAM memories.* Adv. Mater. **22**, 5193 (2010)

[108] V. Dubost, T. Cren, C. Vaju, L. Cario, B. Corraze, E. Janod, F. Debontridder and D. Roditchev. *Resistive switching at the nanoscale in the Mott insulator compound $GaTa_4Se_8$.* Nano Lett. **13**, 3648 (2013)

[109] P. Stoliar, L. Cario, E. Janod, B. Corraze, C. Guillot-Deudon, S. Salmon-Bourmand, V. Guiot, J. Tranchant and M. Rozenberg. *Universal electric-field-driven resistive transition in narrow-gap Mott insulators.* Adv. Mater. **25**, 3222 (2013)

[110] E. Dorolti, L. Cario, B. Corraze, E. Janod, C. Vaju, H.-J. Koo, E. Kan and M.-H. Whangbo. *Halfmetallic ferromagnetism and large negative magnetoresistance in the new lacunar spinel $GaTi_3VS_8$.* J. Am. Chem. Soc. **132**, 5704 (2010)

[111] H.-S. Kim, J. Im, M. J. Han and H. Jin. *Spin-orbital entangled molecular j_{eff} states in lacunar spinel compounds.* Nat. Commun. **5**, 3988 (2014)

[112] E. Ruff, S. Widmann, P. Lunkenheimer, V. Tsurkan, S. Bordács, I. Kézsmárki and A. Loidl. *Multiferroicity and skyrmions carrying electric polarization in GaV_4S_8.* Sci. Adv. 1:e1500916 (2015)

[113] N. Shanthi and D. D. Sarma. *Electronic structure of vacancy ordered spinels, $GaMo_4S_8$ and GaV_4S_8, from ab initio calculations.* J. Sol. State Chem. **148**, 143 (1999)

[114] H.-S. Kim, K. Haule and D. Vanderbilt. *Molecular Mott state in the deficient spinel GaV_4S_8.* Phys. Rev. B **102**, 081105(R) (2020)

[115] N. F. Mott. *Conduction in non-crystalline materials. III. Localized states in a pseudogap and near extremities of conduction and valence bands.* Phil. Mag. **19**, 835 (1969)

[116] A. Camjayi, R. Weht and M. J. Rozenberg. *Localised Wannier orbital basis for the Mott insulators GaV_4S_8 and $GaTa_4Se_8$.* EPL **100**, 57004 (2012)

[117] Y. Wang, D. Puggioni and J. M. Rondinelli. *Assessing exchange-correlation functional performance in the chalcogenide lacunar spinels GaM_4Q_8 (M = Mo, V, Nb, Ta; Q = S, Se).* Phys. Rev. B **100**, 115149 (2019)

[118] S. Zhang, T. Zhang, H. Deng, Y. Ding, Y. Chen and H. Weng. *Crystal and electronic structure of $GaTa_4Se_8$ from first-principle calculations.* arXiv:2007.12435v1 (2020)

[119] M. Sieberer, S. Turnovszky, J. Redinger and P. Mohn. *Importance of cluster distortions in the tetrahedral cluster compounds GaM_4X_8 (M = Mo, V, Nb, Ta; X = S, Se): Ab initio investigations.* Phys. Rev. B **76**, 214106 (2007)

[120] A. O. Leonov and I. Kézsmárki. *Asymmetric isolated skyrmions in polar magnets with easy-plane anisotropy.* Phys. Rev. B **96**, 014423 (2017)

[121] A. O. Leonov and I. Kézsmárki. *Skyrmion robustness in noncentrosymmetric magnets with axial symmetry: The role of anisotropy and tilted magnetic fields.* Phys. Rev. B **96**, 214413 (2017)

[122] W. Withayachumnankul, B. Ferguson, T. Rainsford, S. P. Mickan and D. Abbot. *Simple material parameter estimation via terahertz time-domain spectroscopy.* Electron. Lett. **41**, 800 (2005)

[123] W. Withayachumnankul and M. Naftaly. *Fundamentals of measurement in terahertz time-domain spectroscopy.* J. Infrared Millim. Terahertz Waves **35**, 610 (2014)

[124] J.-H. Son. *Terahertz electromagnetic interactions with biological matter and their applications.* J. Appl. Phys. **105**, 102033 (2009)

[125] B. Gorshunov, A. Volkov, I. Spektor, A. Prokhorov, A. Mukhin, M. Dressel, S. Uchida and A. Loidl. *Terahertz BWO-spectroscopy.* Int. J. Infrared Millimeter Waves **26**, 1217 (2005)

[126] A. A. Volkov, Y. Goncharov, G. V. Kozlov, S. P. Lebedev and A. M. Prokhorov. *Dielectric measurements in the submillimeter wavelength region.* Infrared Phys. **25**, 369 (1985)

[127] A. A. Volkov, G. V. Kozlov and A. M. Prokhorov. *Progress in submillimeter spectroscopy of solid state.* Infrared Phys. **29**, 747 (1989)

[128] K. Sakai and M. Tani. *Introduction to terahertz pulses.* In K. Sakai, editor, *Terahertz Optoelectronics,* Topics Appl. Phys. **97**, 1 – 31. Springer-Verlag Berlin Heidelberg (1990)

[129] D. H. Auston. *Picosecond optoelectronic switching and gating in silicon.* Appl. Phys. Lett. **26**, 101 (1975)

[130] C. H. Lee. *Picosecond optoelectronic switching in GaAs.* Appl. Phys. Lett. **30**, 84 (1977)

[131] D. H. Auston, K. P. Cheung and P. R. Smith. *Picosecond photoconducting hertzian dipoles.* Appl. Phys. Lett. **45**, 284 (1984)

[132] P. R. Smith, D. H. Auston and M. C. Nuss. *Subpicosecond photoconducting dipole antennas.* IEEE J. Quantum Electron. **24**, 255 (1988)

[133] W. Withayachumnankul, G. M. Png, X. Yin, S. Atakaramians, I. Jones, H. Lin, B. S. Y. Ung, J. Balakrishnan, B. W.-H. Ng, B. Ferguson, S. P. Mickan, B. M. Fischer and D. Abbot. *T-ray sensing and imaging.* Proc. IEEE **95**, 1528 (2007)

[134] M. Tonouchi. *Cutting-edge terahertz technology.* Nat. Photonics **1**, 97 (2007)

[135] M. Hangyo, M. Tani and T. Nagashima. *Terahertz time-domain spectroscopy of solids: A review.* Int. J. Infrared Millimeter Waves **26**, 1661 (2005)

[136] L. Duvillaret, F. Garet, J.-F. Roux and J.-L. Coutaz. *Analytical modelling and optimization of terahertz time-domain spectroscopy experiments using photoswitches as antennas.* IEEE J. Sel. Topics Quantum Electron. **7**, 615 (2001)

[137] J. Neu and C. A. Schmuttenmaer. *Tutorial: An introduction to terahertz time domain spectroscopy (THz-TDS).* J. Appl. Phys. **124**, 231101 (2018)

[138] C. A. Schmuttenmaer. *Exploring dynamics in the far-infrared with terahertz spectroscopy.* Chem. Rev. **104**, 1759 (2004)

[139] L. Duvillaret, F. Garet and J.-L. Coutaz. *A reliable method for extraction of material parameters in terahertz time-domain spectroscopy.* IEEE J. Sel. Topics Quantum Electron. **2**, 739 (1996)

[140] M. Hangyo, T. Nagashima and S. Nashima. *Spectroscopy by pulsed terahertz radiation.* Meas. Sci. Technol. **13**, 1727 (2002)

[141] S. Nishizawa, K. Sakai, M. Hangyo, T. Nagashima, M. W. Takeda, K. Tominaga, A. Oka, K. Tanaka and O. Morikawa. *Terahertz time-domain spectroscopy.* In K. Sakai, editor, *Terahertz Optoelectronics,* Topics Appl. Phys. **97**, 203 – 271. Springer-Verlag Berlin Heidelberg (1990)

[142] T. Fließbach. *Elektrodynamik.* Springer-Verlag Berlin Heidelberg, 6. edition (2012)

[143] S. Hunklinger. *Festkörperphysik.* De Gruyter, 4. edition (2014)

[144] M. Dressel and G. Grüner. *Electrodynamics of solids. Optical properties of electrons in matter.* Cambridge (2002)

[145] A. A. Michelson. *On the application of interference-methods to spectroscopic measurements.-I.* Phil. Mag. **31**, 338 (1891)

[146] A. A. Michelson. *On the application of interference methods to spectroscopic measurements.-II.* Phil. Mag. **34**, 280 (1892)

[147] J. B. Bates. *Fourier transform spectroscopy.* Comput. Math. with Appl. **4**, 73 (1978)

[148] H. Günzler and H.-U. Gremlich. *IR-Spektroskopie.* Wiley-VCH Verlag, Weinheim, 4. edition (2003)

[149] P. R. Griffiths and J. A. de Haseth. *Fourier transform infrared spectrometry.* Wiley, 2. edition (2007)

[150] F. Mayr. *Breitbandige optische Spektroskopie an Manganaten mit Perowskit-Struktur.* Ph.D. thesis, Universität Augsburg (2002)

[151] J. B. Bates. *Fourier transform infrared spectroscopy.* Science **191**, 31 (1976)

[152] J. S. Toll. *Causality and the dispersion relation: Logical foundations.* Phys. Rev. **104**, 1760 (1956)

[153] R. de L. Kronig. *On the theory of dispersion of X-rays.* J. Opt. Soc. Am. **12**, 547 (1926)

[154] H. A. Kramers. *La diffusion de la lumière par les atomes.* Atti Cong. Intern. Fisici Como **2**, 545 – 557 (1927)

[155] F. Wooten. *Optical properties of solids.* Academic Press, New York and London (1972)

[156] B. Velický. *Dispersion relation for complex reflectivity.* Czech. J. Phys. B **11**, 541 (1961)

[157] A. S. Barker jr. and M. Tinkham. *Far-infrared ferroelectric vibration mode in $SrTiO_3$.* Phys. Rev. **125**, 1527 (1962)

[158] F. W. King. *Dispersion relations and sum rules for the normal reflectance of conductors and insulators.* J. Chem. Phys. **71**, 4726 (1979)

[159] P. O. Nilsson and L. Munkby. *Investigation of errors in the Kramers-Kronig analysis of reflectance data.* Phys. kondens. Materie **10**, 290 (1969)

[160] G. Leveque. *Reflectivity extrapolations in Kramers-Kronig analysis.* J. Phys. C: Solid State Phys. **10**, 4877 (1977)

[161] A. G. Gurevich and G. A. Melkov. *Magnetization oscillations and waves.* CRC Press (1996)

[162] K. Penc, J. Romhányi, T. Rõõm, U. Nagel, Á. Antal, T. Fehér, A. Jánossy, H. Engelkamp, H. Murakawa, Y. Tokura, D. Szaller, S. Bordács and I. Kézsmárki. *Spin-stretching modes in anisotropic magnets: Spin-wave excitations in the multiferroic $Ba_2CoGe_2O_7$.* Phys. Rev. Lett. **108**, 257203 (2012)

[163] A. Zheludev, T. Sato, T. Masuda, K. Uchinokura, G. Shirane and B. Roessli. *Spin waves and the origin of commensurate magnetism in $Ba_2CoGe_2O_7$.* Phys. Rev. B **68**, 024428 (2018)

[164] H. Murakawa, Y. Onose, S. Miyahara, N. Furukawa and Y. Tokura. *Ferroelectricity induced by spin-dependent metal-ligand hybridization in $Ba_2CoGe_2O_7$.* Phys. Rev. Lett. **105**, 137202 (2010)

[165] V. Hutanu, A. Sazonov, M. Meven, H. Murakawa, Y. Tokura, S. Bordács, I. Kézsmárki and B. Náfrádi. *Determination of the magnetic order and the crystal symmetry in the multiferroicground state of $Ba_2CoGe_2O_7$.* Phys. Rev. B **86**, 104401 (2012)

[166] M. Eremin. *Private communication* (2020)

[167] D. Szaller. *High-field measurements on $Fe_2Mo_3O_8$.* Unpublished (2014)

[168] W. Low and M. Weger. *Paramagnetic resonance and optical spectra of divalent iron in cubic fields. I. Theory.* Phys. Rev. **118**, 1119 (1960)

[169] S. Reschke, F. Meggle, F. Mayr, V. Tsurkan, L. Prodan, H. Nakamura, J. Deisenhofer, C. A. Kuntscher and I. Kézsmárki. *Lattice dynamics and electronic excitations in a large family of lacunar spinels with a breathing pyrochlore lattice structure.* Phys. Rev. B **101**, 075118 (2020)

[170] T. Chatterji and T. C. Hansen. *Magnetoelastic effects in Jahn-Teller distorted CrF_2 and CuF_2 studied by neutron powder diffraction.* J. Phys.: Condens. Matter **23**, 276007 (2011)

[171] W. Low and M. Weger. *Paramagnetic resonance and optical spectra of divalent iron in cubic fields. II. Experimental results.* Phys. Rev. **118**, 1130 (1960)

[172] L. F. Feiner. *Unified description of the cooperative Jahn-Teller effect in $FeCr_2S_4$, and the impurity Jahn-Teller effect in $CoCr_2S_4$:Fe^{2+}.* J. Phys. C: Solid State Phys. **15**, 1515 (1982)

[173] O. Mualin, E. E. Vogel, M. A. de Orúe, L. Martinelli, G. Bevilacqua and H.-J. Schulz. *Two-mode Jahn-Teller effect in the absorption spectra of Fe^{2+} in II-VI and III-V semiconductors.* Phys. Rev. B **65**, 035211 (2001)

[174] K. Ohgushi, T. Ogasawara, Y. Okimoto, S. Miyasaka and Y. Tokura. *Gigantic Kerr rotation induced by a d-d transition resonance in MCr_2S_4 (M = Mn,Fe).* Phys. Rev. B **72**, 155114 (2005)

[175] V. V. Fedorov, S. B. Mirov, A. Gallian, D. V. Badikov, M. P. Frolov, Y. V. Korostelin, V. I. Kozlovsky, A. I. Landman, Y. P. Podmar'kov, V. A. Akimov and A. A. Voronov. *$3.77 - 5.05$-μm tunable solid-state lasers based on Fe^{2+}-doped ZnSe crystals operating at low and room temperatures.* IEEE J. Quantum Electron. **42**, 907 (2006)

[176] N. J. Laurita, J. Deisenhofer, L. D. Pan, C. M. Morris, M. Schmidt, M. Johnsson, V. Tsurkan, A. Loidl and N. P. Armitage. *Singlet-Triplet excitations and long-range entanglement in the spin-orbital liquid candidate $FeSc_2S_4$.* Phys. Rev. Lett. **114**, 207201 (2015)

[177] J. W. Evans, T. R. Harris, B. R. Reddy, K. L. Schepler and P. A. Berry. *Optical spectroscopy and modeling of Fe^{2+} ions in zinc selenide.* J. Lumin **188**, 541 (2017)

[178] J. Stöhr and H. C. Siegmann. *Magnetism.* Springer, Berlin, 1 edition (2006)

[179] E. Riedel and C. Janiak. *Anorganische Chemie.* De Gruyter, Berlin, 7 edition (2007)

[180] A. B. Kuzmenko. *Kramers–Kronig constrained variational analysis of optical spectra.* Rev. Sci. Instr. **76**, 083108 (2005)

[181] A. B. Kuzmenko. *RefFIT v. 1.3.05* (2018). https://reffit.ch/

[182] R. A. Cowley. *The lattice dynamics of an anharmonic crystal.* Adv. Phys. **12**, 421 (1963)

[183] R. A. Cowley. *Raman scattering from crystals of the diamond structure.* J. Phys. **26**, 659 (1965)

[184] P. G. Klemens. *Anharmonic decay of optical phonons.* Phys. Rev. **148**, 845 (1966)

[185] J. Menéndez and M. Cardona. *Temperature dependence of the first-order Raman scattering by phonons in Si, Ge, and α-Sn: Anharmonic effects.* Phys. Rev. B **29**, 2051 (1984)

[186] G. A. Slack, F. S. Ham and R. M. Chrenko. *Optical absorption of tetrahedral Fe^{2+} ($3d^6$) in cubic ZnS, CdTe, and $MgAl_2O_4$.* Phys. Rev. **152**, 376 (1966)

[187] J. Hlinka, F. Borodavka, I. Rafalovskyi, Z. Docekalova, J. Pokorny, I. Gregora, V. Tsurkan, H. Nakamura, F. Mayr, C. A. Kuntscher, A. Loidl, S. Bordács, D. Szaller, H.-J. Lee, J. H. Lee and I. Kézsmárki. *Lattice modes and the Jahn-Teller ferroelectric transition of GaV_4S_8.* Phys. Rev. B **94**, 060104(R) (2016)

[188] C. Kant, J. Deisenhofer, T. Rudolf, F. Mayr, F. Schrettle, A. Loidl, V. Gnezdilov, D. Wulferding, P. Lemmens and V. Tsurkan. *Optical phonons, spin correlations, and spin-phonon coupling in the frustrated pyrochlore magnets $CdCr_2O_4$ and $ZnCr_2O_4$.* Phys. Rev. B **80**, 214417 (2009)

[189] K. Wakamura and T. Arai. *Effect of magnetic ordering on phonon parameters for infrared active modes in ferromagnetic spinel $CdCr_2S_4$.* J. Appl. Phys. **63**, 5824 (1988)

[190] M. Balkanski, R. F. Wallis and E. Haro. *Anharmonic effects in light scattering due to optical phonons in silicon.* Phys. Rev. B **28**, 1928 (1983)

[191] S. Reschke, F. Mayr, Z. Wang, P. Lunkenheimer, W. Li, D. Szaller, S. Bordács, I. Kézsmárki, V. Tsurkan and A. Loidl. *Optical conductivity in multiferroic GaV_4S_8 and GeV_4S_8: Phonons and electronic transitions.* Phys. Rev. B **96**, 144302 (2017)

[192] B. D. Viezbicke, S. Patel, B. E. Davis and D. P. Birnie III. *Evaluation of the Tauc method for optical absorption edge determination: ZnO Thin films as a model system.* Phys. Stat. Sol. B **252**, 1700 (2015)

[193] E. A. Davis and N. F. Mott. *Conduction in non-crystalline systems V. Conductivity, optical absorption and photoconductivity in amorphous semiconductors.* Philos. Mag. **22**, 903 (1970)

[194] K. P. O'Donnell and X. Chen. *Temperature dependence of semiconductor band gaps.* Appl. Phys. Lett. **58**, 2924 (1991)

[195] R. Pässler. *Semi-empirical descriptions of temperature dependences of band gaps in semiconductors.* Phys. Stat. Sol. B **236**, 710 (2003)

[196] V. Guiot, L. Cario, E. Janod, B. Corraze, V. Ta Phuoc, M. Rozenberg, P. Stoliar, T. Cren and D. Roditchev. *Avalanche breakdown in $GaTa_4Se_{8-x}Te_x$ narrow-gap Mott insulators.* Nat. Commun. **4**, 1722 (2013)

[197] V. Guiot, E. Janod, B. Corraze and L. Cario. *Control of the electronic properties and resistive switching in the new series of Mott insulators* $GaTa_4Se_{8-y}Te_y$*(*$0 \leq y \leq 6.5$*).* Chem. Mater. **23**, 2611 (2011)

[198] A. M. Stoneham. *Theory of defects in solids.* Oxford University Press (1975)

[199] Y. Toyozawa. *Optical processes in solids.* Cambridge University Press (2003)

[200] M. Rätsep, M. Pajusalu, J. M. Linnanto and A. Freiberg. *Subtle spectral effects accompanying the assembly of bacteriochlorophylls into cyclic light harvesting complexes revealed by high-resolution fluorescence spectroscopy.* J. Chem. Phys. **141**, 155102 (2014)

List of publications

Publications related to the thesis

- S. Reschke, A. A. Tsirlin, N. Khan, L. Prodan, V. Tsurkan, I. Kézsmárki and J. Deisenhofer. *Structure, phonons, and orbital degrees of freedom in* $Fe_2Mo_3O_8$. Phys. Rev. B, **102**, 094307 (2020)

- B. Csizi, S. Reschke, A. Strinić, L. Prodan, V. Tsurkan, I. Kézsmárki and J. Deisenhofer. *Magnetic and vibronic terahertz excitations in Zn-doped* $Fe_2Mo_3O_8$. Phys. Rev. B, **102**, 174407 (2020)

- S. Reschke, F. Meggle, F. Mayr, V. Tsurkan, L. Prodan, H. Nakamura, J. Deisenhofer, C. A. Kuntscher and I. Kézsmárki. *Lattice dynamics and electronic excitations in a large family of lacunar spinels with a breathing pyrochlore lattice structure.* Phys. Rev. B **101**, 075118 (2020)

- S. Reschke, F. Mayr, Z. Wang, P. Lunkenheimer, W. Li, D. Szaller, S. Bordács, I. Kézsmárki, V. Tsurkan and A. Loidl. *Optical conductivity in multiferroic* GaV_4S_8 *and* GeV_4S_8*: Phonons and electronic transitions.* Phys. Rev. B **96**, 144302 (2017)

Further publications

- A. Strinić, S. Reschke, K. V. Vasin, M. Schmidt, A. Loidl, V. Tsurkan, M. V. Eremin and J. Deisenhofer. *Magnetoelectric properties and low-energy excitations of multiferroic* $FeCr_2S_4$. Phys. Rev. B **102**, 134409 (2020)

- M. Majumder, M. Prinz-Zwick, S. Reschke, A. Zubtsovskii, T. Dey, F. Freund, N. Büttgen, A. Jesche, I. Kézsmárki, A. A. Tsirlin and P. Gegenwart. *Field evolution of low-energy excitations in the hyperhoneycomb magnet* β-Li_2IrO_3. Phys. Rev. B **101**, 214417 (2020)

- A. Sahasrabudhe, D. A. S. Kaib, S. Reschke, R. German, T. C. Koethe, J. Buhot, D. Kamenskyi, C. Hickey, P. Becker, V. Tsurkan, A. Loidl, S. H. Do, K. Y. Choi, M. Grüninger, S. M. Winter, Z. Wang, R. Valentí and P. H. M. van Loosdrecht. *High-field quantum disordered state in* α-$RuCl_3$*: Spin flips,*

bound states, and multiparticle continuum. Phys. Rev. B **101**, 140410(R) (2020)

- S. Reschke, V. Tsurkan, S.-H. Do, K.-Y. Choi, P. Lunkenheimer, Z. Wang and A. Loidl. *Terahertz excitations in α-$RuCl_3$: Majorana fermions and rigid-plane shear and compression modes.* Phys. Rev. B **100**, 100403(R) (2019)

- S. Reschke, F. Mayr, S. Widmann, H.-A. Krug von Nidda, V. Tsurkan, M. V. Eremin, S.-H. Do, K.-Y. Choi, Z. Wang and A. Loidl. *Sub-gap optical response in the Kitaev spin-liquid candidate α-$RuCl_3$.* J. Phys.: Condens. Matter **30**, 475604 (2018)

- J. Fritzsche, M. Grzywa, D. Denysenko, S. Reschke, K. Sugimoto, H.-A. Krug von Nidda, D. Schmidtner and D. Volkmer. *CFA-14 - a perfluorinated metal-organic framework with linear 1-D Co^{II}-chains showing temperature dependent spin-chain magnetic ordering.* Dalton Trans. **47**, 12750 (2018)

- Z. Wang, S. Reschke, D. Hüvonen, S.-H. Do, K.-Y. Choi, M. Gensch, U. Nagel, T. Rõõm and A. Loidl. *Magnetic excitations and continuum of a possibly field-induced quantum spin liquid in α-$RuCl_3$.* Phys. Rev. Lett. **119**, 227202 (2017)

- S. Reschke, F. Mayr, Z. Wang, S.-H. Do, K.-Y. Choi and A. Loidl. *Electronic and phonon excitations in α-$RuCl_3$.* Phys. Rev. B **96**, 165120 (2017)

- S. Reschke, Z. Wang, F. Mayr, E. Ruff, P. Lunkenheimer, V. Tsurkan and A. Loidl. *Excitations and relaxation dynamics in multiferroic GeV_4S_8 studied by terahertz and dielectric spectroscopy.* Phys. Rev. B **96**, 144418 (2017)

- S. Spirkl, M. Grzywa, S. Reschke, J. K. H. Fischer, P. Sippel, S. Demeshko, H.-A. Krug von Nidda and D. Volkmer. *Single-crystal to single-crystal transformation of a nonporous Fe(II) metal-organic framework into a porous metal-organic framework via a solid-state reaction.* Inorg. Chem. **56**, 12337 (2017)

- T. W. Werner, S. Reschke, H. Bunzen, H.-A. Krug von Nidda, J. Deisenhofer, A. Loidl and D. Volkmer. *[$Co_5Tp^*_4(Me_2bta)_6$]: A highly symmetrical pentanuclear Kuratowski complex featuring tris(pyrazolyl)borate and benzotriazolate ligands.* Inorg. Chem. **55**, 1053 (2016)

Acknowledgments

I would like to thank all persons who have contributed to the success of the present work:

- Prof. Dr. István Kézsmárki for the excellent supervision of this work, the interesting topic of optical spectroscopy on multiferroics and many scientific discussions.
- Prof. Dr. Christine Kuntscher for kindly reviewing this thesis and for the possibility to perform the mirco-IR measurements in her optical lab.
- Prof. Dr. Markus Grüninger for acting as an external reviewer for this thesis.
- Prof. Dr. Alois Loidl for the possibility to start my Ph.D. at EP V and for the supervision in the beginning of my doctoral studies.
- Dr. Joachim Deisenhofer for many scientific discussions, many useful pieces of advice and proofreading the thesis.
- Dr. Franz Mayr for sharing his lab experience and countless help with the spectrometers.
- Dr. Vladimir Tsurkan and Dr. Lilian Prodan for the growing of the high quality samples and the support with preparing them for the optical measurements.
- Dr. Alexander Tsirlin for performing the x-ray and neutron diffraction measurements on $Fe_2Mo_3O_8$, which motivated the IR study on this compound, and the DFT calculations.
- Prof. Dr. Mikhail Eremin for providing calculations of the crystal-field levels of $Fe_2Mo_3O_8$.
- Dr. Somnath Ghara for the good working atmosphere in our office and for performing the INS measurements on $Co_2Mo_3O_8$ in collaboration with Dr. Oksana Zaharko.
- Ana Strinić and Benjamin Csizi for their collaboration in the THz measurements on $Fe_2Mo_3O_8$ and $Fe_{1.86}Zn_{0.14}Mo_3O_8$ and the good atmosphere in the optics group.

- Fabian Meggle for the support with the micro-IR measurements.
- Daniel Farkas for the collaboration in optical measurements in Augsburg and Nijmegen.
- All members of EP V for the good working atmosphere.